Mississippi State University

Scholars Junction

5-5-2007

Multiscale Modeling of Hydrogen-Enhanced Void Nucleation

Mei Qiang Chandler

Follow this and additional works at: https://scholarsjunction.msstate.edu/td

MULTISCALE MODELING OF HYDROGEN- ENHANCED VOID NUCLEATION

By

Mei Qiang Chandler

A Dissertation
Submitted to the Faculty of
Mississippi State University
In Partial Fulfillment of the Requirements
for the Degree of Doctor of Philosophy
in Mechanical Engineering
in the Department of Mechanical Engineering
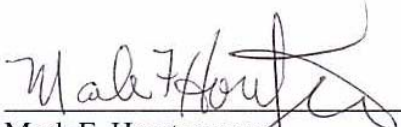
Mississippi State, Mississippi

March 2007

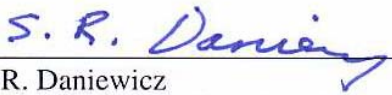Copyright by

Mei Qiang Chandler

2007

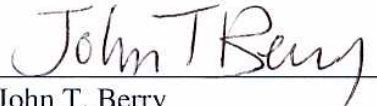MULTISCALE MODELING OF HYDROGEN- ENHANCED VOID NUCLEATION

By
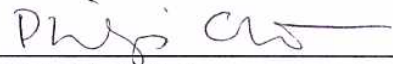
Mei Qiang Chandler
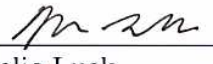
Approved:

Mark F. Horstemeyer
Chair Professor of Mechanical Engineering
(Director of Dissertation)
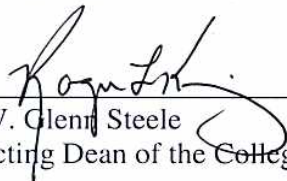
Steven R. Daniewicz
Professor of Mechanical engineering
(Graduate coordinator and Committee
 Member)

John T. Berry
E. P. Coleman Professor of Mechanical
Engineering
(Committee Member)

Philip M. Gullett
Assistant Professor of Civil Engineering
(Committee Member)

Rogelio Luck
Associate Professor of Mechanical
Engineering
(Committee Member)

Doug J. Bammann
Principal Member of Technical Staff of
Sandia National Laboratories
(Committee Member)

W. Glenn Steele
Acting Dean of the College of Engineering

Name: Mei Qiang Chandler

Date of Degree: May 4, 2007

Institution: Mississippi State University

Major Field: Mechanical Engineering

Major Professor: Mark Horstemeyer

Title of Study: MULTISCALE MODELING OF HYDROGEN-ENHANCED VOID NUCLEATION

Pages in Study: 142

Candidate for Degree of Doctor of Philosophy

Many experiments demonstrate that the effects of hydrogen solutes decrease macroscopic fracture stresses and strains in ductile materials. Hydrogen-related failures have occurred in nearly all industries involving hydrogen. The financial losses incurred from those failures reaches billions of dollars annually. With the ever-urgent needs for alternative energy sources such as hydrogen, safe storage and transportation of hydrogen increases the momentum for studying hydrogen-related failures, especially in ductile materials.

To quantify ductile material damage with the effects of hydrogen embrittlement, it is necessary to add hydrogen effects into the void nucleation, void growth, and void coalescence equations. In this research, hydrogen-enhanced void nucleation is our focus, with hydrogen-enhanced void growth and void coalescence to be studied in the future.

Molecular Dynamic (MD) and Monte Carlo (MC) simulations with Embedded Atom Method (EAM) potentials were performed to study how hydrogen affects

dislocation nucleation, dislocation structure formation and nanovoid nucleation at nickel grain boundaries. The results were inserted into the continuum void nucleation model by Horstemeyer and Gokhale, and the relationships between stress triaxiality-driven void nucleation, grain boundary hydrogen concentrations and local grain geometries were extracted.

MD and MC simulations with EAM potentials were also performed to study how hydrogen interstitials affect the dislocation nucleation, dislocation structure formation and subsequent nanovoid nucleation of single crystal nickel in different hydrogen-charging conditions. Evolutions of dislocation structures of nickel single crystal with different hydrogen concentrations were compared. The effects of nanovoid nucleation stress and strain at different hydrogen concentrations were quantified. The results were also inserted into the Horstemeyer and Gokhale model and the relationship between stress triaxiality-driven void nucleation and hydrogen concentration caused by stress gradient, which showed similar trends as the grain boundary studies.

From nanoscale studies and existing experimental observations, a continuum void nucleation model with hydrogen effects was proposed and used in a continuum damage model based upon Bammann and coworkers. The damage model was implemented into user material code in FEA code ABAQUS. Finite element analyses were performed and the results were compared to the experimental data by Kwon and Asaro.

DEDICATION

I would like to dedicate this research to my parents, Liu, Zhibiao and Qiang, Gongying,

my husband, Donnie Chandler, and my daughter, Sherlee Chandler.

ACKNOWLEDGEMENTS

I would like to take this opportunity to express my appreciation to a number of people who have helped and encouraged me during the work involved in this dissertation.

First, I would like to thank Dr. Mark Horstemeyer, my academic advisor and mentor, for his great effort in training me to think critically and independently, for working tirelessly on helping me to learn the art of communicating, both orally and verbally, in a professional and scientific manner, and for pushing me to manage my time and to reach milestones. His vast knowledge of multiscale modeling has been a great resource for me. His passion for science has been inspirational to me. He kindly helped me and my family during a time of need, which allowed me to be able to focus upon my research. He also helped me in finding my future job.

Second, I would like to express my deepest gratitude to Dr. Mike Baskes from Las Alamos National laboratory. He has spent a great amount of his precious time to improve my understanding of atomistic simulations and hydrogen embrittlement. He provided both Monte Carlo simulation codes and the Common Neighbor Analysis code, which I have used extensively in conducting this research. His many suggestions have been crucial for me to finish this research and write this dissertation.

Third, I would like to express my thanks to all of my graduate committee members for helping me and supporting my effort. Discussions with Dr. Douglas

TABLE OF CONTENTS

LIST OF TABLES

LIST OF FIGURES

xvi

LIST OF SYMBOLS, ABBREVIATIONS, AND SPECIAL NOMENCLATURE

Abbreviations

MD   Molecular Dynamics
MC   Monte Carlo
CNA   Common Neighbor Analysis
CDM   Continuum Damage Mechanics
EAM   Embedded Atom Method
CSL   Coincident Site occurrence Lattice
BCJ   Bammann-Chiesa-Johnson

Nomenclature

Molecular Dynamics

F_i^α	The force in ith direction acting on atom α
m^α	The mass of atom α
E	Total potential energy
x_i^α	The ith component of the atom's position
$f_{ij}^{\ k}$	The force vector between atoms i and j
$r_{ij}^{\ k}$	The position vector between atoms i and j
β_i^{km}	The stress tensor at atom i
σ^{km}	The continuum-like stress tensor
σ_m	The bulk mean stress
σ_{von}	von Mises stress
χ	Stress triaxality

Hydrogen/chemical potential

J	The molar flux of hydrogen atoms
H	Hydrogen concentration
D	The hydrogen diffusion coefficient
μ	Chemical potential
$\dfrac{\partial \mu}{\partial x}$	The gradient of chemical potential

Continuum damage model with hydrogen effects

ϕ	Damage
$\underline{L}$	The total velocity gradient
$\underline{L}^e$	Elastic velocity gradient
$\underline{L}^p$	Plastic velocity gradient
$\underline{L}^\Phi$	Damage-induced velocity gradient
$\underline{L}^H$	Hydrogen-induced velocity gradient
$\underline{\varepsilon}$	Total strain
$\underline{\varepsilon}^e$	Elastic strain
$\underline{\varepsilon}^p$	Plastic strain
$\underline{\varepsilon}^\Phi$	Damage-induced volumetric strain
$\underline{\varepsilon}^H$	Hydrogen-induced volumetric strain
$\overline{V}$	Hydrogen partial molar volume
Ω	The mean atomic volume of the host metal atom.
u	The internal energy per unit mass
ζ	The specific heat generation rate
$\underline{q}$	The heat flux vector
ρ	The density
T	Absolute temperature
μ_T	The specific entropy related to dissipation
ε^{ss}	The thermodynamic displacement caused by statistically-stored dislocations
κ	Isotropic hardening variable
Y	Thermodynamic force conjugated to damage
$\underline{C}$	Elastic moduli
H^κ	The isotropic hardening modulus
R^κ	The dynamic recovery constant
λ	Bulk modulus
μ^s	Shear modulus
ρ_{ss}	Dislocation density
$\overline{b}$	Burger's vector
c_1, c_2	Material constants
$V(T)$	Temperature dependence of the yield function
$Y(T)$	Temperature dependence of the yield function
$f(T)$	Temperature dependence of the yield function

Void growth

v	Void growth
C	Void coalescence
R_o	The initial average radius of the voids

xviii

ε_{eq} The equivalent plastic strain
n The strain hardening exponent

Void coalescence

C_{coal} Material constant
C_{CT} Temperature dependency on void coalescence

Void nucleation model/hydrogen effects

η Void nucleation
K_{IC} Fracture toughness
f The volume fraction of second phase particle
d Average diameter of second phase particles
I_1 The first stress invariant
J_2 The second invariant of deviatoric stress
J_3 The third invariant of deviatoric stress
a The void nucleation coefficient related to torsional loads
b The void nucleation coefficient related to compression and tension loads
c The void nucleation coefficient related to stress triaxiality
η_H Void nucleation with hydrogen effects
c_H The void nucleation coefficient related to stress triaxiality with hydrogen effects
m Material constant related to materials and local interfaces

Hydrogen concentration

H_L Bulk hydrogen concentration
H_B Hydrogen concentration at grain boundaries and interfaces
H_σ Local hydrogen concentration
P_{H_2} Hydrogen gas pressure (MPa)
R Gas constant
W_B Trap binding energy
N_α The number of sites per trap
N_T Trap site density per unit volume
θ_T The occupancy of the trapping sites

CHAPTER I

INTRODUCTION

1.1   Hydrogen Embrittlement and Mechanisms

Hydrogen embrittlement was first reported at least a century ago [1]. At first, the macro-aspect of hydrogen embrittlement was studied with a large number of metals. For most materials studied, the macroscopic aspect of hydrogen embrittlement has shown that solute hydrogen can reduce the ductility of the metals [2-7] and can change the fracture mode from void coalescence to transgranular cleavage or intergranular brittle fracture [8]. With the advent of the Scanning Electron Microscopy (SEM) and Transmission Electron Microscopy (TEM) technology, researchers were able to look into hydrogen embrittlement phenomena at the microscopic level. As a result, four main mechanisms have been proposed to explain the causes of hydrogen embrittlement: stress-induced hydride formation mechanism [9], Hydrogen-Enhanced Localized Plasticity (HELP) Mechanism [10-12], hydrogen-induced decohesion mechanism [13], and stacking fault mechanism [14-15].

Stress-induced hydride formation mechanism is based on the experimental observations that a number of metal-hydrogen systems can form stable hydrides at crack tips. Hydrides are brittle and have a low critical stress intensity factor. Cracks can grow through hydrides by cleavage [9]. Hydrogen-Enhanced Localized Plasticity mechanism is

1

based on the experiment observations that during plastic deformation, hydrogen atoms cause dislocation mobility to increase and cause strain localization. As a result, materials fail by enhanced localized plastic deformation [10-12, 16-17]. Hydrogen-induced decohesion mechanism is based on a theory that hydrogen atoms decrease the strength of atomic bonding at the tip of the crack and interfaces, and lower the energy to form a fracture surface [13, 18-20]. The stacking fault mechanism is based on experiments [14-15, 21-22] that show that hydrogen discourages cross slip and encourages planar slip, possibly by reducing the stacking fault energy of the system. Ferreira and coworkers' [22] experiments show that hydrogen did cause a reduction in the stacking fault energy of austenitic stainless steel.

1.2 Hydrogen Effects on Ductile Failures

In a monotonic loading condition, ductile materials fail by void nucleation, void growth, and void coalescences [23]. In a continuum sense, hydrogen effects on ductile failure mainly comprise two aspects. First is that hydrogen affects the plastic flow of the materials by either inducing softening or hardening on a material. Researchers suggest that hydrogen causes softening in high purity iron by increasing the mobility of screw dislocations and by interacting with dislocation pile-ups [24-25]. Oguri and Kimura [26] found that hydrogen causes either softening or hardening of iron depending upon the material purity, strain rate, and temperature. Lunarska and Flis [27] studied the effects of hydrogen on the stress-strain relationships for nickel and found that hydrogen caused softening possibly by stress relaxation at the specimen surface or by the generation of new dislocations. Abraham and Altstette [15] found that hydrogen can induce either

hardening or softening in an austenitic stainless steel. Second is that hydrogen affects the ductility of material, and causes the elongation to failure to decrease. Many experiments showed that hydrogen promoted void growth and void coalescence leading to the reduction of the elongation to failure. Garber and coworkers [28] found that hydrogen promotes void growth of spheroidized medium carbon steels. Cialone and Asaro [29] suggested that hydrogen not only promotes void initiation but also accelerates void growth and coalescence in spheroidized plain carbon steel. Park and Thompson [30] also investigated spheroidized AISI 1520 steel and found that hydrogen did not affect significantly the early stage of void growth; instead, it assisted the later stages of void growth and void coalescence. Park and Thompson [30] had previously suggested that internal pressure was responsible for the accelerated void growth. However, researchers [31-34] at a later time have suggested that hydrogen dilatation and strain localization caused by the HELP mechanism may be responsible for both accelerated void growth and void coalescence.

Several researchers suggested that hydrogen promotes higher rates of void nucleation based on experimental data for different materials. Louthan and coworkers [5] suggested that hydrogen promotes void nucleation after comparing the dimples on the fracture surfaces of hydrogen-charged specimens and those on an uncharged specimen of 304L stainless steel. Oriani and Josephic [34] also found that hydrogen enhanced the nucleation and early growth of microvoids in AISI 1045 steel. Thompson [35] examined the fracture surface of a single phase nickel alloy with a SEM under hydrogen-charged and uncharged conditions. Figure 1.1 shows that the void area density is nearly doubled

in hydrogen-charged condition versus a hydrogen-free condition [35]. For spheriodized carbon steels, experimental results [36-38] showed that hydrogen affects void growth more than void nucleation. However, for a 7075 aluminum alloy, Thompson and coworkers [39] found that the total number of voids nucleated in hydrogen-charged specimens was much larger than the number density shown in air-tested specimens.
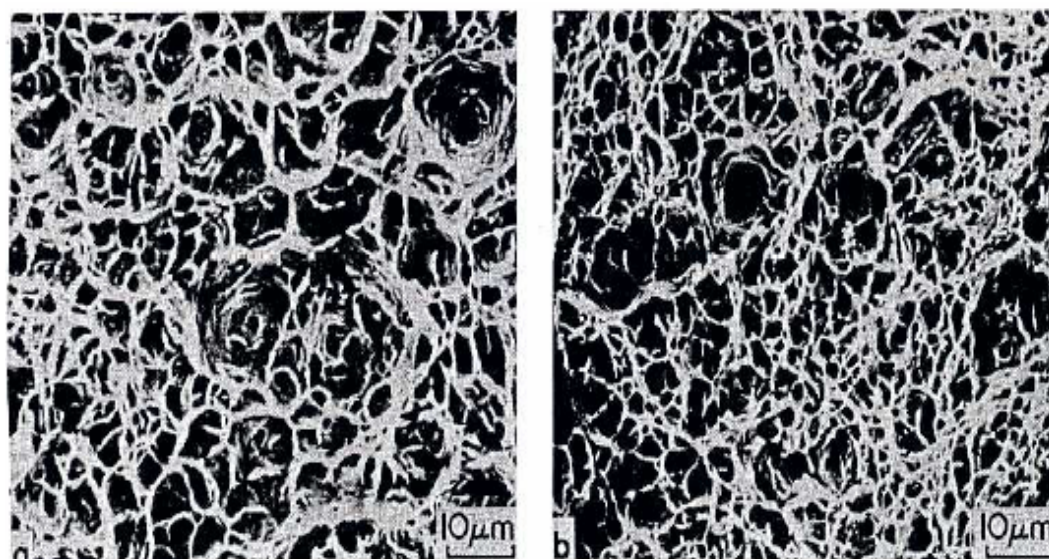
(a) Void area density $\approx 10^8/cm^2$
in a hydrogen-free
condition

(b) Void area density $\approx 2 \times 10^8/cm^2$
in a hydrogen-charged
condition

Figure 1.1.   The fracture surface of a single phase nickel alloy under Scanning Electron Microscopy (SEM) at hydrogen-charged (a) and uncharged conditions (b). The void area density in the hydrogen-charged condition is nearly twice of that in the hydrogen-free condition [35].

The void nucleation can be enhanced by different mechanisms. Kwon and Asaro [38] studied tensile specimens of spheroidized 1518 steel and found that hydrogen promotes void nucleation at average-sized carbide particles by reducing the critical interfacial strength. Jiang and coworkers [40] concluded that hydrogen promotes void

nucleation at either the intersection of active slip bands or at the dislocation cell walls by affecting local dislocation interactions in AISI 310 stainless steel. Clearly, all of these experimental studies indicate that hydrogen enhances the void/crack nucleation rate; the hydrogen-induced decohesion mechanism and the hydrogen-enhanced plasticity mechanism may both play a role in the nucleation process.

1.3 Research Objective

Many continuum void nucleation models [41-47] have been developed to predict ductile failures. Although those models have been used to solve many practical problems, hydrogen-enhanced void nucleation models are lacking for predicting material damage and failure with hydrogen effects. Liang and Sofronis [48] modeled the interfacial decohesion of an elastic inclusion in an elastic-plastic matrix coupled with hydrogen transport. Their work suggests that the strain for interfacial decohesion decreases with hydrogen. However, a continuum void nucleation equation that can be used with void growth and void coalescence to predict material damage and fracture was not formulated. Kwon and Asaro [38] proposed a continuum void nucleation rate model with hydrogen effects based only on interfacial stress reduction. Jiang and coworkers [40] proposed a model based on an assumption that hydrogen promotes microcrack nucleation by reducing the friction stress for operating the Frank-Read source and by forming dislocation pile-ups; as a result, decreasing the critical stress of microcrack nucleation. However, they did not propose a continuum void nucleation model with hydrogen effects.

A generally applicable void nucleation evolution equation should be a function of a length scale parameter, volume fraction of second phase materials, stress state, strain

rate and fracture toughness. Among many proposed void nucleation models, only the Horstemeyer-Gokale model includes all of the parameters mentioned above.

The objective of this work is to modify the Horstemeyer-Gokhale continuum void nucleation model [47] to account for hydrogen effects by employing a hierarchical multiscale modeling methodology. The mechanisms of hydrogen embrittlement demonstrate that the effects of hydrogen on material failures start from the nanoscale by interacting with defects [49-50] and by weakening atomic bonding [13, 18]. The multiscale modeling approach used is shown in Figure 1.2.
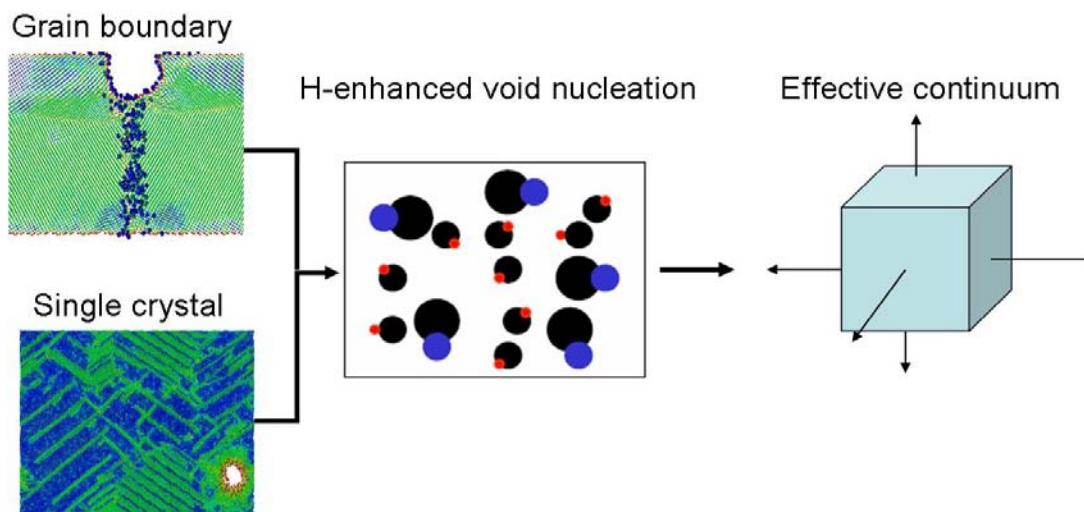
Figure 1.2. A schematic of multiscale modeling of void nucleation with hydrogen effects. At the nanoscale, hydrogen effects on plasticity and the subsequent nanovoid nucleation at grain boundaries and in a bulk single crystal are studied. At the microscale, a void nucleation model with hydrogen effects is developed based on the quantitative information from the nanoscale. At the macroscale, a continuum damage framework with hydrogen effects is developed and the new void nucleation model is implemented into the framework to predict damage and failure.

Molecular Dynamic simulations were performed to study the effects of hydrogen on nanovoid nucleation and interfacial debonding at different local grain structures. A low angle Σ257 (1610) [001] tilt grain boundary, a high angle Σ5 (310) [001] tilt grain boundary, and a single crystal, with the same specimen sizes, were studied (referring section *3.2.1* for information on Σ). MC simulations were used to introduce hydrogen atoms in the specimens. The bulk hydrogen concentration and the grain boundary hydrogen concentration at different applied chemical potentials were quantified. Hydrogen trapping at grain boundaries was discussed and the relationship between the grain boundary hydrogen concentration and the bulk hydrogen concentration was addressed. The dislocation nucleation and dislocation substructures formed at the grain boundary were compared for hydrogen-free and hydrogen–charged cases. The critical stresses and strains for void nucleation were quantified for different bulk and grain boundary hydrogen concentrations. The critical stresses and strains for nanovoid nucleation were inserted into the continuum Horstemeyer-Gokhale void nucleation model [47] to extract the quantitative relationships between void nucleation parameters, grain boundary hydrogen concentration and local grain structures.

Molecular Dynamic (MD) simulations [51] and Monte Carlo (MC) [52] simulations were also performed to study the effects of hydrogen interstitials on homogenous void nucleation of bulk single nickel crystals. In this study, the hydrogen transport by stress gradient and hydrogen trapping from plasticity-induced dislocations were addressed. The stress-strain response of the single crystals in hydrogen-free, hydrogen-precharged, and hydrogen dynamically-charged conditions, were addressed. In

each of these three conditions, the dislocation nucleation, dislocation substructures, and plasticity, were also studied. The critical stresses and strains for void nucleation for different hydrogen concentrations were quantified. The MD simulation results were also inserted into the Horstemeyer-Gokhale model [47] to associate the void nucleation and hydrogen concentration when hydrogen was absorbed into the specimen by stress gradient and was trapped by dislocations.

After quantifying the hydrogen effects at the nanoscale, the bulk effects of hydrogen on the kinematics, thermodynamics, and kinetics were derived in developing the constitutive equations and flow rules based on the Bammann-Chiesa-Johnson(BCJ) [53-54] continuum damage mechanics framework. Based on the nanoscale simulation results and existing experimental observations [55], the Horstemeyer-Gokhale void/crack nucleation rate [47] was modified to account for hydrogen effects. The continuum damage framework was implemented into the user material code and applied in the finite element calculations in ABAQUS 2006 [56]. The finite element results were compared to the experimental data of spheroidized 1518 steel [38].

1.4   Dissertation Structure

Chapter II presents overviews of several methods and concepts involved in the research. The basic concept of multiscale material modeling is discussed first. Then, a few basic concepts of the Molecular Dynamics (MD) simulation methods are reviewed, which include the equation of motion, integration method, periodic boundary conditions, constant pressure control, the Embedded Atom Method (EAM) potential and bulk quantities. A brief review of Continuum Damage Mechanics (CMD) is given.

Chapter III presents MD and MC simulation results of nickel grain boundaries. The hydrogen absorption and distribution, at different local grain structures, from MC simulation results, is presented first. The MC simulation results are used to associate grain boundary hydrogen concentrations with bulk hydrogen concentrations by introducing an effective trap binding energy into McLean's equation [57]. This relationship is used in the continuum model in Chapter V. The stress and strain responses and the dislocation evolution of different grain boundary structures are presented to address the effects of hydrogen on the plasticity. The critical stresses and strains at nanovoid nucleation are quantified at different bulk hydrogen concentration and grain boundary hydrogen concentrations. In the end, the MD simulation results are inserted into the Horstemeyer and Gokhale continuum void nucleation model [47], and nanovoid nucleation at different grain boundary hydrogen concentrations and nanovoid nucleation without hydrogen are quantified.

Chapter IV presents MD and MC simulation results of nickel single crystal with hydrogen effects. A novel coupled MD-MC process for modeling hydrogen dynamically-charged conditions is presented. Hydrogen absorption based on MC simulation results is discussed for the hydrogen-precharged and the dynamically-charged cases. The relationship between stress states, dislocation activities and nanovoid nucleation is presented. The MD simulation results are inserted into the Horstemeyer and Gokhale model [47] to associate the void nucleation and hydrogen concentration to aid in the development of a continuum model.

Chapter V presents a continuum damage framework with hydrogen effects, with emphasis on void nucleation. The kinematics of the framework includes decomposition of the deformation gradient into the deviatoric plastic part, the elastic part, the volumetric expansion induced by damage and hydrogen-induced dilatational strain. In the thermodynamics of the framework, the internal state variables include the thermodynamic displacement induced by statistically-stored dislocations and damage, which is a function of hydrogen. In the kinetics of the frameworks, a continuum void nucleation model with hydrogen effects is proposed and used with the equation for calculating hydrogen concentration mentioned in Chapters III and IV and implemented into Finite Element Analysis. The model is correlated with the experimental results [38] of 1518 spheroidized steel smooth specimens in hydrogen-free and hydrogen-charged conditions. The model is then validated with the experimental results [38] of 1518 spheroidized steel notched specimens in hydrogen-free and hydrogen-charged specimens.

Chapter VI summarizes the work performed in this research. Recommendations for future research are also presented.

CHAPTER II

OVERVIEW OF THEORIES AND APPROACHES

2.1 Introduction of Multiscale Material Modeling in Ductile Failure

Multiscale modeling of materials is about performing simulations across several characteristic length and time scales [58]. Length scales can range from quantum ($\sim 10^{-12}$m), through nano ($10^{-12} \sim 10^{-6}$m) to micro ($10^{-6} \sim 10^{-4}$m) and to macro ($10^{-4} \sim 10^{-2}$m) levels. Time scales can range from picoseconds (10^{-12}s), to nanosecond (10^{-9}s), to microsecond (10^{-6}s), to second (s) and to quasi-static regimes. Figure 2.1 shows modeling methods corresponding to different length and time scales.

At the quantum scale, the total energy and atomic structure of a system of electrons and nuclei is predicted. *Ab initio* methods [59] can be used to numerically approximate the Schrodinger equation and calculate many physical properties of materials [60]. Density Function Theory (DFT) [61], a quantum-mechanical method, can be used to calculate material properties such as cohesive energy, surface energy, energy barriers, atomic structure, etc. The DFT method is limited to a few hundred atoms and a simulation time of a few picoseconds.

At the nanoscale, interatomic potentials are developed to reduce the degrees of freedom of electrons at the quantum scale by considering atoms being held by interatomic potentials. Daw and Baskes [51, 62] developed the Embedded Atom Method

(EAM) as energy corrected potentials by fitting parameters from *ab initio* results to experimental data. The corrected parameters include the lattice constant, elastic constants, vacancy formation energy and surface energy. Molecular Dynamics simulations with interatomic potentials can be used to study dislocation nucleation and interactions, interfacial debonding and nanovoid nucleation, growth, and coalescence, MD simulations can simulate up to 10^9 atoms and 100 nm [63], from a few picoseconds to 10 nanoseconds.

At the micron scale, Dislocation Dynamics (DD) methods [64] are used to model dislocations explicitly to study dislocation motion, interactions and dislocation structure formation, because the mechanical behavior of materials depend mostly upon point defects such as vacancies and interstitials, line defects such as dislocations, and surface defects such as voids, cracks and grain boundaries. The mechanical responses from DD simulations can be used in the development of constitutive laws at the continuum scale. Another method at the intermediate length scales is the Statistic Homogenization Mechanics (SHM) [65] methods, which are used to study dislocation cells, shear bands or other organized dislocation structures, in order to develop continuum equations.

At the macroscale, the effects of defects and microstructures on plastic deformation and fracture are represented by a set of internal state variables that are incorporated into the constitutive equations. Those equations are used with other governing equations such as conservation of mass and conservation of linear and angular momentum to solve the stress and strain tensor at each material point.

Currently, two approaches exist to link one scale to another: the hierarchical approach and the concurrent approach. In the hierarchical approach, large-scale models use coarse-grained representations with information obtained from more detailed, small-scale models [60]. In the concurrent approach, different scales of the system are linked explicitly in a combined model and information is passed from one scale to another scale concurrently [66]. A hierarchical approach is used in our research.
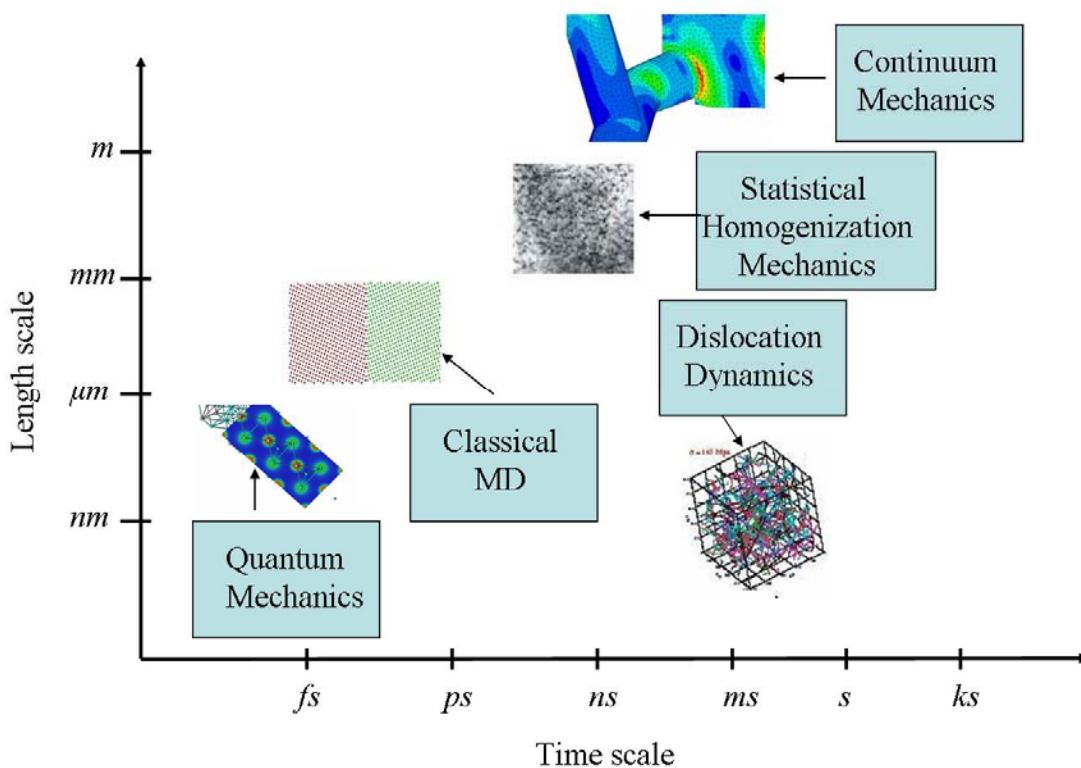
Figure 2.1.   The modeling methods at different length scale and time scale. (Modified from [58]).

2.2   Overview of Molecular Dynamic (MD) simulations

In this research, the MD simulation code used is WARP [67], originally developed by Steve Plimpton and later modified by Gregory Wagner from Sandia National Laboratories. Another code used is PREWARP [67], developed by Phillip Gullett from the Department of Civil Engineering at Mississippi State University, to build grain boundary structures.

2.2.1   Equation of motions

The Molecular Dynamics simulation method has been used to study a dynamic system of particles since the 1960s [68]. The equations of motion can be derived in several ways. Newton's 2'nd Law of Motion can be used for an *N* atom system,

$$F_i^\alpha = m_\alpha \ddot{x}_i^\alpha \quad i=1,2,3 \text{ and } \alpha=1,2\ldots N \tag{2.1}$$

where F_i^α denotes the force in the *i*th direction acting on atom α; m_α denotes the atom's mass and x_i^α denotes the *i*th component of the atom's position. The force F_i^α can also be described as the derivative of the total potential energy *E* with respect to the position of the atom α,

$$F_i^\alpha = -\frac{\partial E}{\partial x_i^\alpha} \tag{2.2}$$

The forms of potential energies include Lennard-Jones [69], Embedded Atom Method (EAM) [51] and Modified Embedded Atom Method (MEAM) [70]. In this research, the EAM potential was used. In a later section, the EAM potential will be described in more detail.

2.2.2 Integration methods

The Leapfrog and Verlet methods are most widely used for integrating the equations of motion in MD simulations [71-72]. These two methods are equivalent algebraically [72].

In the Verlet method, Taylor expansion is used for the atom position *x(t)*,

$$x(t + h) = x(t) + h\dot{x}(t) + (h^2 / 2)\ddot{x}(t) + O(h^3) , \tag{2.3}$$

where *t* is the current time, and *h=Δt*. Taylor expansion is also used for *x(t − h)*,

$$x(t - h) = x(t) - h\dot{x}(t) + (h^2 / 2)\ddot{x}(t) + O(h^4) \tag{2.4}$$

Equation (2.3) is added to Equation (2.4) to obtain,

$$x(t + h) = 2x(t) - x(t - h) + h^2\ddot{x}(t) + O(h^4) \tag{2.5}$$

The velocity term is needed for calculating the kinetic energy and temperature. The velocity term is obtained by subtracting Equation (2.4) from Equation (2.3) as:

$$\dot{x}(t) = [x(t + h) - x(t - h)] / 2h + O(h^2) \tag{2.6}$$

The velocity and position of the atoms can be used to calculate the atomic forces.

2.2.3 Periodic boundary conditions

A very large system of atoms needs to be modeled to study macroscopic phenomena such as hydrogen-enhanced void nucleation. However, even with the super computing power existing today, as mentioned earlier, only a very small system with a limited number of atoms (fewer than 10^9 atoms) can be simulated. To address this problem, periodic boundary conditions are being used.

Periodic boundaries introduce an infinite space-filling array of identical copies of the simulation region, as shown in Figure 2.2 [73]. In Figure 2.2, the black box with black circles is the simulation region and the grey boxes with grey circles are the images of the simulation regions. The black circles are atoms and grey circles are their images. If an atom leaves the simulation region from one face of the black box, shown by the red arrows, it will immediately enter the simulation region from the opposite face, shown by the blue arrows. The atoms near the boundaries of the simulation region have the forces and energies of bulk atoms, because they interact with the periodic image of other atoms. As a result, the small finite system can be used to model bulk properties.
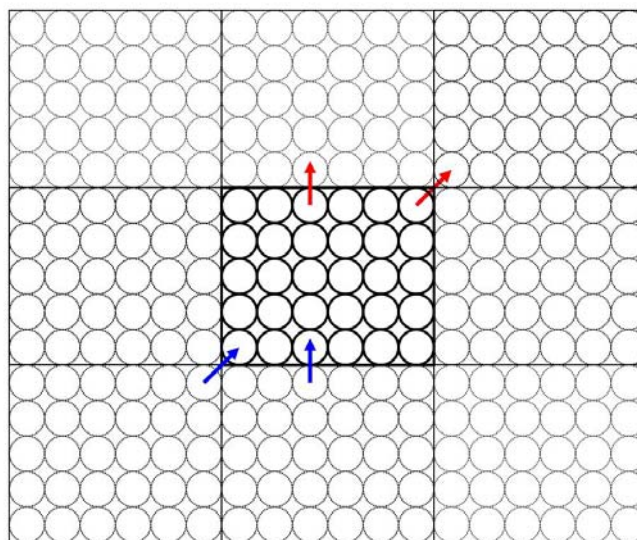
Figure 2.2.   The black box with black circles is the simulation region and the grey boxes with grey circles are the images of the simulation regions. The black circles are atoms and the grey circles are their images. If an atom leaves the simulation region from one face of the black box, shown by the red arrows, it will immediately enter the simulation region from the opposite face, shown by the blue arrows [73].

2.2.4   Constant pressure control

In MD simulations, energy and volume are fixed. However, in experiments, either temperatures or pressures are usually fixed. In our simulations, we impose a constant pressure condition. The constant pressure control is described next.

In MD simulations, the pressure can be adjusted by a uniform isotropic volume change V through rescaling the atomic coordinates [74]. The scaled coordinate r is related to the physical coordinate r' by

$$r = r' \Delta V^{1/3}, \tag{2.7}$$

where ΔV is the cubic volume change. Rather than Newton's 2nd Law of motion, the Lagrangian equation is used to describe the motion. For an isolated N atoms system, the Lagrangian equation is:

$$L = \frac{1}{2} m V^{2/3} \sum_i \dot{r}_i^2 - \sum_{i<j} E(V^{1/3} r_{ij}) + \frac{1}{2} M \dot{V}^2 - PV , \tag{2.8}$$

where m is the atom mass, V is the volume of the system, E is the total potential energy, P is the pressure, and M is a generalized mass parameter, which can be regarded as the mass of a piston that can be used to regulate pressure by altering the volume. Substituting equation (2.8) into the following equation:

$$\frac{\partial L}{\partial t} \left(\frac{\partial L}{\partial \dot{V}} \right) - \frac{\partial L}{\partial V} = 0 , \tag{2.9}$$

and:

$$M\ddot{V} + \frac{m}{3V^{1/3}} \sum_i \dot{r}_i^2 - \sum_{i<j} \frac{\partial E(V^{1/3} r_{ij})}{\partial V} - P = 0 , \tag{2.10}$$

and:

$$P = M\ddot{V} + \frac{m}{3V^{1/3}}\sum_i \dot{r}_i^2 - \sum_{i<j}\frac{\partial E(V^{1/3}r_{ij})}{\partial V}, \tag{2.11}$$

where P is the external pressure of the system.

2.2.5 EAM potential

The EAM potentials [51] are based on a semi-empirical method. In this method, the total energy of a metallic solid is composed of the sum of pair potential energies, E_p, plus the sum of the energies to embed each atom into the local electron density of neighboring atoms, F,

$$E = \sum_{i,j>i} E_p(R_{i,j}) + \sum_i F(\sum_{j\neq i}\rho(R_{i,j})), \tag{2.12}$$

where i refers to the atom in question and j refers to neighboring atoms. The first term is the pair interaction energies between two atoms separated by a distance $R_{i,j}$. The second term is the sum of the embedding energies of atom i in the electron density ρ_j.

The EAM Nickel-Hydrogen (Ni-H) potentials [75-76] were used in the simulations. The elastic constants calculated from this potential, matches well with the experimental data [77]. The vacancy formation energy also matches well with the experimental data [78]. However, the stacking fault energy predicted from the potential is only 89 erg cm^{-2}, smaller than the experimental value of 125 erg cm^{-2} for pure nickel [79]. In FCC materials, the lower the stacking fault energy, the greater the separation between the partial dislocations, resulting in a wider stacking fault [80]. Metals with high stacking fault energy have a deformation substructure of dislocation tangles and cells. Metals with low stacking fault energy have a deformation substructure of banded, linear

arrays of dislocations [79]. The predicted lower stacking fault energy may cause more banded deformation substructures. The deformation substructure will be discussed in detail in the future.

2.2.6 *Definition of bulk quantities*

One of the purposes for performing MD simulations is to study the mechanical properties of materials. In many cases, bulk quantities, such as stress and strain tensors need to be estimated. In MD simulations, the explicit output includes the force and velocity of each atom. The following section shows how a continuum-like stress tensor is calculated from atomic forces.

At each atom, the dipole force tensor is defined as a second rank tensor,

$$f_{ij}^{k} = \frac{\partial E}{\partial r_{ij}^{k}} \,, \tag{2.13}$$

where the superscripts denote the rank of the tensor and the subscripts denote the atom counting system. f_{ij}^{k} is the force vector between atoms. r_{ij}^{k} is a position vector between atoms i and j. The stress tensor at the atom i is defined as,

$$\beta_{i}^{km} = \frac{1}{\Omega_{i}} \sum_{j \neq i}^{N} f_{ij}^{k} r_{ij}^{m} \tag{2.14}$$

where N^{*} is the number of nearest neighbor atoms, and Ω_{i} is the atomic volume. A continuum-like stress tensor is defined for the bulk specimen as,

$$\sigma^{km} = \frac{1}{N^{*}} \sum_{i=1}^{N^{*}} \beta_{i}^{km} \tag{2.15}$$

2.2.7   Monte Carlo (MC) methods

The MC methods were developed by Metropolis and coworkers [81]. Monte Carlo simulations with EAM potentials can be used to find equilibrium positions and compositions of a material system at the given temperature, thermal expansion and thermodynamic state. In Ni-H systems, hydrogen concentrations correspond to different applied chemical potentials. In this research, MC simulations were performed to introduce hydrogen atoms in the specimens. The details on how hydrogen atoms are introduced into the nickel specimens are described in [52].

2.2.8   Common Neighbor Analysis (CNA)

In this study, a Common Neighbor Analysis (CNA) method [82] was used with MD simulations to identify local FCC and HCP lattice structures. By studying the local lattice structure through the CNA method, stacking faults, partial dislocations, and deformation twins were identified during the deformation process. The details of the CNA method can be found in references [82-83]. The CNA code used in this research was developed by Srinivasan G. Srivilliputhur from Los Alamos National Laboratory.

2.3   Continuum Damage Mechanics (CDM)

The CDM is developed based on a macroscopic damage variable, ϕ, which was initially proposed by Kachanov [84] and Robotnov [85]. Damage, ϕ, can be an internal state variable used to link the evolution of voids and cracks in the microscale to the constitutive equations in the continuum scale. One important concept related to this variable is a Representative Volume Element (RVE). An RVE is a material volume

which is a statistical representation of a material neighborhood of a material point [86]. Figure 2.3 shows how a volume element with heterogeneity, such as voids/cracks, is replaced by a continuum element.

(a)   (b)
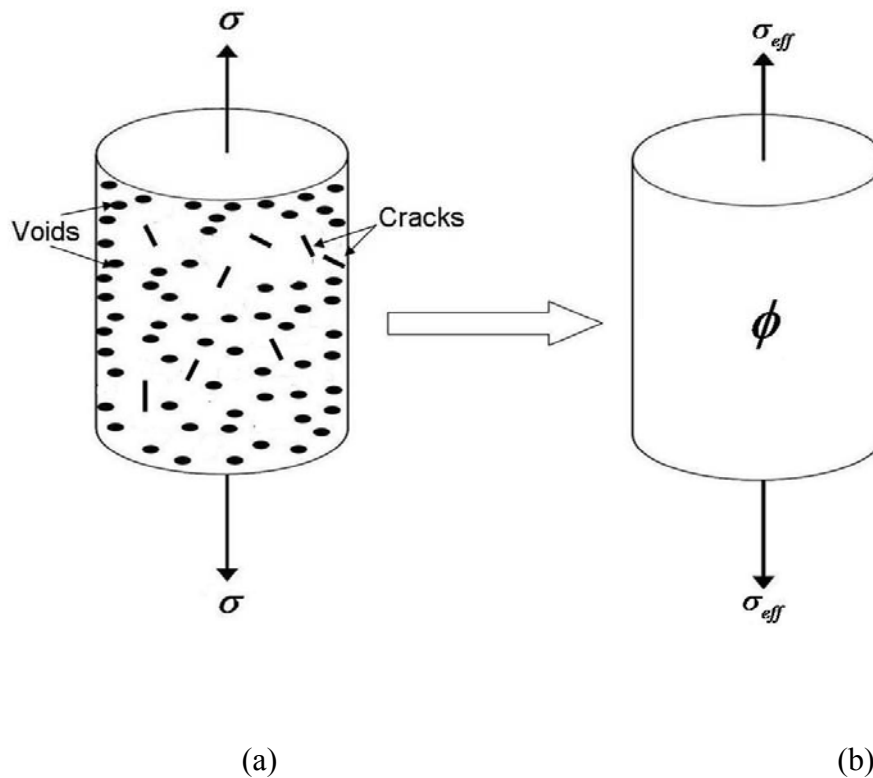
Figure 2.3.   RVE includes microvoids/cracks in (a), and is replaced with a continuum element (b) with an internal state variable, damage variable ϕ, to account for the effects of microvoids/cracks in the constitutive equations.

Because the cracks and voids are oriented, the damage variable can be a tensor. However, for a case of isotropic damage, the damage variable is a scalar and is defined by the volume fraction or area fraction of voids or cracks in a volume element. When damage is zero, the volume element is in an undamaged state; when damage is less than

one, the volume element is in a damaged state; when damage is one, the volume element is considered to be ruptured.

Damage can cause an increase in the effective stress of the volume element [87]. In uniaxial case, shown in Figure 2.3,

$$\sigma_{eff} = \frac{\sigma}{1-\phi} , \tag{2.16}$$

where σ_{eff} is the effective stress of a damaged volume element, σ is the stress of an undamaged volume element. This relationship is used in constitutive equations of the undamaged material to modify the strain behavior of the damaged element.

Elastic strain $\quad \varepsilon_e = \dfrac{\sigma_{eff}}{E} = \dfrac{\sigma}{(1-\phi)E}$, $\tag{2.17}$

Plastic strain $\quad \varepsilon_p = \left(\dfrac{\sigma_{eff}}{K}\right)^M = \left(\dfrac{\sigma}{(1-\phi)K}\right)^M$, $\tag{2.18}$

where E is the Young's modulus, and K and M are material coefficients. Damage degrades the elastic modulus and enhances plastic flow, as described in Equations (2.17) and (2.18) [87].

Ductile failures involve void nucleation, growth and coalescence. Damage is defined as the ratio of the change of volume in the intermediate state to total volume in the intermediate state [88]. The specimen is unloaded elastically at the intermediate state.

$$\phi = \frac{V_v}{V_o + V_v} \tag{2.19}$$

V_o is the volume of the element at its initial state. V_v is the volume change at its intermediate state. Void nucleation, η, is the total number of voids nucleated in the intermediate state, N_η, divided by the volume of the material in its intermediate state.

$$\eta = \frac{N_\eta}{V_0 + V_v} \qquad (2.20)$$

The average void volume is v_v. The total volume of the voids is,

$$V_v = N_\eta v_v \qquad (2.21)$$

Therefore,

$$\phi = \eta v_v \qquad (2.22)$$

CHAPTER III

HYDROGEN EFFECTS ON NANOVOID NUCLEATION AT NICKEL GRAIN BOUNDARIES

3.1   Introduction

Hydrogen enhances material damage in ductile materials [28-31]. Because hydrogen affects the damage state, one must consider the effects of the stress and strain states on the damage state of the material. Molecular Dynamics (MD) simulations have revealed a size scale effect related to dislocation nucleation influencing the yield stress as a function of the volume per surface area [89-92]. Alternatively, other MD studies related to kinematic/geometrical effects, nanoscale fracture, and nanoscale fatigue have shown no size scale effects and have revealed self-similar, scale invariant behavior. Three examples illustrate no size scale dependence related to kinematics/geometry/strain. Horstemeyer and coworkers [93] performed macroscopic single crystal experiments of copper and compared the results to MD and microscale crystal plasticity simulations for torsion and simple shear. The results showed similar strains and gradients of strain at all size scales although the stress states were different. In [94], the simple shear simulations were performed in MD, microscale crystal plasticity, and macroscale internal state variable plasticity, showing very similar strain states, but differing stress states as afunction of size scale. In [95], macroscale experiments of imploding rings were

24

compared to MD simulations and microscale crystal plasticity simulations. Again, although the geometry changes, strain levels and strain gradients were similar in all cases. In terms of fatigue, researchers employing MD [96-97] have shown that nanoscale crack growth rates are similar to microcrack growth rates with the same mechanisms existing at all size scales. In terms of void growth, MD simulations [98] were performed that showed size scale effects in the elastic regime, but that a scale invariance quickly developed as plasticity was induced, arising from the nucleation, movement, and interaction of dislocations. Hence, the question arises regarding hydrogen effects on nanovoid nucleation: hydrogen effects on nucleation size scale dependent like the stress state or are they size scale independent, like the geometric quantities, or is it a combination of both?

The mechanisms proposed for hydrogen-related failures include a stress-induced hydride formation mechanism, a Hydrogen-Enhanced Localized Plasticity (HELP) mechanism, a hydrogen-induced decohesion mechanism, and a stacking fault mechanism. Any of these mechanisms can promote hydrogen effects on microvoid nucleation at grain boundaries and interfaces, as illustrated in 310 Stainless Steel [40], spheroidized carbon steels [28-31, 36-38], nickel alloys [35] and 7000 series aluminum alloys [39]. Liang and Sofronis [48] performed micromechanical simulations to study interface debonding of a carbide particle embedded in a nickel matrix with hydrogen and found that hydrogen caused the voids to nucleate at a lower applied strain. Although these experimental and modeling studies have indicated the importance of hydrogen on void nucleation at grain boundaries and interfaces, to understand the hydrogen effects on void nucleation at the

microscale and macroscale, the underlying mechanisms at the atomic scale must be understood [99]. Moody and coworkers [100] performed MD calculations to study hydrogen effects on the debonding of symmetrical $\Sigma 9$ and asymmetrical $\Sigma 9$ nickel tilt grain boundaries, and found that hydrogen caused a marked reduction in fracture stress due to strong hydrogen trapping at the grain boundaries. Tanguy and coworkers [101] also performed MD simulations of hydrogen segregation on a $\Sigma 5$ (310)[001] aluminum tilt grain boundary, and the results showed that high local hydrogen concentrations induced a large separation at the interface, which caused a lower fracture stress at the interface.

In this chapter, hydrogen absorption and distribution, and their effects on nanovoid nucleation at different local geometries were studied. The purpose of this study is to look into a possible quantitative relationship between nanovoid nucleation, local hydrogen concentrations, and local grain boundary geometries to help develop a continuum void nucleation model with hydrogen. Sato and coworkers [102] found that hydrogen embrittlement of Ni-based Alloy 600, with coarse columnar crystals, depended on grain boundary orientations. Pan and coworkers [103] counted cracked grain boundaries due to stress corrosion and found that grain boundaries with certain Coincident Site occurrence Lattice (CSL) numbers cracked more than the others. Note that stress corrosion is usually related to hydrogen embittlement [104]. Those experiments show the importance of grain boundary orientation in hydrogen-induced failure. To simplify this study, three specimens were chosen: a single crystal nickel, which may be regarded as a grain boundary with a misorientation angle of 0^0, a low angle

Σ257 (1610)[001] tilt grain boundary with a misorientation angle of 7.14^o and a high angle Σ5 (310)[001] tilt grain boundary with a misorientation angle of 36.7^o. Dislocation spacing, instead of the CSL number, is usually used to describe low angle grain boundaries. The CSL number was used to describe the low angle grain boundary only for consistency and simplification. Monte Carlo (MC) simulations [52, 81] were performed to introduce hydrogen atoms into the specimens. Molecular Dynamics (MD) simulations were performed to study how hydrogen affects the nanovoid nucleation in these local geometries. Finally, the results were inserted into the Horstemeyer-Gokhale continuum void nucleation model [47], and hydrogen effects on the nanovoid nucleation rate were discussed.

3.2   Simulation setup and computational approach

3.2.1   Grain boundaries

Grain boundaries are the interfaces that separate neighboring misoriented single crystals in a polycrystalline solid. Based on the extent of the misorientation between two grains, grain boundaries can be categorized as low angle grain boundaries or high angle grain boundaries. A low angle grain boundary generally is composed of an array of dislocations; its properties and structure are a function of the misorientation angle. One of the important properties is *dislocation spacing*. Figure 3.1 shows the schematic of a symmetrical low angle tilt grain boundary, where, *D* is the dislocation spacing, *b* is the Burger's vector and *θ* is the misorientation angle. As the misorientation angle increases, the cores of the dislocations begin to overlap, and the grain boundary becomes a high

angle grain boundary. The high angle grain boundary includes regions of good and bad fits between two grains. Based on this concept, the Coincidence Site Lattice (CSL) (Σ) numbers are used to describe a high angle grain boundary. Figure 3.2 shows a schematic of a $\Sigma5$ model in which one in five lattice sites of two grains are coincident. In Figure 3.2, the lattice sites of one grain are represented by red dots and the lattice sites of another grain are represented by yellow dots. The coincident lattice sites of both grains are represented by green dots.
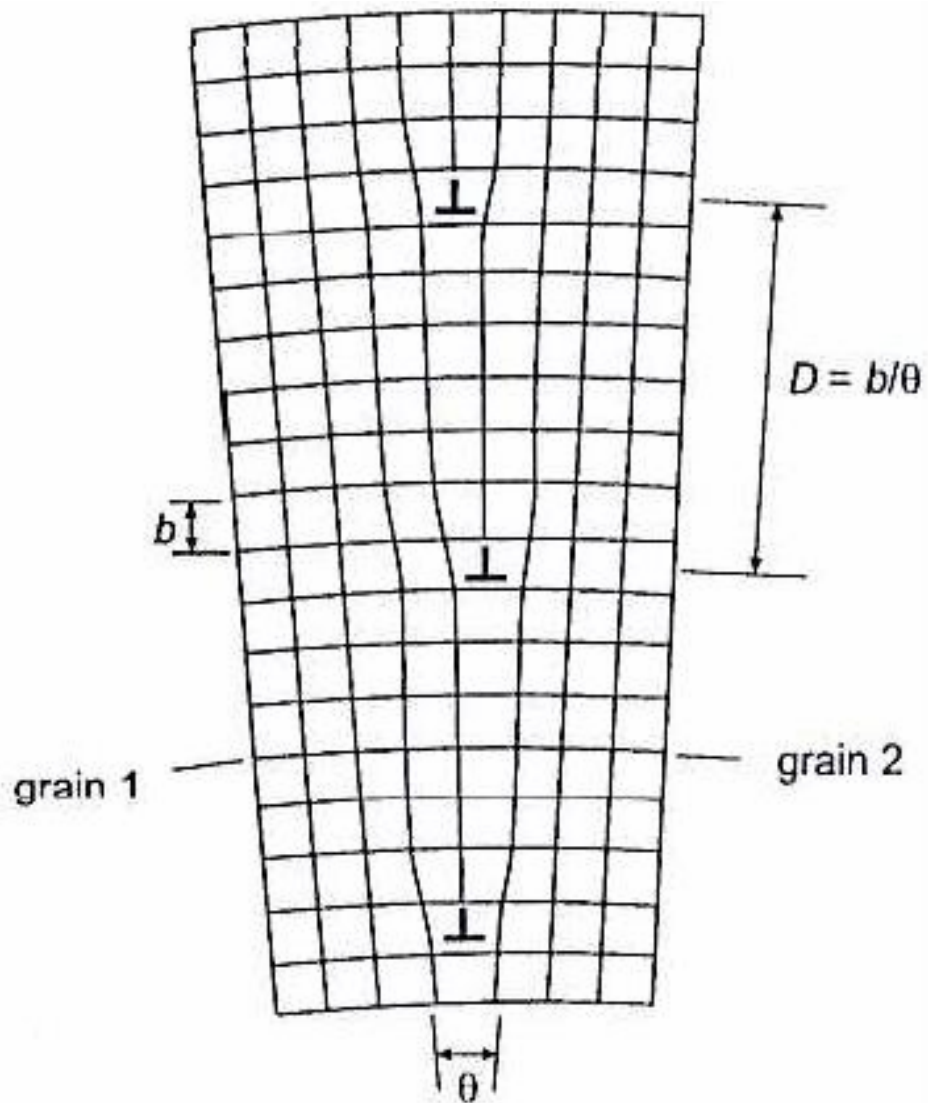
Figure 3.1.   A symmetrical tilt grain boundary consists of a vertical array of edge dislocations with parallel Burgers vectors. This schematic is from Hull and Bacon[105].
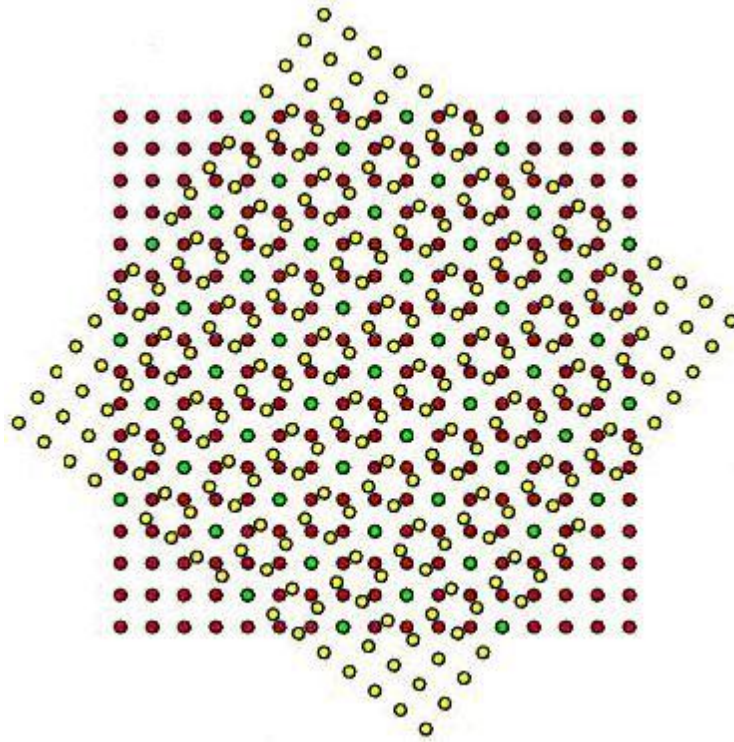
Figure 3.2.   A schematic of a Σ5 Coincident Site Lattice (CSL) model shows that one in five lattice sites of two grains are coincident.

3.2.2   Simulation parameters

In this study, all specimens were created with approximately the same dimensions. The grain boundary specimens were 22 nm in the direction normal to grain boundary planes, 11 nm and 4.2 nm respectively in the direction of the grain boundary plane. 98800 nickel atoms were created for the low angle Σ257 (1610) [001] tilt grain boundary. 96000 nickel atoms were created for the high angle Σ5 (310) [001] tilt grain boundary. The 96000 atoms were created for a single crystal nickel specimen, which was 22 nm in the [130] direction, 11 nm in the $[3\overline{1}0]$ direction, and 4.2 nm in the [001] direction. Periodic boundary conditions, described later, were applied in all directions.

Figure 3.3 (a) shows the atomic arrangement, dimension and loading direction of a pristine low angle Σ257 [001] grain boundary. Blue represents bulk nickel atoms; the colorful array represents the grain boundary; green arrows represent the loading directions. Figure 3.3 (b) and (c) show the atomic arrangement, dimension and loading direction of a pristine high angle Σ5 [001] grain boundary and a single crystal.
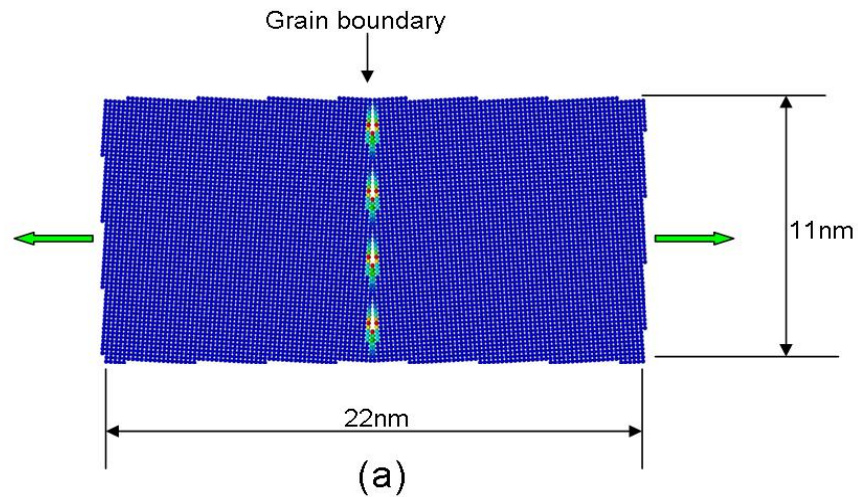
Figure 3.3.   The atomic arrangement, dimension and loading direction of three specimens (a) low angle Σ257, (b) high angle Σ5 and (c) single crystal.

Figure 3.3 (continued)
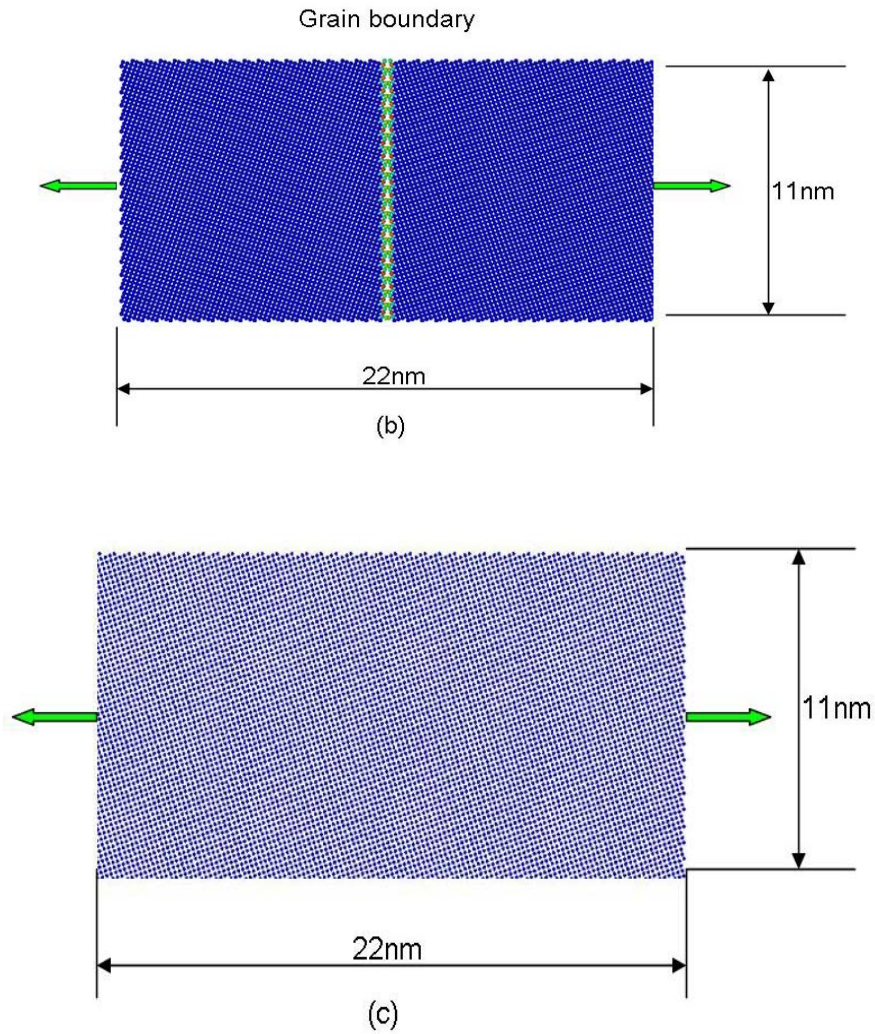
(b)

(c)

The system was brought to thermal equilibrium at 300K at pressure 0 bar. MC simulations were then performed to introduce hydrogen atoms into the specimen by applying a chemical potential. Both grain boundaries were subjected to a strain rate of $5 \times 10^8 s^{-1}$, perpendicular to grain boundary planes, until the specimen failed accompanied by nanovoid nucleation. Single crystal specimens were also subjected to the same strain

rate in the [130] direction. Although the applied strain rate was very high in our MD simulations, in the order of $10^8 s^{-1}$, Moody and coworkers [100] show that Molecular Static (MS) simulation results on nickel grain boundaries were very close to their MD simulation results, which had a strain rate in the order of $10^9 s^{-1}$, which is higher than the strain rate in those simulations.

3.3   Results

3.3.1   *Hydrogen concentration*

MC simulation results are discussed with respect to varying chemical potentials. For each chemical potential applied, the MC simulation was run until the hydrogen concentration saturated, as shown in Figure 3.4, and the system reached a thermodynamic equilibrium state, which corresponds to the state of lowest free energy and zero gradient in chemical potentials. In MC simulations, the applied chemical potential induced a chemical potential gradient that acts as a driving force for hydrogen diffusion, according to Fick's first law [106]:

$$J = -H \frac{D}{RT} \frac{\partial \mu}{\partial x} \tag{3.1}$$

where J is the molar flux of hydrogen atoms, H is hydrogen concentration, D is the diffusion coefficient, and $\dfrac{\partial \mu}{\partial x}$ is the gradient of chemical potential. At the equilibrium state, the gradient of chemical potential reaches zero, and the flux of hydrogen atoms reaches zero, and hydrogen concentration in the system saturates.

Figures 3.5a and 3.5b show the distribution of hydrogen atoms in the high-angle and low-angle grain boundary at the equilibrium state, which show that the majority of hydrogen atoms were located at and near the grain boundary plane in both grain boundaries. However, the hydrogen distribution at the high-angle grain boundary is more homogenous at the grain boundary, and hydrogen atoms were concentrated in clusters in the low-angle grain boundary, which corresponds to the different distribution of defects at the grain boundaries. Researchers [107] illustrated that hydrogen can accumulate at the microstructural heterogeneities such as dislocations, grain boundaries, voids, and surfaces, which are described as traps. The grain boundary hydrogen concentrations are the averaged hydrogen concentrations at and near the grain boundary plane, where hydrogen atoms accumulate. Figure 3.5c shows the distribution of hydrogen atoms in the bulk single crystal at the equilibrium state, which shows that hydrogen atoms were randomly distributed in the specimen, because there were no defects to act as traps. Hydrogen concentrations in the single crystal specimen correspond to the bulk hydrogen concentrations at the different applied chemical potentials. Figure 3.6 shows the bulk hydrogen concentration and grain boundary hydrogen concentration versus applied chemical potentials, and shows that both bulk hydrogen concentrations and grain boundary hydrogen concentrations increased with increased applied chemical potentials. Similar to studies performed by other researchers [100-101], more hydrogen atoms occupied the grain boundary plane and near the grain boundary region and caused much higher grain boundary hydrogen concentrations than the bulk hydrogen concentrations. Figure 3.7 shows the grain boundary hydrogen concentration versus bulk hydrogen

concentration at the grain boundaries. At a low bulk hydrogen concentration (less than 10^{-3} atomic), the grain boundary hydrogen concentration increases rapidly with an increased bulk hydrogen concentration. After the bulk hydrogen concentration exceeds 10^{-3} atomic, the grain boundary concentration increases slowly and saturates when hydrogen atoms fill all of the trap sites at the grain boundaries, which was also demonstrated by Moody and coworkers' simulations [100-101].
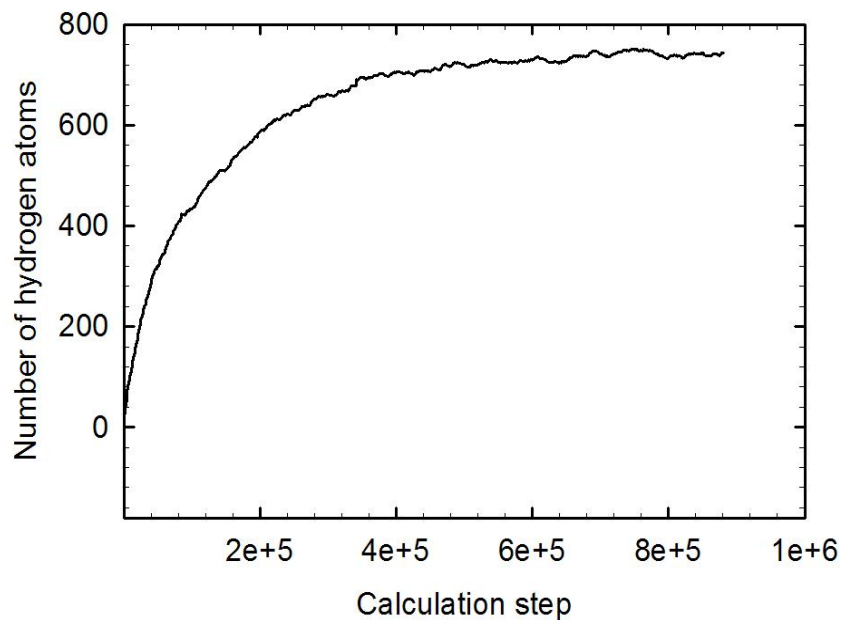
Figure 3.4.   MC simulation results show that the number of hydrogen atoms saturates eventually, which signals that the system reaches an equilibrium state.

McLean [57] related grain boundary hydrogen concentration to bulk hydrogen concentration at an equilibrium state by the following expression:

$$\frac{H_B}{1 - H_B} = \frac{H_L}{1 - H_L} \exp(\frac{-W_B}{RT}), \tag{3.2}$$

where H_B is the grain boundary hydrogen concentration, H_L is the bulk hydrogen concentration, W_B is trap binding energy of hydrogen at the grain boundary trapping sites, R is ideal gas constant, and T is the absolute temperature. Because the trap binding energy is not the same for each trap site, with higher trap binding energy at grain boundary planes and lower trap binding energy at near grain boundary planes, an effective trap binding energy were introduced to address the averaged trap binding energy at a grain boundary from the MC simulation results. Figure 3.7 shows the effective trap binding energy versus the bulk hydrogen concentration for both low angle and high angle grain boundaries. At a low bulk hydrogen concentration, the effective trap binding energy was high (around -0.28 ev) and hydrogen occupied deep traps such as grain boundary planes. With an increased bulk hydrogen concentration, the effective trap binding energy decreased and most of the hydrogen filled up the weak trap sites, where the trap binding energy was around -0.05ev. Figure 3.7 also shows that the effective trap binding energies were nearly the same for both low angle and high angle grain boundaries.
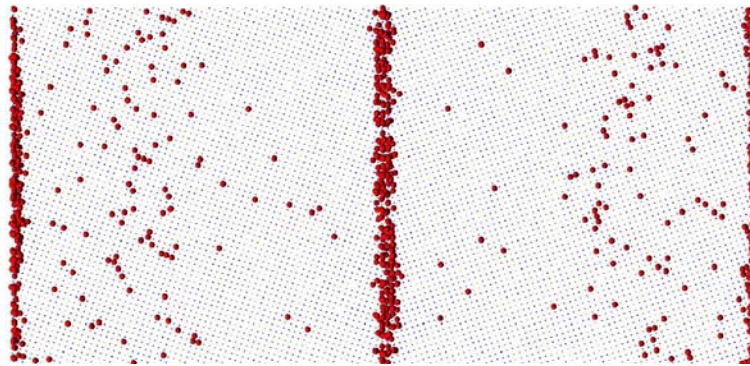
(a)
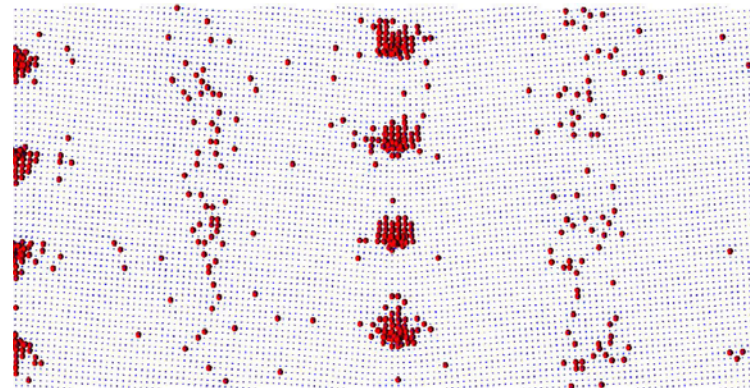
(b)

Figure 3.5.   MC simulation results show that hydrogen atoms accumulate at and near nickel Σ5 grain boundary planes, shown in (a), and concentrate at the defects at nickel Σ257 grain boundary, shown in (b), and are randomly distributed in the nickel bulk single crystal, shown in (c). Hydrogen atoms are shown as red balls.

Figure 3.5 (continued)
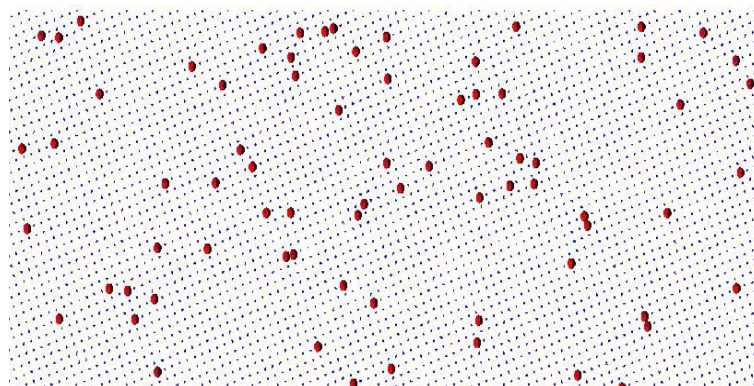
(c)
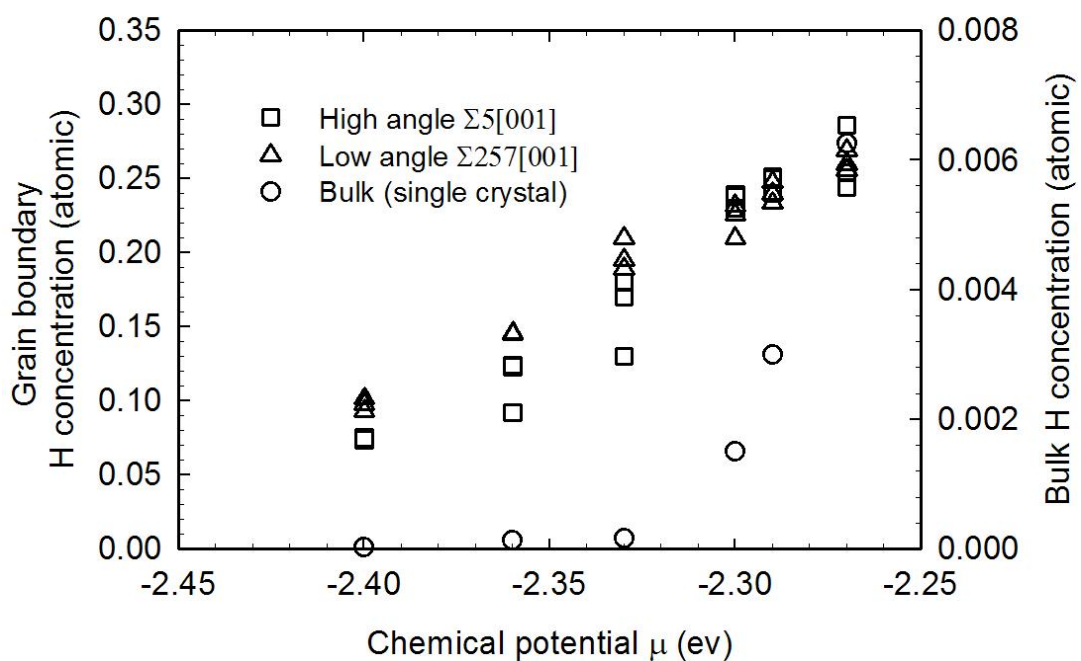
Figure 3.6.   MC simulations show that the bulk and grain boundary hydrogen concentrations increase with increasing chemical potential. More hydrogen atoms are introduced in the grain boundary specimens than in the single crystal nickel specimens to reach the same chemical potential. Also, the grain boundary hydrogen concentrations are nearly the same for both low angle ($\Sigma 257$) and high angle ($\Sigma 5$) grain boundary specimens.
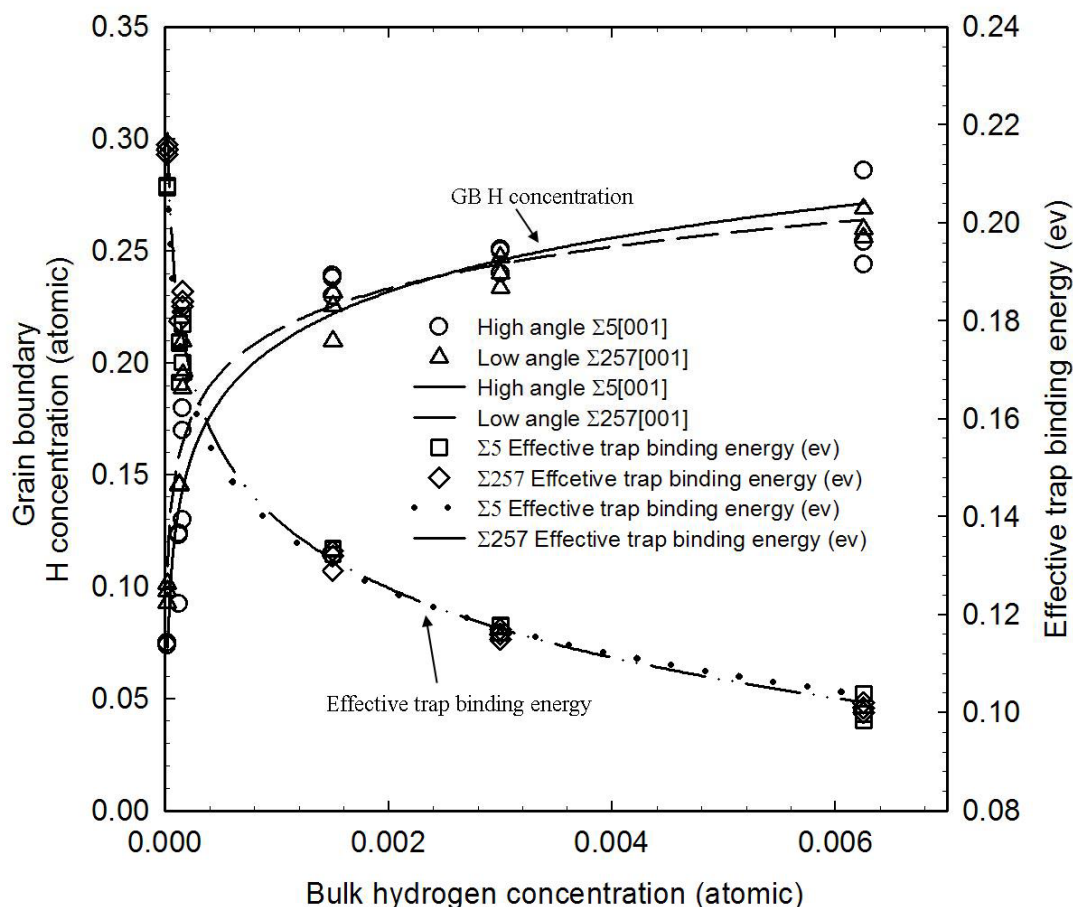
Figure 3.7.   MC simulations reveal the relationship between the grain boundary hydrogen concentration, the effective trap binding energy, and the bulk hydrogen concentration. At a low bulk hydrogen concentration (less than 10^{-3} atomic), the grain boundary hydrogen concentration increases rapidly with an increased bulk hydrogen concentration. The grain boundary concentration then increases slowly and saturates when hydrogen atoms fill all the trap sites. Correspondingly, the effective trap binding energy decreases with an increasing bulk hydrogen concentration.

3.3.2   *Stress-strain responses*

Figure 3.8 shows the stress-strain response and CNA snap shots at different stages

of deformation in the hydrogen-free and hydrogen-charged cases of single crystal nickel.

In both cases, the specimens deformed elastically until some dislocations nucleated at

approximately 8% strain. The yield point definition was defined as macroyield by Horstemeyer and coworkers [89-92]. The tensile stress then dropped slightly until dislocations spread throughout the entire specimen. This stress drop is similar to single crystal whisker responses [89-92]. The tensile stress continued to increase with increasing applied strain and then dropped sharply, because a nanovoid nucleated at the peak tensile stress. The critical tensile stress for nanovoid nucleation was approximately 7% lower, and the critical strain was approximately 4% lower in the hydrogen-charged case than in the hydrogen-free case. The location of the nanovoid nucleation was different in each specimen in the hydrogen-charged case, because hydrogen was distributed randomly in the specimen, and the nanovoid nucleation can occur at a random location. Figure 3.8 shows that the CNA snap shots for the hydrogen-free and hydrogen-charged cases were similar, indicating that hydrogen has a minimal affect on the overall plasticity.
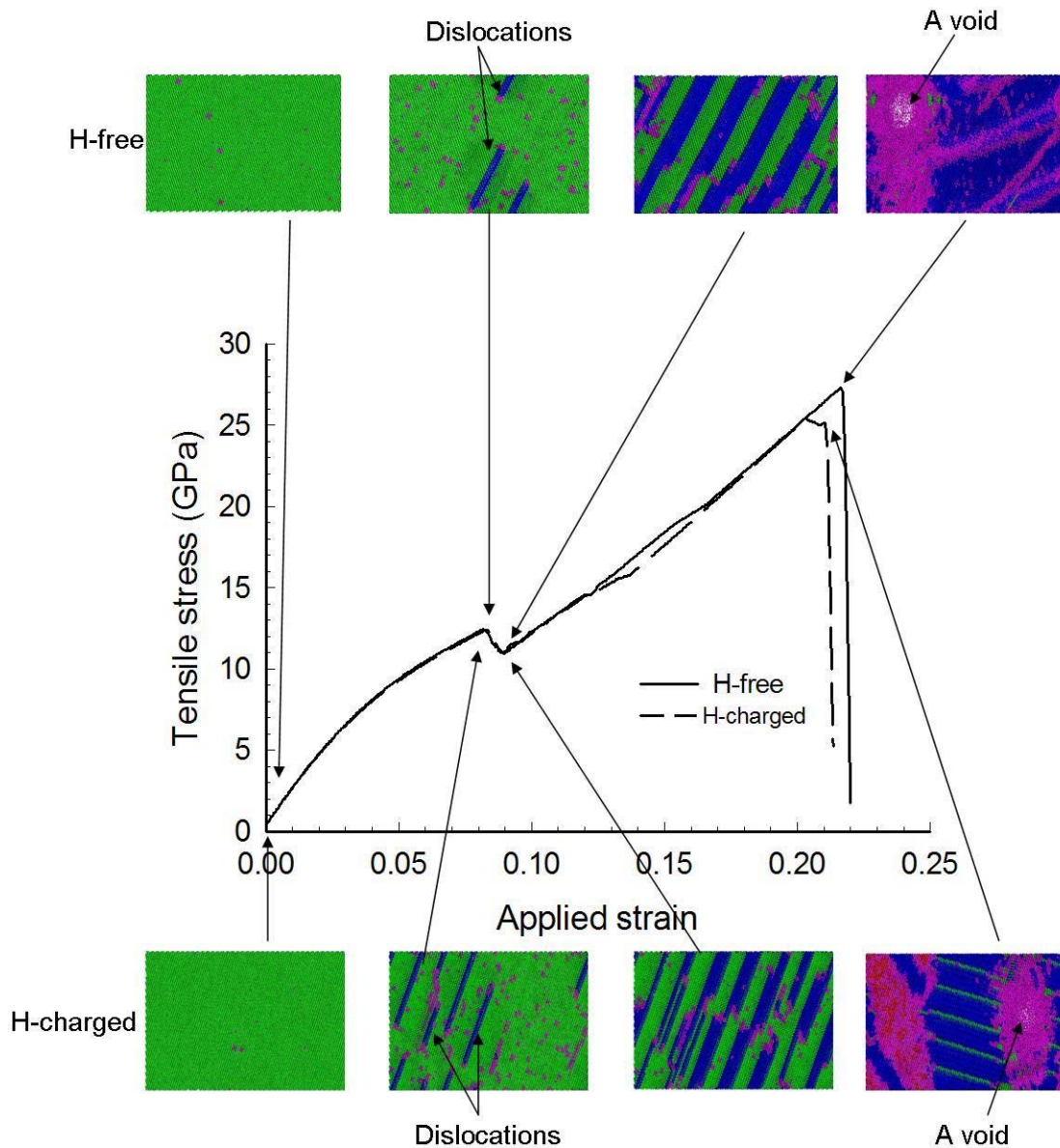
Figure 3.8.   MD simulation results show the tensile stress versus applied strain and corresponding CNA snap shots in single crystal nickel for H-free and H-charged conditions at 300K. The specimen is subjected to a strain rate of $5 \times 10^8 s^{-1}$ in the [130] direction. The CNA snap shots show the full specimen domain. The color green represents the local FCC structure, the color blue represents the local HCP structure, and the color pink is an unknown lattice structure. The dislocation substructure and void damage are illustrated clearly.

Figure 3.9 shows the stress-strain response and CNA snap shots at different stages of deformation in the hydrogen-free and hydrogen-charged cases of the low angle Σ257 [001] tilt nickel grain boundary. In the hydrogen-free condition, the grain boundary structure was defined by an array of dislocations, with the cores shown in pink. With increasing stress and strain, partial dislocations nucleated from the grain boundary at the yield point. Similar to the stress-strain response in the case for pure nickel with no grain boundary, the stress then dropped and more dislocations nucleated until dislocations developed in the entire specimen. The stress increased continuously and then dropped sharply accompanied by nanovoid nucleation at the intersection of dislocations at the grain boundary. In the hydrogen-charged condition, dislocations nucleated at the grain boundary at the yield point, which has nearly the same stress and strain level as in the hydrogen-free condition. As deformation proceeded, the stress and strain continued to increase until the specimen failed, initiated by nanovoid nucleation at the grain boundary. The critical stress for nanovoid nucleation was nearly 32% lower and the critical strain was approximately 29% lower in the hydrogen-charged case than in the hydrogen-free case.
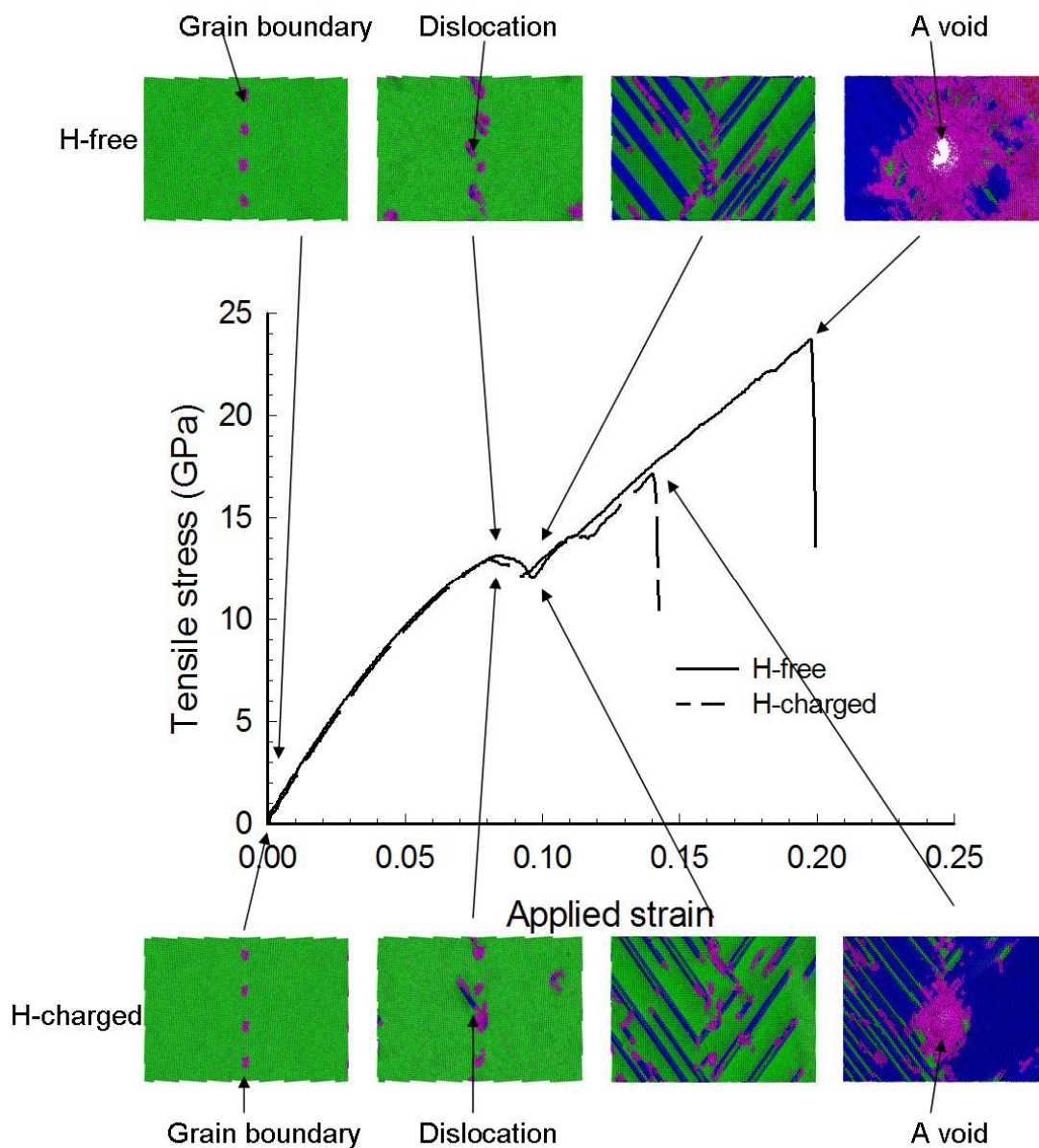
Figure 3.9.   MD simulation results show the tensile stress versus applied strain and corresponding CNA snap shots in a low angle $\Sigma257$ [001] tilt nickel grain boundary at H-free and H-charged conditions. The specimen is subjected to a strain rate of $5\times10^8 s^{-1}$ normal to the grain boundary plane. The CNA snap shots show the full specimen domain. The color green represents the local FCC structure, the color blue represents the local HCP structure, and the color pink is an unknown lattice structure.

Figure 3.10 shows the stress-strain response and CNA snap shots at different stages of deformation in the hydrogen-free and hydrogen-charged cases of a high angle Σ5 (310) [001] tilt nickel grain boundary. Figure 3.10 shows that the elastic regimes had identical stress-strain responses, but the plastic regimes were different after yielding, which was signified by partial dislocations nucleating at the grain boundary. However, the yield stress in the hydrogen-charged case was slightly higher than in the other cases. Similar to the single crystal and the low angle Σ257 [001] tilt nickel grain boundary, after yielding, the tensile stresses dropped slightly while more dislocations were nucleated. The tensile stress increased again after dislocations spread over the entire specimens. The stress-strain responses were very similar for each case until specimen failure caused by nanovoid nucleation at the peak tensile stress occurred. The critical tensile stress for nanovoid nucleation was approximately 32% lower and the critical strain was approximately 30% lower in the hydrogen-charged specimen than in the hydrogen-free specimen. The nanovoids nucleated at the grain boundaries for the hydrogen-free and hydrogen-charged specimens. The CNA snap shots in Figure 3.10 were also similar for the hydrogen-free and hydrogen-charged specimens.

The stress-strain responses and dislocation evolution from Figures 3.8-3.10 show that work hardening rate and dislocation evolution prior to nanovoid nucleation was not changed significantly by hydrogen in either single crystal or grain boundary specimens. Boniszewski and Smith [108] also observed similar effects at very low temperatures.
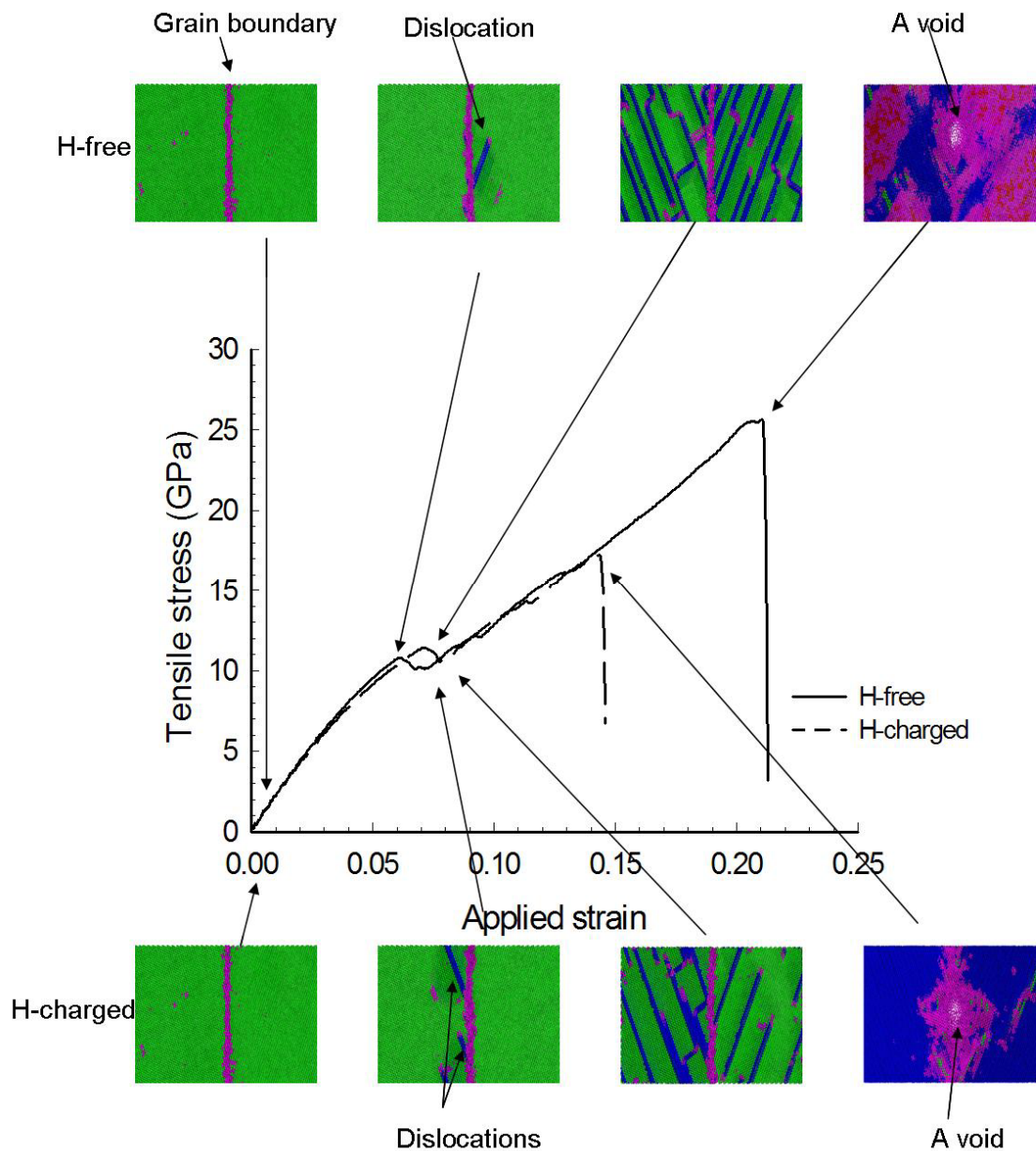
Figure 3.10. MD simulation results show the tensile stress versus applied strain and corresponding CNA snap shots in a Σ5 (310)[001] tilt nickel grain boundary for H-free and H-charged conditions. The specimen is subjected to a strain rate of $5 \times 10^8 s^{-1}$ normal to the grain boundary plane. The CNA snap shots show the full specimen domain. The color green represents the local FCC structure, the color blue represents the local HCP structure, and the color pink is an unknown lattice structure.

3.3.3   Hydrogen effects on nanovoid nucleation

Figures 3.8-3.10 show that the nanovoid nucleation occurred at a critical stress and a critical strain followed by abrupt failure. Several repeated simulations were run to address the statistical issues related to the variation in number and location of the hydrogen atoms at any given chemical potential.

Figure 3.11 shows the critical tensile stress required to nucleate a nanovoid versus bulk hydrogen concentration for a single crystal specimen and grain boundary specimens. For single crystal nickel, hydrogen caused little change to the nanovoid nucleation stress with increasing bulk hydrogen concentration. However, the critical tensile stress required to induce a nanovoid arising in the grain boundary specimens was reduced by hydrogen. In single crystals, there was no hydrogen enrichment, because neither tensile hydrostatic stresses nor defects were present at the beginning of the simulations.   In the grain boundary specimens, the grain boundaries acted as trap sites, and hydrogen was enriched at the grain boundaries reducing the interfacial strength, which is consistent with experimental results [109-110]. Figure 3.12 shows the critical tensile stress at nanovoid nucleation versus grain boundary hydrogen concentrations for both high angle and low angle grain boundaries, and shows that the critical tensile stress for nanovoid nucleation decreased with increasing grain boundary hydrogen concentration; and that the reduction on nanovoid nucleation stress was slightly more in the low angle $\Sigma 257$ [001] tilt grain boundary than in the high angle $\Sigma 5$ [001] tilt grain boundary. Figure 3.13 shows that the critical hydrostatic stress for nanovoid nucleation decreased with increasing grain boundary hydrogen concentration in both grain boundaries.
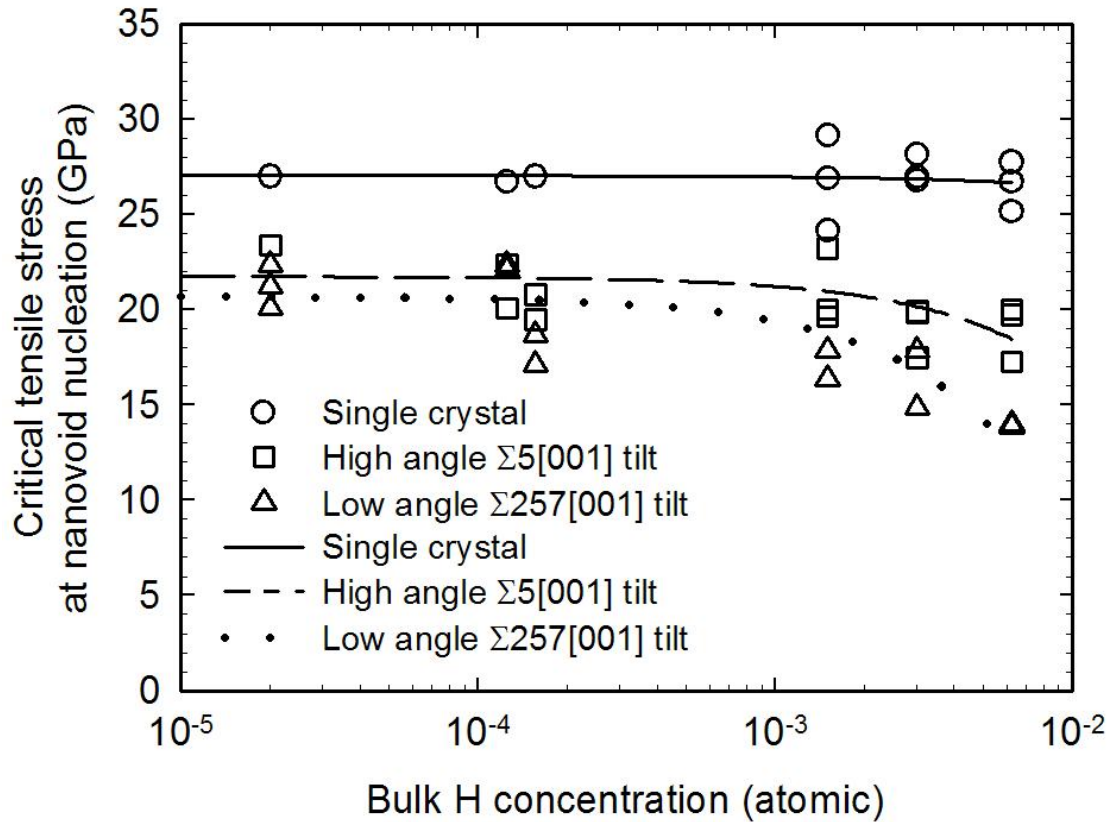
Figure 3.11.   MD simulation results show the critical tensile stress at nanovoid nucleation versus bulk hydrogen concentration for a single crystal, a low angle Σ257 [001] tilt grain boundary and a high angle Σ5 [001] tilt grain boundary. Hydrogen effects on the critical stress for nanovoid nucleation depend on grain boundary geometries and bulk hydrogen concentrations. The scatter is caused by the statistical nature of hydrogen trapping.
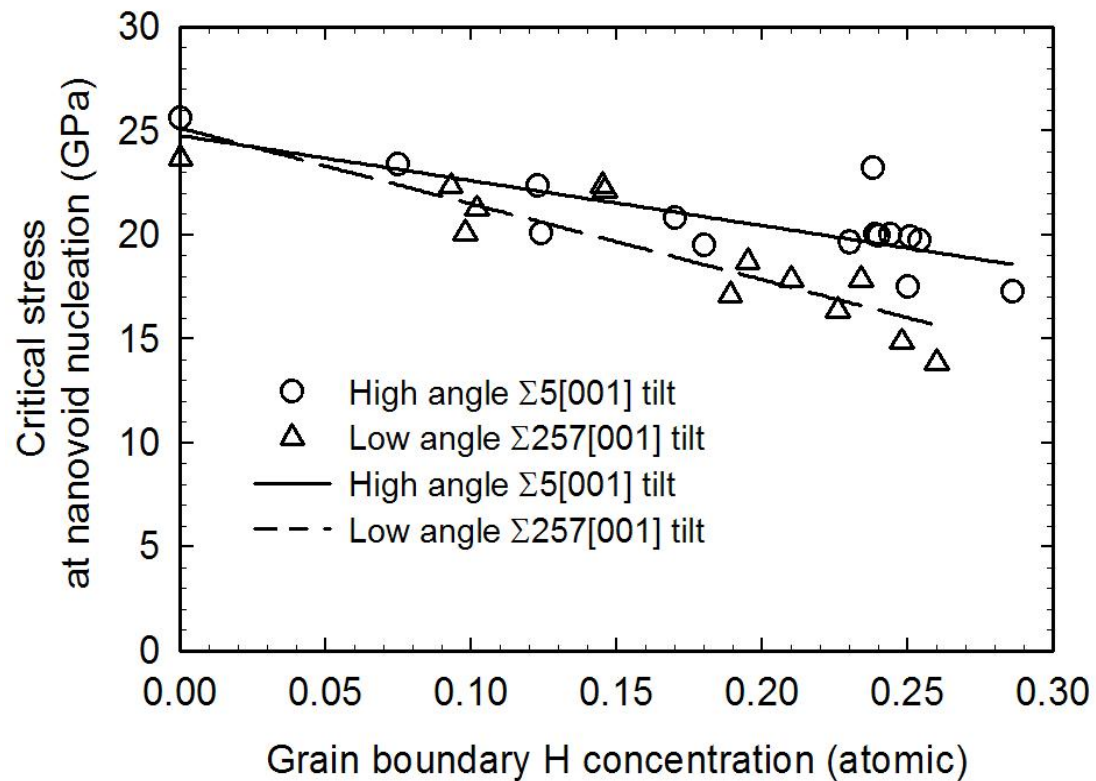
Figure 3.12. MD simulation results show the critical stress at nanovoid nucleation versus grain boundary hydrogen concentrations for a low angle Σ257 [001] tilt grain boundary and a high angle Σ5 [001] tilt grain boundary. The reduction is slightly more pronounced in the low angle Σ257 [001] boundaries than the high angle Σ5 [001] boundaries.
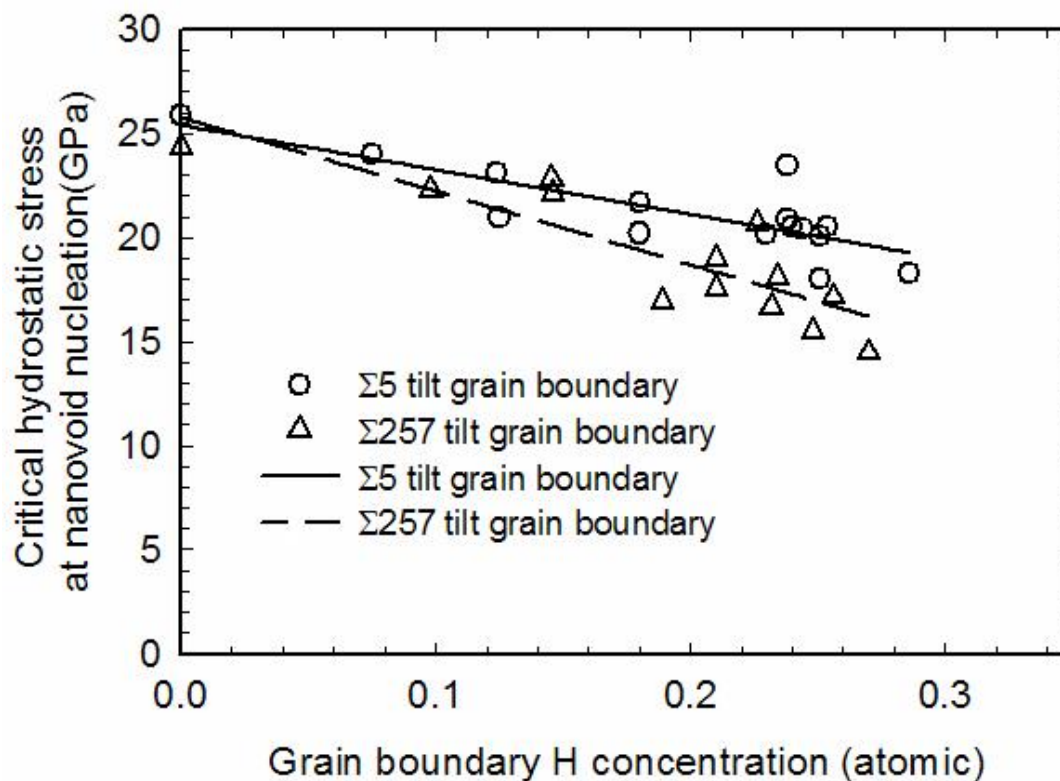
Figure 3.13.   MD simulation results show that the critical hydrostatic stress at nanovoid nucleation decreased with increasing grain boundary hydrogen concentration in both low angle and high angle grain boundaries.

Figure 3.14 shows the critical strain at nanovoid nucleation versus bulk hydrogen concentration for all three specimens. The critical strain in the single crystal was changed very little by hydrogen. The critical strains in both grain boundaries were reduced, clearly tying the hydrogen enrichment at the grain boundaries to the reduction of the strain to failure. Figure 3.15 shows the critical strain at nanovoid nucleation versus grain boundary hydrogen concentration for grain boundary specimens. Figure 3.15 shows that the critical stress at nanovoid nucleation decreased with increasing grain boundary

hydrogen concentration; the nanovoid nucleation stress decreased more rapidly in the low angle Σ257 [001] grain boundary than in the high angle Σ5 [001] tilt grain boundary.

Based on Figures 3.11-3.15, two aspects may have contributed to the different hydrogen effects on nanovoid nucleation and failure. First, hydrogen enrichment in the grain boundaries caused nanovoid nucleation to occur at lower stresses and strains at the grain boundary specimens. Second, even with the same grain boundary hydrogen concentration, the effects of hydrogen on nanovoid nucleation were more pronounced in the low angle Σ257 tilt grain boundary than in the high angle Σ5 tilt grain boundary. The distribution of the hydrogen may have played a role in the mechanical response of the specimen. Figure 3.16a shows the distribution of hydrogen at the grain boundaries before any strain was applied. For the high angle Σ5 grain boundary case, hydrogen concentrated at the grain boundary but was relatively evenly distributed along the grain boundary, because the space of grain boundary dislocation was approximately 0.586 nm based on equation $h = \dfrac{b}{\theta}$, where h is dislocation spacing, b is Burger's vector, and θ is the grain boundary orientation angle [111]. For the low angle Σ257 grain boundary case, the dislocation spacing was approximately 2nm, which is more than five lattice constants and caused hydrogen to concentrate not only at the grain boundary but at dislocation cores as well. Figure 3.16b shows that nanovoids nucleated where hydrogen was concentrated in both grain boundaries. This analysis demonstrates that the effects of hydrogen on nanovoid nucleation depend on grain boundary hydrogen concentration and on the local grain boundary geometry.
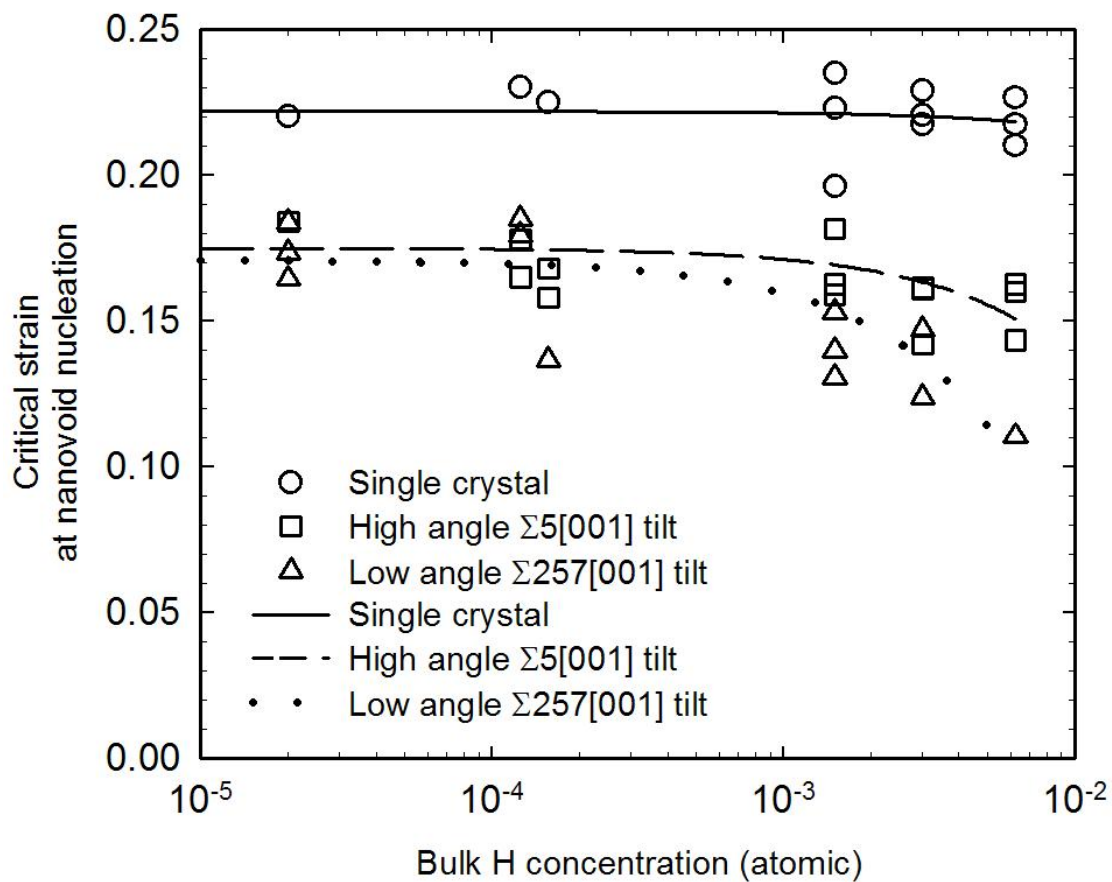
Figure 3.14.   MD simulation results show the fracture strains at nanovoid nucleation versus bulk hydrogen concentration for a single crystal, a low angle Σ257 [001] tilt grain boundary and a high angle Σ5 [001] tilt grain boundary.
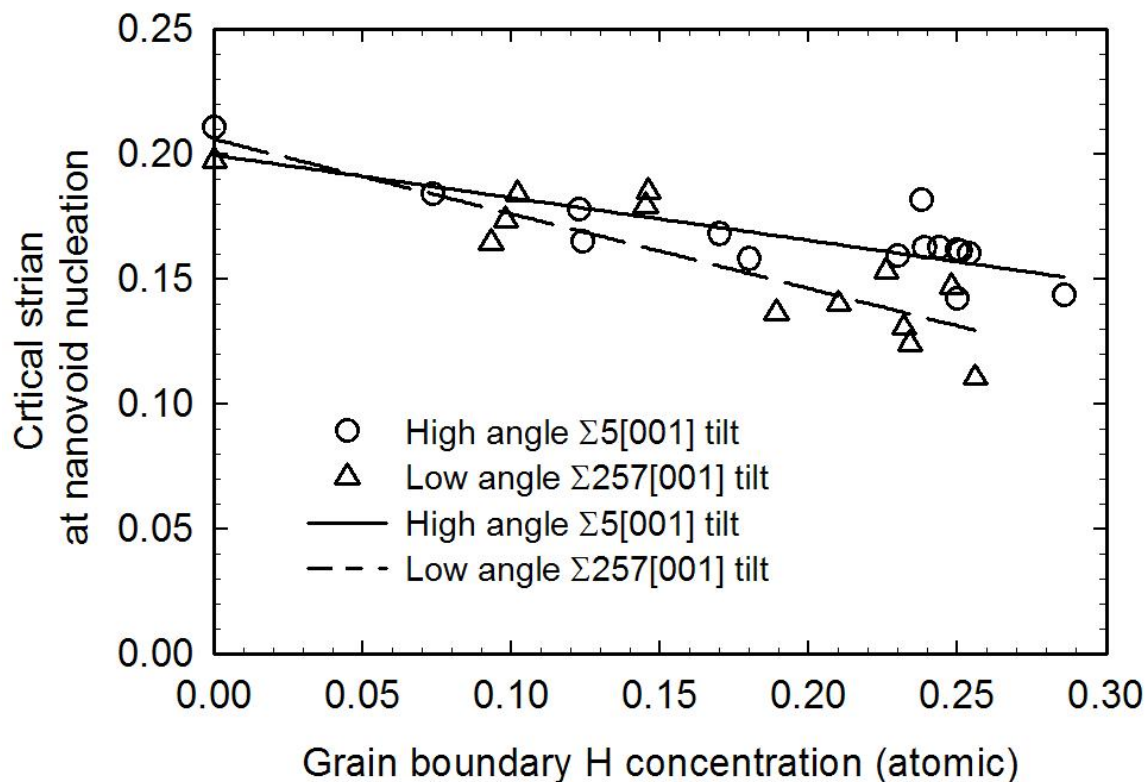
Figure 3.15.   MD simulation results show the critical stresses at nanovoid nucleation versus grain boundary hydrogen concentration for both grain boundaries. The critical strains at nanovoid nucleation decrease with an increasing grain boundary hydrogen concentration. However, the reduction is greater in the low angle Σ257 [001] tilt grain boundary.
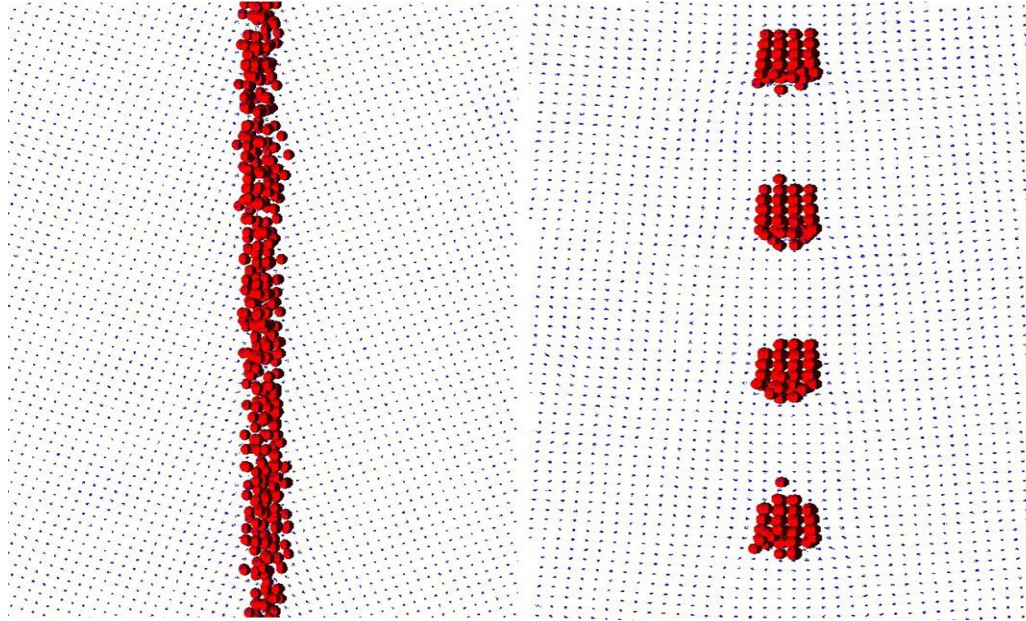
High angle Σ5 grain boundary   Low angle Σ257 grain boundary

Figure 3.16a. MC simulations show that hydrogen is distributed more evenly along the high angle Σ5 grain boundary than that along the low angle Σ257 grain boundary. The red balls represent hydrogen atoms.
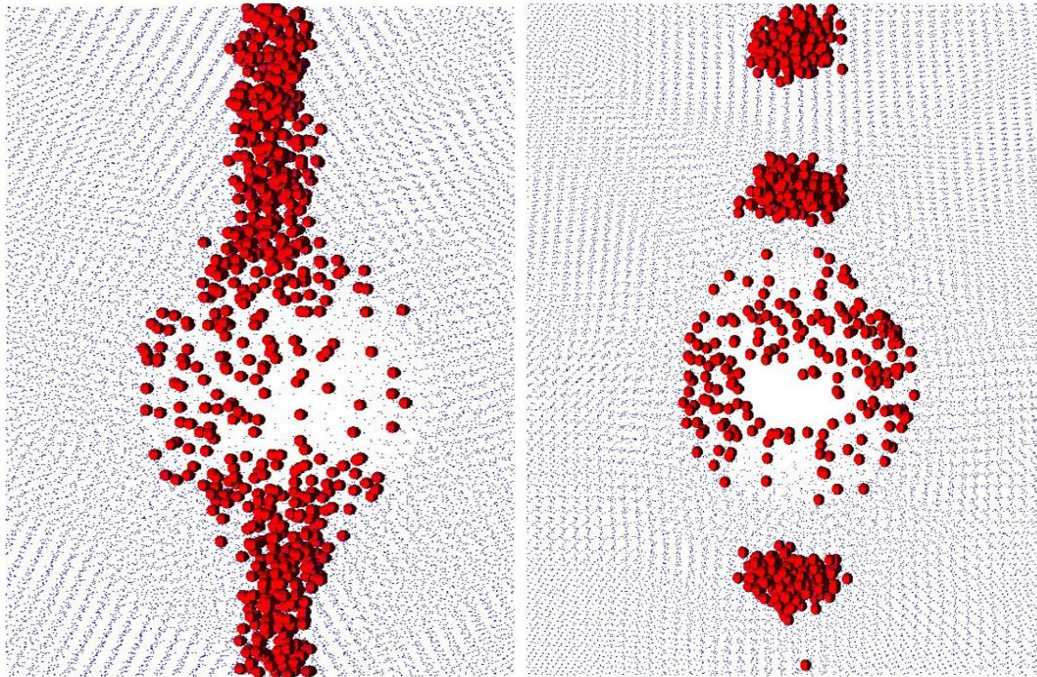
High angle Σ5 grain boundary   Low angle Σ257 grain boundary

Figure 3.16b.   MD simulations show that nanovoid nucleation occurs at both grain boundaries where hydrogen resides. The red balls represent hydrogen atoms.

3.4 Discussion

Continuum void nucleation models are used in finite element codes to predict ductile failures. Horstemeyer and Gokhale [47] developed a model that void nucleation rate $\dot{\eta}$ is a function of fracture toughness K_{IC}, volume fraction of second phase particle f, length scale parameter d, stress state and strain rate $\dot{\varepsilon}$.

$$\dot{\eta} = \frac{\|\dot{\varepsilon}\| d^{1/2}}{K_{IC} f^{1/3}} \eta \left\{ a[\frac{4}{27} - \frac{J_3^2}{J_2^3}] + b \frac{J_3}{J_2^{3/2}} + c \left\| \frac{I}{\sqrt{J_2}} \right\| \right\} \tag{3.3}$$

Stress invariants I_1, J_2, and J_3 are used to distinguish different stress state effects and three material constants a, b and c are used to address the void nucleation contribution from torsional, compressive, and tensile loads. The MD results have shown the relation of the hydrogen concentration to the nucleation of damage. The rest of this section illustrates how MD simulation results are inserted into Equation (3.3) in a hierarchical manner in order to tie the parameters that affect void nucleation with grain boundary hydrogen concentration and local grain geometries. The Horstemeyer and Gokhale model is based on linear fracture criteria for void-crack nucleation that motivated from atomic scale study of Al-Si interfacial debonding [112]. Although the simulation results in this study are based on grain boundaries instead of interfaces between two phase materials, hydrogen trapping, and failure mechanisms at grain boundaries and interfaces are likely to be similar.

The continuum-like averaged stress tensors σ^{ij} from the MD simulations can be used to calculate the stress invariants as the following,

$$I_1 = \sigma^{kk} \tag{3.4}$$

$$J_2 = \frac{1}{2}(\sigma^{ij} - \frac{1}{3}I_1)(\sigma^{ij} - \frac{1}{3}I_1) \tag{3.5}$$

$$J_3 = \frac{1}{2}(\sigma^{ij} - \frac{1}{3}I_1)(\sigma^{ij} - \frac{1}{3}I_1)(\sigma^{ij} - \frac{1}{3}I_1) \tag{3.6}$$

In this study, because periodic boundary conditions were applied, the stress state at nanovoid nucleation was highly triaxial. Table 3.1 shows $\frac{4}{27} - \frac{J_3^2}{J_3}$, $\frac{J_3}{J_2^{3/2}}$ and $\frac{I_1}{\sqrt{J_2}}$ at nanovoid nucleation in the high angle Σ5 grain boundary at different grain boundary hydrogen concentrations. Here, both $\frac{4}{27} - \frac{J_3^2}{J_3}$ and $\frac{J_3}{J_2^{3/2}}$ were negligible, compared to $\frac{I_1}{\sqrt{J_2}}$. A similar trend also applies to both the single crystal and the low angle Σ257 grain boundary indicating the dominance of the stress triaxiality.

Table 3.1. Stress state parameters $\frac{4}{27} - \frac{J_3^2}{J_3}$, $\frac{J_3}{J_2^{3/2}}$ and $\frac{I_1}{\sqrt{J_2}}$ were calculated from MD simulation results at nanovoid nucleation at the Σ5 tilt grain boundary at different grain boundary hydrogen concentrations. The data scatter was caused by the statistical uncertainty related to hydrogen.

Grain boundary H concentration (atomic)	$\frac{4}{27} - \frac{J_3^2}{J_2^{3/2}}$	$\frac{J_3}{J_2^{3/2}}$	$\frac{I_1}{\sqrt{J_2}}$
0.00	0.15	0.02	251.40
0.07	0.08	0.26	149.26
0.12	0.14	0.10	184.37
0.12	0.05	0.32	164.46

Table 3.1 (continued)

0.17	0.15	0.00	247.00
0.18	0.45	0.32	147.00
0.23	0.03	0.34	106.00
0.24	0.02	0.35	83.00
0.24	0.10	0.23	218.27
0.25	0.00	-0.38	110.50
0.26	0.12	0.18	70.63
0.24	0.12	-0.15	103.70
0.29	0.01	-0.37	182.11
0.25	0.02	0.36	73.30
0.24	0.03	0.34	153.90

The triaxiality factor, c, in Equation (3.3) in tension is dominant and has been shown to relate to tensile stress states and damage nucleation by Dighe and coworkers [55].

The Horstemeyer-Gokhale model [47] can then be simplified to the following,

$$\dot{\eta} = \frac{d^{1/2}}{K_{IC} f^{1/3}} c \|\dot{\varepsilon}\| \eta \left\| \frac{I_1}{\sqrt{J_2}} \right\|$$

(3.7)

With the inclusion of hydrogen, the equation may be rewritten as

$$\dot{\eta}_H = \frac{d^{1/2}}{K_{IC} f^{1/3}} c_H \|\dot{\varepsilon}\|_H \eta_H \left\| \frac{I_1}{\sqrt{J_2}} \right\|_H$$

(3.8)

where $\dot{\eta}_H$ is the void nucleation rate of hydrogen-charged specimens, η_H is the void number density of hydrogen-charged specimens, $\|\dot{\varepsilon}\|_H$ is the imposed strain rate in the

hydrogen-charged specimen, and $\left\|\dfrac{I_1}{\sqrt{J_2}}\right\|_H$ is calculated from the continuum-like averaged

stress tensors from the MD simulations of hydrogen-charged specimens. Rearranging

Equations (3.7) and (3.8), get

$$\frac{c_H}{c} = \frac{\dot{\eta}_H}{\dot{\eta}}\,\frac{\eta}{\eta_H}\,\frac{\|\dot{\varepsilon}\|}{\|\dot{\varepsilon}\|_H}\,\frac{\left\|\dfrac{I_1}{\sqrt{J_2}}\right\|}{\left\|\dfrac{I_1}{\sqrt{J_2}}\right\|_H} \tag{3.9}$$

We define the term $\dfrac{c_H}{c}$ as a normalized void nucleation coefficient, since it

shows the effects of hydrogen on the void nucleation.

MD simulation results with and without hydrogen for grain boundary specimens

were inserted into Equation (3.9). The imposed strain rates were the same for all the

cases. The void number densities were the same since only one void was nucleated and

specimen sizes were the same for all the specimens. The void nucleation rate was

calculated by using one void divided by the time for the nanovoid nucleation to occur.

The stress invariants were calculated from the continuum-like stress tensor at nanovoid

nucleation.

Figure 3.17 shows the normalized void nucleation coefficient versus grain

boundary hydrogen concentration in the low angle Σ257 [001] tilt grain boundary and the

high angle Σ5 [001] tilt grain boundary. The normalized void nucleation coefficient

increased with increasing grain boundary hydrogen concentration and followed a similar

exponential trend in both grain boundaries. This indicates that as the grain boundary

hydrogen concentration increases, the nucleation rate for damage will increase. However, the normalized void nucleation coefficient increased more in the low angle grain boundary Σ257 than in the high angle grain boundary Σ5. The possible reason may lie in the heterogeneity of the local hydrogen distribution in Σ257 versus relatively homogenous distribution in Σ5 at and near the grain boundary plane, as shown in Figure 3.16a.

Based on Figure 3.17, the normalized void nucleation coefficient can be written as

$$\frac{c_H}{c} = e^{mH_B} \tag{3.10}$$

H_B is the grain boundary hydrogen concentration, and m is a material parameter that accounts for different local structures such as different grain boundaries. According to Figure 3.17, for the high angle Σ5 grain boundary, m is 3.27; for the low angle Σ257 grain boundary, m is 6.47. Grain boundary hydrogen concentration H_B can be calculated based on Equation (3.2). Trap binding energy W_B can be evaluated experimentally. The bulk hydrogen H_L can be calculated based on hydrogen pressure by Sievert's law [113].

Equation (3.8) provides a form that ties stress triaxiality-driven void nucleation with grain boundary hydrogen concentrations and local grain geometries at the nanoscale.
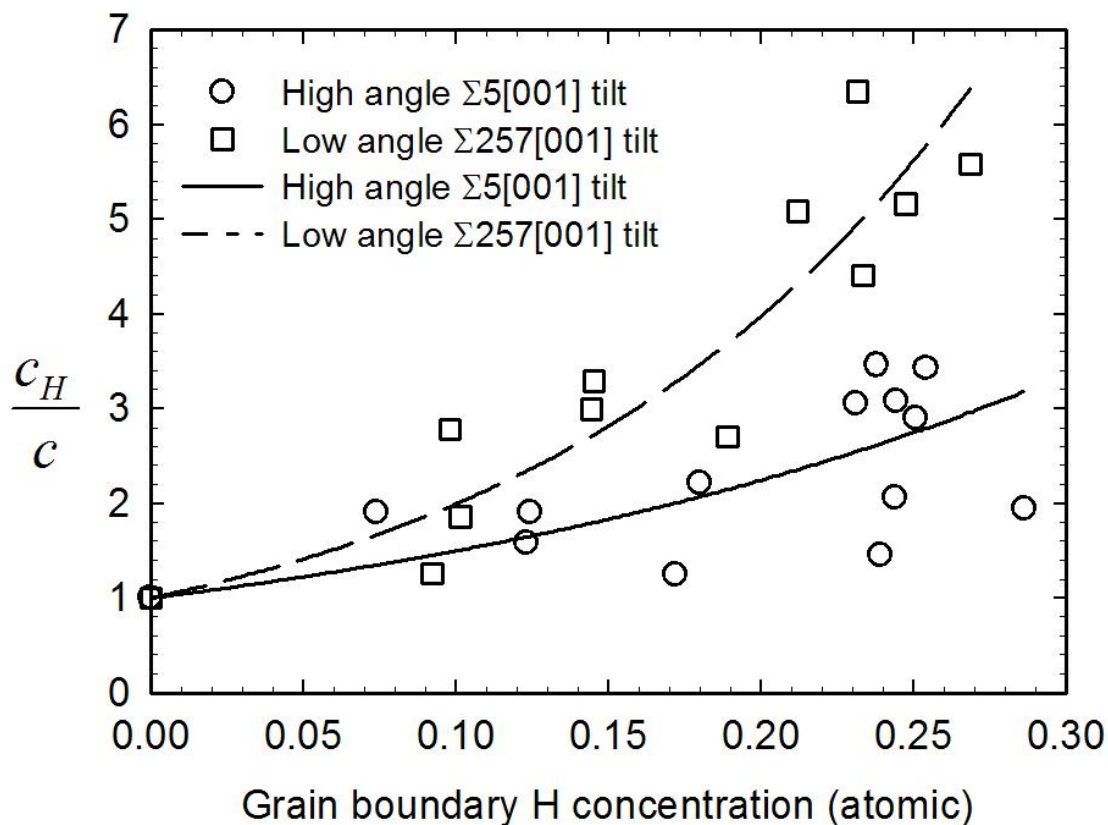
Figure 3.17. Normalized void nucleation coefficient versus grain boundary hydrogen concentration. The normalized void nucleation coefficient increased exponentially with increasing grain boundary hydrogen concentration in both the high angle Σ5 and the low angle Σ257 tilt grain boundaries, and it increased more rapidly in the low angle Σ257 tilt grain boundary than the high angle Σ5 tilt grain boundary.

3.5   Summary of Chapter 3

Several conclusions can be drawn from the MC and MD simulations that were performed to study hydrogen-enhanced nanovoid nucleation in nickel grain boundaries.

- When hydrogen was introduced into unstressed specimens, it was distributed homogenously in the single crystal specimen, but accumulated at grain boundaries in the bi-crystal specimens. At equilibrium, the grain boundary hydrogen concentrations were much higher than bulk hydrogen concentration (single crystal hydrogen concentration). However, there was very small difference in grain boundary hydrogen concentration in a low angle $\Sigma 257$ [001] and a high angle $\Sigma 5$ [001] tilt grain boundary. The effective trap binding energy decreased with increased bulk hydrogen concentration.

- The critical stress and strain at nanovoid nucleation changed little with increasing hydrogen concentration in a single crystal. This agrees well with experimental data trends that show the ductility of a single crystal is not reduced as much as polycrystals [3-4].

- In bi-crystal specimens, the stress-strain responses and dislocation evolution show that the work hardening rate and dislocation evolution prior to nanovoid nucleation was not changed by hydrogen. The critical stress at nanovoid nucleation decreased with increasing grain boundary hydrogen concentration indicating that hydrogen may have reduced the cohesive force between atoms at the grain boundary. Furthermore, the elongation to failure decreased with increasing grain boundary hydrogen concentration. This most likely indicates a hydrogen-induced decohesion mechanism [13]. Several researchers [114-116] also observed similar trends in their experiments in pure nickel.

- The effects of hydrogen on nanovoid nucleation were slightly more pronounced in the low angle $\Sigma257$ [001] tilt gain boundary than the high angle $\Sigma5$ [001] tilt grain boundary at same grain boundary hydrogen concentrations, possibly caused by different local hydrogen distributions at the grain boundaries.

- MD results were inserted into the Horstemeyer and Gokhale continuum void nucleation model [47] and a relationship between stress triaxiality-driven void nucleation and grain boundary hydrogen concentration was extracted, which was used in the development of a modified continuum void nucleation model in the later chapter.

CHAPTER IV

HYDROGEN EFFECTS ON NANOVOID NUCLEATION IN FCC SINGLE CRYSTALS

4.1 Introduction

Hydrogen solutes cause a reduction on macroscopic fracture stresses and strains in ductile materials [2-8] and that the effects are even more detrimental when dynamically-charged [36]. Void nucleation not only occurs at the second phase particles [117-118] and grain boundaries [119], but is also observed inside grains and in single crystals [23]. A number of experiments show that hydrogen promotes void nucleation inside grains and single crystals. Birnbaum and co-workers [16, 120-121] performed straining experiments in a hydrogen environment on nickel and aluminum in-situ, and observed that hydrogen promoted transgranular cracks by either affecting the emission of dislocations from the crack tip, or by affecting void nucleation and growth ahead of the crack tip. Chen and his co-workers [122] also observed that hydrogen promoted nanovoid nucleation in thin crystals of a 310 stainless steel. Jiang and co-workers [40] suggested that hydrogen encouraged void nucleation at either the intersection of active slip bands or at the dislocation cell walls by affecting local dislocation interactions. The experiments by Birnbaum and Chen were performed in a hydrogen environment, and hydrogen was continuously charged into the specimen while loads were being applied on the specimen. We consider this case as a dynamically-charged condition. Jiang's specimens were

63

charged with hydrogen before loads were applied. We consider this case as a precharged condition. We consider this case as a precharged condition.

Hydrogen effects on void nucleation at the atomistic scale need to be studied in order to understand the microscale and macroscale responses. Molecular Dynamics (MD) simulations have been performed to study the effects of hydrogen on single crystal nickel [123-124]. In those simulations, hydrogen was randomly placed in the lattice before MD simulations were performed, and the effects due to hydrogen transport by stress gradients and by dislocation trapping was not addressed, because current MD simulations alone have limitations in addressing hydrogen diffusion.

In this chapter, the MC and MD simulations employing EAM potential [75-76] were performed to study hydrogen effects on dislocation nucleation and nanovoid nucleation in hydrogen-precharged and hydrogen dynamically-charged conditions in nickel single crystals. In the precharged condition, hydrogen atoms were introduced in the specimen before any stress and strain was applied. Hydrogen diffusion due to stress gradient and defects caused by plastic deformation was not addressed. In the dynamically-charged condition, hydrogen atoms were introduced in the specimen by using a novel MD-MC process at different strain levels incrementally. By doing so, hydrogen transport by stress gradients and by dislocation trapping can be captured. The purpose of this work was to study how hydrogen affects nanovoid nucleation and the underlying mechanisms differently in various charging conditions. The MD simulation results were also inserted into Horstemeyer and Gokhale continuum void nucleation model [47] in order to extract the relationship between nanovoid nucleation and hydrogen

transport by stress gradient and dislocation trapping. The findings can be passed to the higher length scale and aid in the continuum model development.

4.2   Model Parameters and Computational Setup

The single crystal nickel cubic-shaped specimens are 21 nm in the [100] direction, 21 nm in the [010] direction and 2.8 nm in the [001] direction. A total of 115,000 nickel atoms were created. Periodic boundaries were applied in all direction. Figure 4.1 shows the schematic drawing of the model.
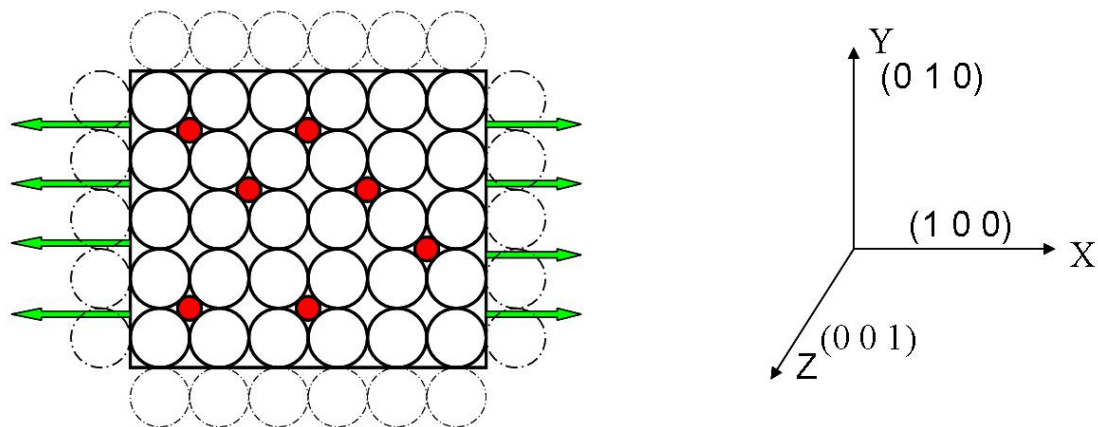
Figure 4.1.   The schematic of the single crystal model show nickel atoms in big black circles, hydrogen atoms in small red circles. The grey circles represent the image atoms. The arrows indicate the loading direction. The orientation of the crystal is shown on the right.

For a hydrogen-precharged system, the system was brought to thermal equilibrium at 300K at pressure 0 bar. MC simulations were then performed to introduce hydrogen atoms in the specimen by applying a chemical potential. Because no stresses or displacements were applied on the specimen, the hydrogen concentration introduced was

an unstressed lattice concentration [125] or define as a precharged concentration or bulk concentration. The specimen was subjected to a strain rate of 5×10^8/sec in the (100) direction until the specimen failed accompanied by nanovoid nucleation.

For a hydrogen dynamically-charged condition, a novel coupled MD-MC process was used. Once the unstressed lattice concentration (bulk concentration) was created, the specimen was subjected to a strain rate of 5×10^8/sec in [100] direction to 8% of engineering strain in the [100] direction. MC simulations were again run on this strained specimen with the same chemical potential applied. The specimen was then pulled to 12% strain in the [100] direction. This procedure was repeated several times with 4% strain increments until the specimen failed mainly due to nanovoid nucleation and rapid void growth immediately after.

Figure 4.2 shows the MC and MD simulations performed for both H-precharged and H-dynamically-charged cases.

The boundary conditions in MD simulations were based on the Parrinello-Rahman method [126] in which the three Cartesian coordinates of the atoms were rescaled to the unit box. When calculating the velocity and new positions of the atoms and also the atomic forces, the unit box was multiplied by a diagonal scaling matrix. The positions of the atoms are given by the following,

$$X^i = LS^i, \tag{4.1}$$

where S_i is the scaled Cartesian coordinates of atom i, and L is a matrix with the simulation box size length as diagonal terms. They are updated at each time step as the strain rate is applied,

$$L' = L(I + t\bar{\dot{\varepsilon}}), \tag{4.2}$$

$$X^{i'} = L'(I + t\bar{\dot{\varepsilon}})S^i, \tag{4.3}$$

where $\bar{\dot{\varepsilon}}$ is the applied strain rate matrix. In our calculations, the only nonzero term of the strain rate matrix was the first diagonal term. As such, the bulk strain was uniaxial.

Because periodic conditions were applied in all three directions, even if the specimens were only subjected to strain rates in the (100) direction, the calculated bulk stress tensor included all the components. The hydrostatic stresses were quantified at different hydrogen concentrations. The bulk mean (hydrostatic) stresses were calculated as the following:

$$\sigma_m = I_1 = \frac{1}{3}\sigma^{kk} \tag{4.4}$$

Correspondingly, the bulk von Mises stress was calculated as:

$$\sigma_{von} = \sqrt{J_2} = \sqrt{\frac{1}{2}(\sigma^{ij} - \sigma_m\delta^{ij})(\sigma^{ij} - \sigma_m\delta^{ij})} \tag{4.5}$$

where J_2 is the second invariant of deviatoric stress.

The third invariant of deviatoric stress was calculated as:

$$J_3 = \frac{1}{3}(\sigma^{ij} - \sigma_m\delta^{ij})(\sigma^{ij} - \sigma_m\delta^{ij})(\sigma^{ij} - \sigma_m\delta^{ij}) \tag{4.6}$$

The stress triaxiality was calculated as:

$$\chi = \frac{\sigma_m}{\sigma_{von}} \tag{4.7}$$

The applied strain at each time step was calculated as the following:

$$\varepsilon = t\dot{\varepsilon} \tag{4.8}$$
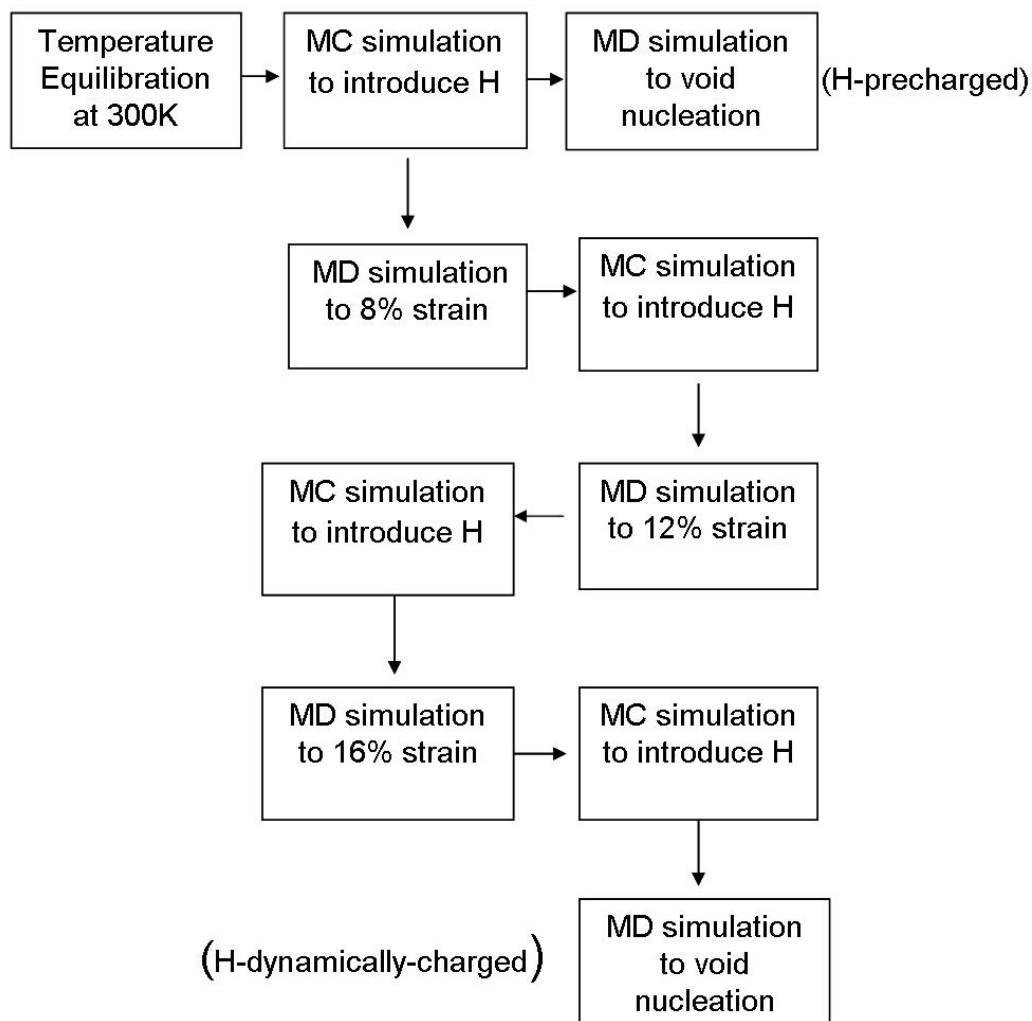
Figure 4.2.   The diagram shows MC and MD simulations performed for H-precharged case and H-dynamically-charged case. In H-precharged case, MD simulation and MC simulations were performed only once; in H-dynamically-charged case, MC and MD simulations are performed alternatively to couple mechanical straining and hydrogen charging.

4.3   Results

4.3.1   Hydrogen Concentrations

MC simulation results of hydrogen introduced in the precharged and dynamically-charged cases are discussed in this section. The relationship between hydrogen diffusion and chemical potentials were described earlier in chapter three. Figure 4.3(a) shows the hydrogen concentration in an unstressed lattice corresponding to the precharged case at different chemical potentials. Note that the definition of a precharged case here is different from the precharged cases in many experiments. In this case, because very high strain rates were used in MD simulations, and because hydrogen in a single crystal nickel can only diffuse on the order of 10^{-4}nm/ps at 300K, the long-range diffusion of hydrogen in a specimen was minimal. Some experiments [127] have shown that after the specimen has been precharged, hydrogen will diffuse and redistribute in the specimen during mechanical straining, given a low applied strain rate and sufficient time. Figure 4.3(b) shows that the hydrogen concentration in the specimen increased with increasing chemical potential and applied strain in the dynamically-charged case.   After hydrogen was introduced in the unstressed lattices, the specimen was strained to 8% strain in the (100) direction. Figure 4.6 shows that the bulk tensile hydrostatic stress was about 10GPa at this strain level, which was extremely high. The tensile hydrostatic stresses lowered the chemical potential of the hydrogen solutes [125] and caused a higher chemical potential gradient that drove more hydrogen into the specimen. At 12% and 16% strain, the tensile hydrostatic stresses were even higher. As a result, more hydrogen atoms were introduced in the specimen. Figures 4.3(a) and 4.3(b) show that the hydrogen concentration in the

dynamically-charged specimen was much higher than in the precharged specimen. Based on the applied chemical potentials, bulk hydrogen concentrations can be determined, corresponding to lattice hydrogen concentration in an unstressed lattice, which was also defined in the grain boundary study in the previous chapter. In the precharged case, the hydrogen concentration in the specimen was the same as the bulk hydrogen concentration, because no defects and stress gradient were present. In the dynamically-charged case, the applied strain induced dislocations and high hydrostatic stresses, which caused much higher hydrogen concentrations in the specimen than the bulk hydrogen concentration. Figure 4.4 shows the final hydrogen concentrations in the specimen versus bulk hydrogen concentration in the dynamically-charged case. Note the hydrogen concentrations did not saturate and the system did not reach equilibrium state, thus a transit state was observed. Experimental observations [128-129] also indicate that hydrogen tends to diffuse to the region with high tensile hydrostatic stresses, such as ahead of a crack tip.
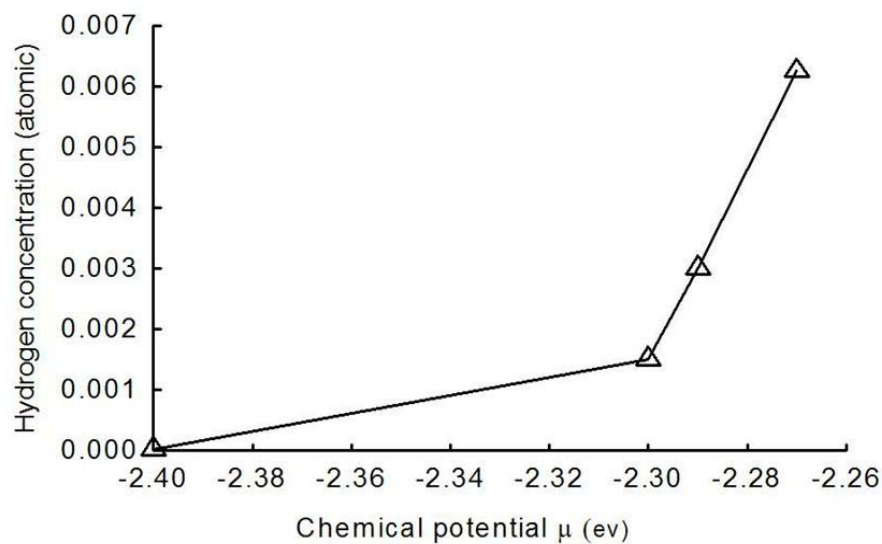
(a)
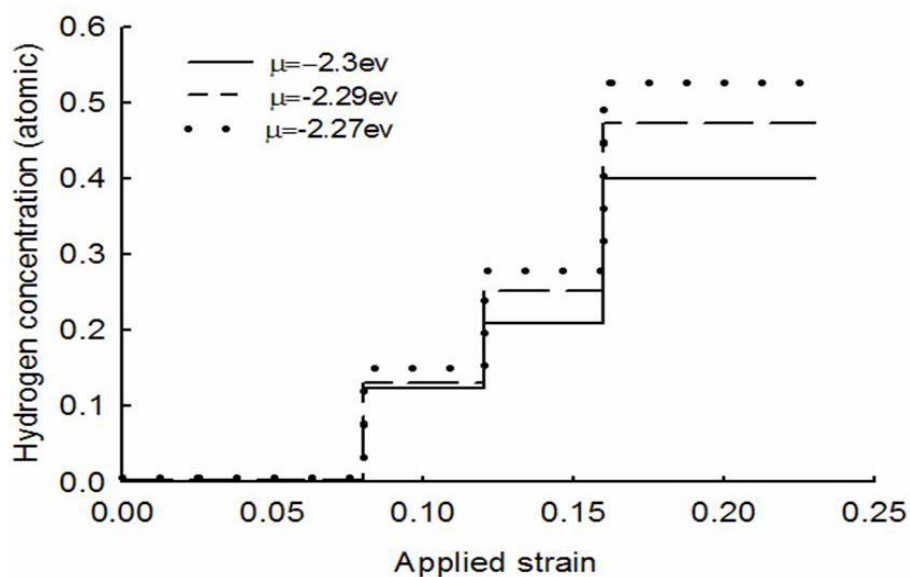
(b)

Figure 4.3.   MC simulation results show that the (a) hydrogen concentration increased with increasing chemical potential in the precharged case, and not only increased with increasing chemical potential, but (b) also with increasing strain in the dynamically-charged case.
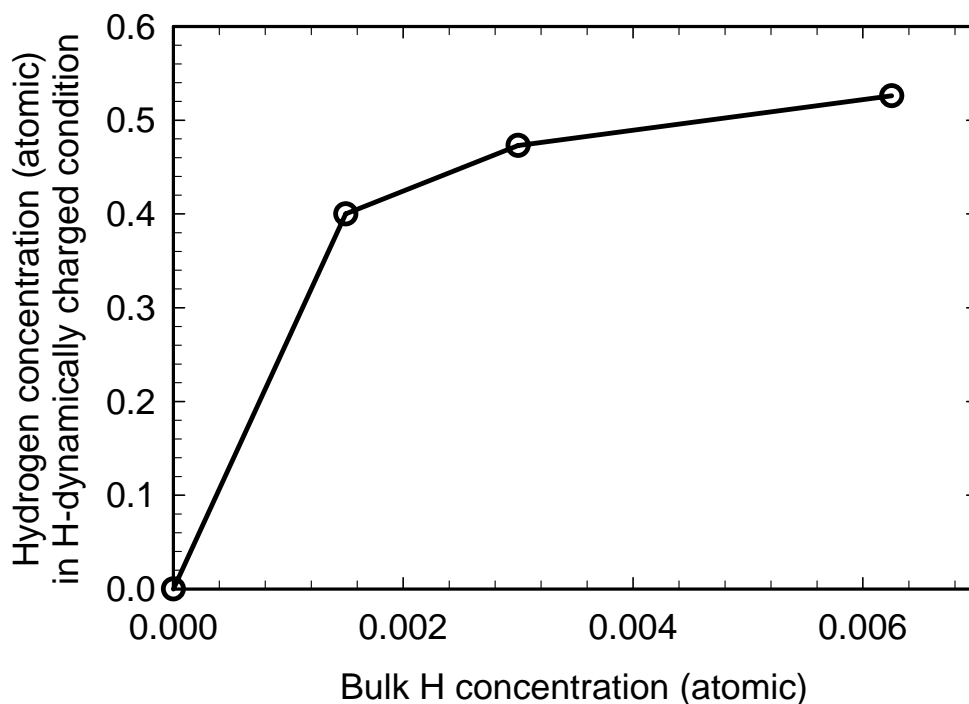
Figure 4.4.   MC simulation results show the final hydrogen concentration in the specimen versus the bulk H concentration in the dynamically charged case. High hydrostatic stress and plasticity-induced dislocations in the specimen caused the much higher hydrogen concentrations, compared to the bulk H concentrations.

4.3.2   Hydrogen Effects on Nanovoid Nucleation

We used the MD simulation results from an uncharged specimen at 300K to illustrate the relationship between the loading mode and related dislocation activity and nanovoid nucleation. Figure 4.5 shows the hydrostatic stress, von Mises stress, and stress triaxiality versus applied strain when the specimen was subjected to a strain rate of 5×10^8/sec. Figure 4.5 also shows the CNA snap shots at different strain levels.

Initially, the stress state was predominantly uniaxial, which was marked by an increased von Mises stress and low stress triaxiality. The specimen deformed elastically until dislocations started to nucleate at 11% strain and the stress reached a maximum. This point is defined as yield point, which is the same as macro-yield point defined by Horstemeyer et al. [91]. CNA snap shots show arrays of HCP atoms in a FCC environment indicating that stacking faults formed by partial dislocations. The stress state then became more triaxial, as characterized by a decreased von Mises stress and an increased hydrostatic stress. When the von Mises stress leveled off, stacking faults and dislocation networks overtook the entire specimen. The hydrostatic stress then increased dramatically and the stress triaxiality remained high. When the hydrostatic stress reached a maximum, (at a critical level of the hydrostatic stress and stress triaxiality, a nanovoid was nucleated, drastically lowering both of these quantities).

Figure 4.5 show that nanovoid nucleation occurred at the peak hydrostatic stresses, and was even more sensitive to the stress triaxiality. The local hydrostatic stress is closely tied to hydrogen absorption. Figure 4.6 shows the hydrostatic stress versus applied strain in all three conditions. The stress-strain curve in the precharged case followed the same trend as the hydrogen-free case until nanovoid nucleation occurred at about 7% lower stress than the hydrogen-free case. The hydrostatic stress in the hydrogen dynamically-charged case followed the same trend as the other two cases until 8% strain was reached. An additional 11% of hydrogen atoms were introduced in the specimen due to the tensile hydrostatic stress in the specimen. The volume expansion of hydrogen atoms may have lowered the bulk tensile hydrostatic stress and caused a hydrostatic

stress drop at 8% strain in the dynamically-charged case. The bulk hydrostatic stress increased as the strain increased until 12% strain, at which an additional 12% of hydrogen atoms were introduced in the specimen, which caused another drop in the bulk hydrostatic stress. The same trend also occurred at 16% strain. The specimen was strained further until the hydrostatic stress reached the peak and nanovoid nucleation occurred. The resulting peak hydrostatic stress at nanovoid nucleation in the dynamically-charged case was 42% lower than in the hydrogen-free case. The resulting critical strain at nanovoid nucleation was only 6% lower than in the hydrogen-free case. Due to a limitation on computation time, the hydrogen was only charged into specimens three times in the dynamically-charged condition in our simulations. To simulate a true dynamically-charged condition, hydrogen should be continuously charged as the deformation occurs; however, the qualitative trend observed here would not change even if the time step were lowered for the charging. Kimura and Matsui [130] observed a stress drop when hydrogen was charged after pulling the specimen to 3% strain, which was similar to what our simulation results showed. Shin and workers [131] also observed the similar zigzag stress-strain response in an intermittent cathodically-charged single crystal iron specimen as shown in Figure 4.7. Even though our results are for single crystal nickel, the effects of hydrogen on the stress-strain response appeared to be similar to the experimental results of single crystal iron, given the similar charging condition. Figure 4.8 shows that the von Mises stress (the second invariant of deviatoric stress J_2) changed little in the hydrogen-precharged case; however, it increased at the macro-yield point in the dynamically-charged case. Figure 4.9 shows the third invariants of deviatoric

stress J_3) also exhibited similar trends to the second invariants. This is reasonable since both J_2 and J_3 are related to the shear stress. Figures 4.8 and 4.9 indicate that hydrogen caused a higher yield stress in the dynamically-charged case. Figures 4.6, 4.7 and 4.8 show that hydrogen caused little change in the bulk stress in the precharged case, however, affected predominantly the hydrostatic component of bulk stress in the dynamically-charged case.

We define the hydrostatic stress at the nanovoid nucleation as the *hydrostatic fracture stress*, and the applied strain at the nanovoid nucleation as the *fracture strain*. Figure 4.10 shows the hydrostatic fracture stress versus bulk hydrogen concentration for hydrogen-precharged and hydrogen dynamically-charged cases. Figure 4.11 shows the fracture strain versus bulk hydrogen for hydrogen-precharged and hydrogen dynamically-charged cases. To address the statistical issue of hydrogen occupation in the specimen, we also ran several duplicated simulations in the hydrogen-precharged cases. We also ran simulations subjected to a strain rate of 5×10^7/sec in the precharged case besides a strain rate of 5×10^8/sec. Figure 4.10 shows that the hydrostatic fracture stress decreased less than 7% for the precharged case, but decreases more than 40% in the dynamically-charged case. Figure 4.10 shows that subjecting the specimen to a lower strain rate did not change the trends in the precharged case. Figure 4.10 also shows some statistical scatter due to the positioning of hydrogen interstitials in the precharged case. Figure 4.11 shows that hydrogen caused a small reduction in fracture strain for the hydrogen-precharged case and little change for the hydrogen dynamically-charged cases.

Figure 4.12 shows that the fracture hydrostatic stress decreased continuously with hydrogen concentration in the specimen in the dynamically-charged condition, which indicated that the fracture stress strongly depended on the amount of hydrogen in the system in the dynamically-charged case. Figure 4.13 shows that the fracture strain changed little with increasing hydrogen concentration in the dynamically-charged condition.
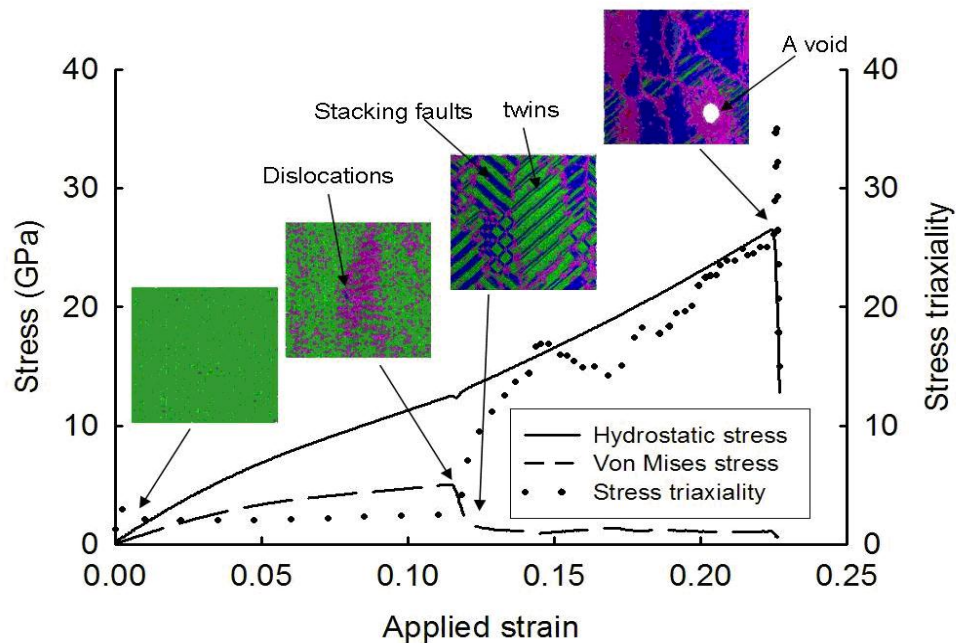
Figure 4.5.   Molecular Dynamics (MD) simulations show that the von Mises stress increased to the yield point marked by dislocation initiation, then dropped sharply as dislocations proliferated through the specimen, and finally saturated upon further deformation. The hydrostatic stress also increased before dislocation initiation, and then increased more steeply until a void nucleated. The stress triaxiality was small until dislocation initiation and then increased dramatically until a nanovoid nucleated. In CNA snapshots, the color green is designated as a local FCC structure, the color blue represents the local HCP structure, and the color pink is an unknown lattice structure. Each snap shot includes the total simulation domain of Nickel crystals.
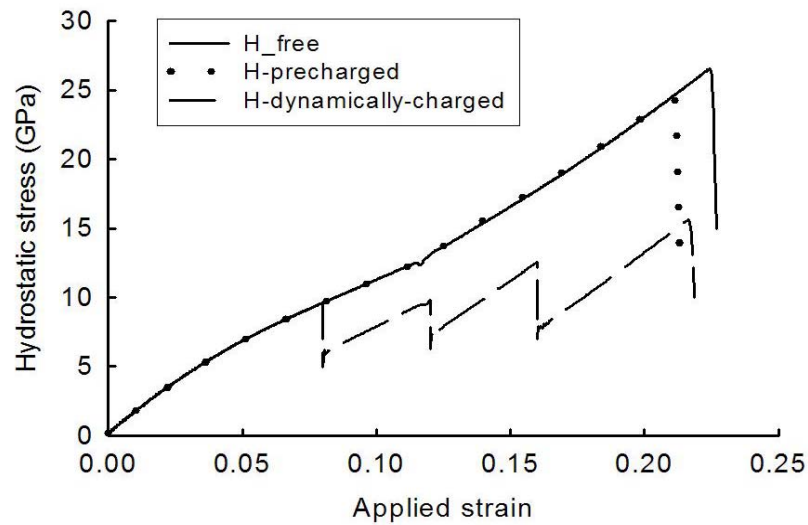
Figure 4.6.   MD simulation results show that the bulk hydrostatic stress increased until a nanovoid nucleated in the hydrogen-free and hydrogen-precharged cases. For the hydrogen dynamically-charged case, the tensile hydrostatic stress increased incrementally until a nanovoid nucleated. The peak hydrostatic stress is about 40% lower in the hydrogen dynamically-charged case than the hydrogen-free case.
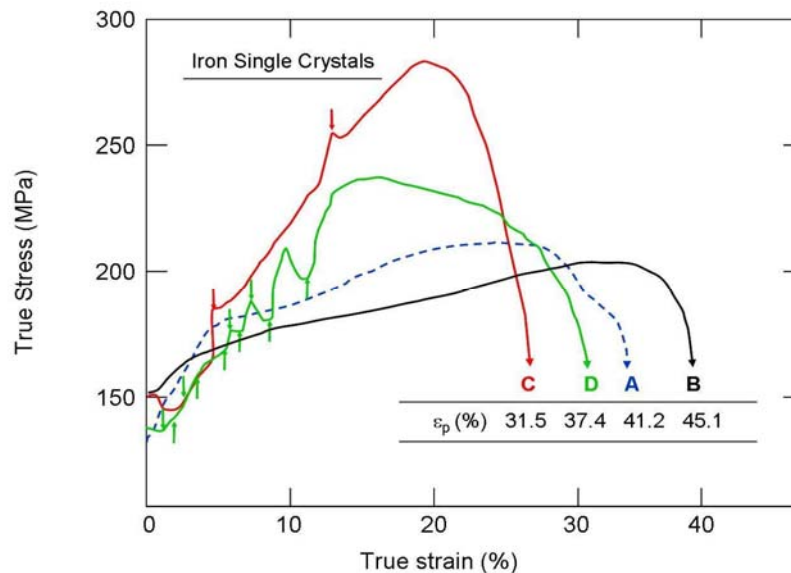
Figure 4.7.   Experimental results in single crystal iron shows the there is a stress drop at each increment when hydrogen was charged in curve D [131].
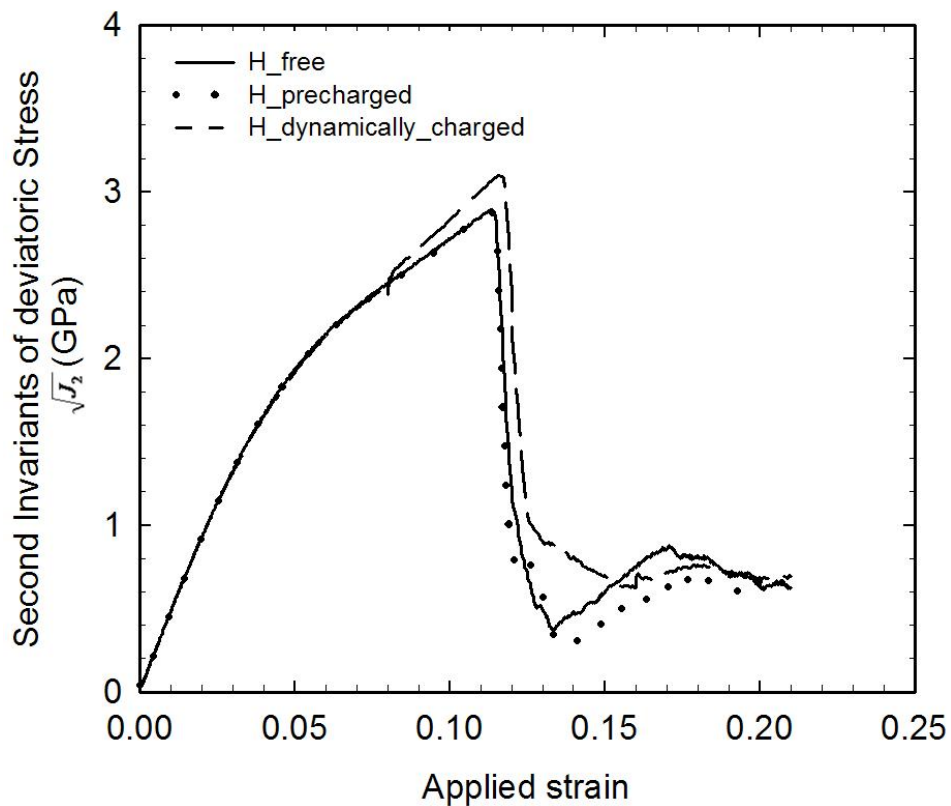
Figure 4.8.   Second invariants of deviatoric stress $\sqrt{J_2}$ versus applied strain in H-free, H-precharged and H-dynamically-charged conditions. Hydrogen did not change the yield stress in the precharged condition but caused a small increase in yield stress in the dynamically-charged condition.
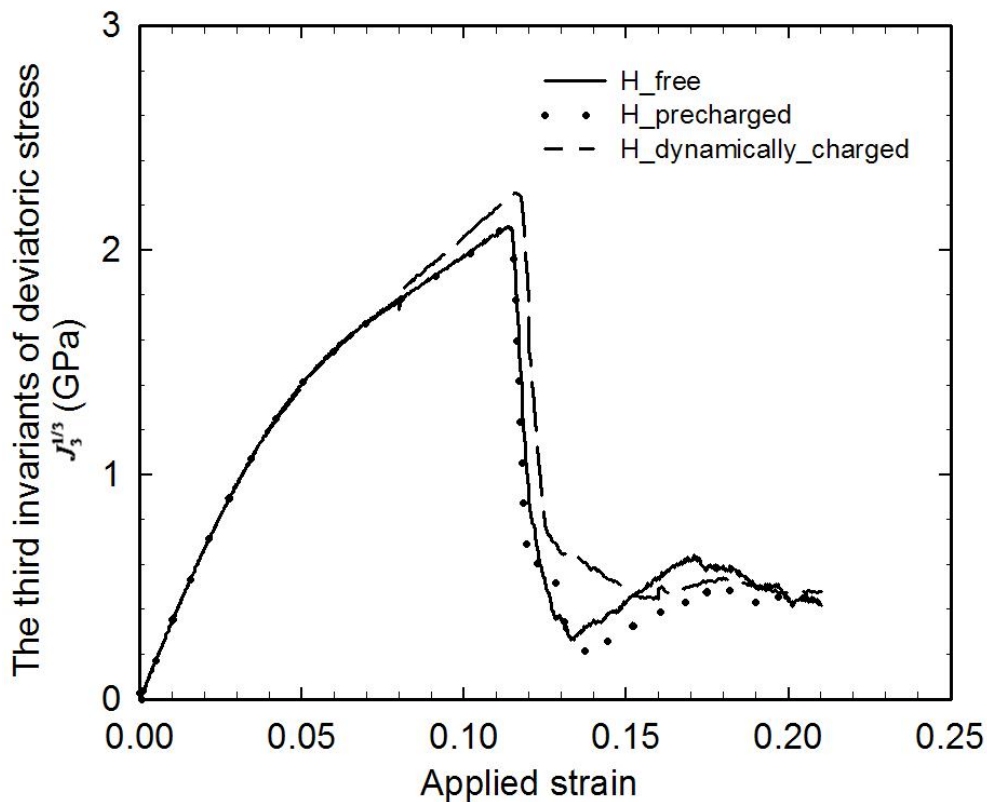
Figure 4.9.   The third invariant of deviatoric stress $J_3^{1/3}$ versus applied stress in H-free, H-precharged and H-dynamically-charged conditions. Hydrogen caused little change in the precharged condition, but caused a higher peak value in the dynamically-charged case.   The peak value corresponds to the yield point.
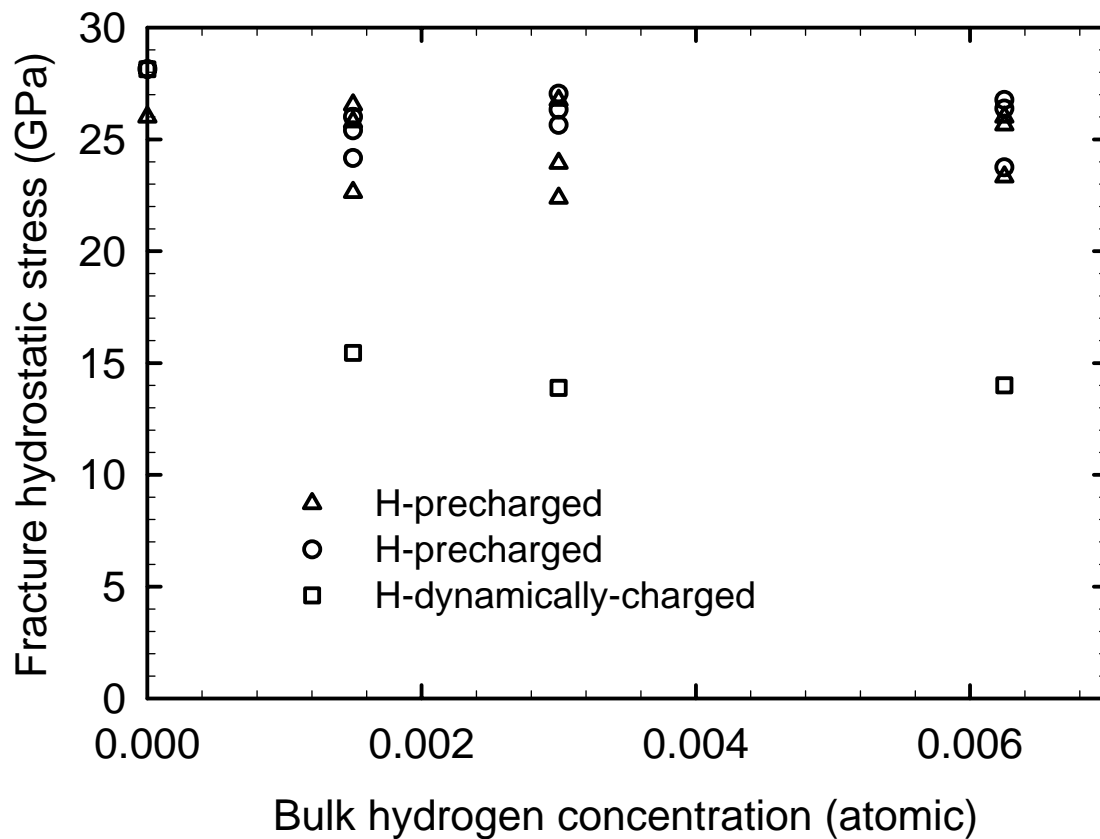
Figure 4.10.   MD simulation results show that the reduction in hydrostatic fracture
stress was only around 7% in the precharged case, and subjection to lower
strain rate did not change this trend. The reduction in hydrostatic fracture
stress was over 40% lower in the dynamically-charged case.
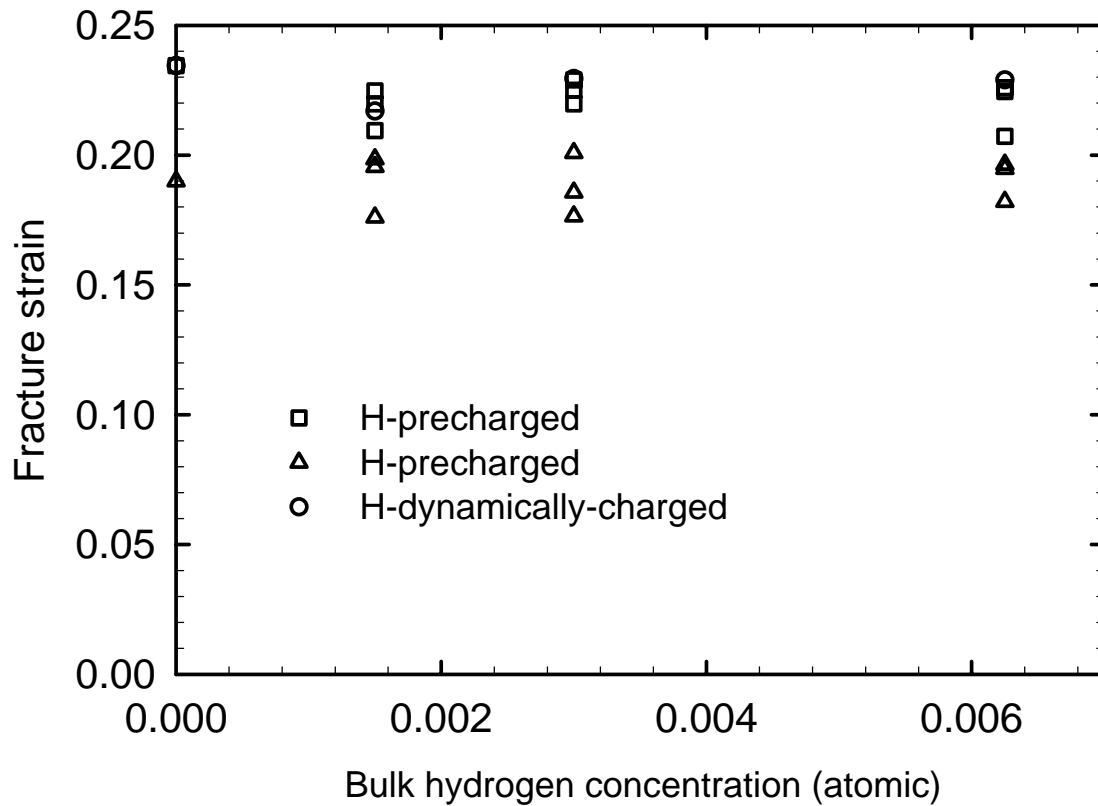
Figure 4.11.   MD simulation results show that hydrogen caused slight reductions in fracture strains for hydrogen-precharged cases and nearly no change in fracture strains for hydrogen dynamically-charged cases. Subjecting to lower strain rate did not change the trend in the precharged case.
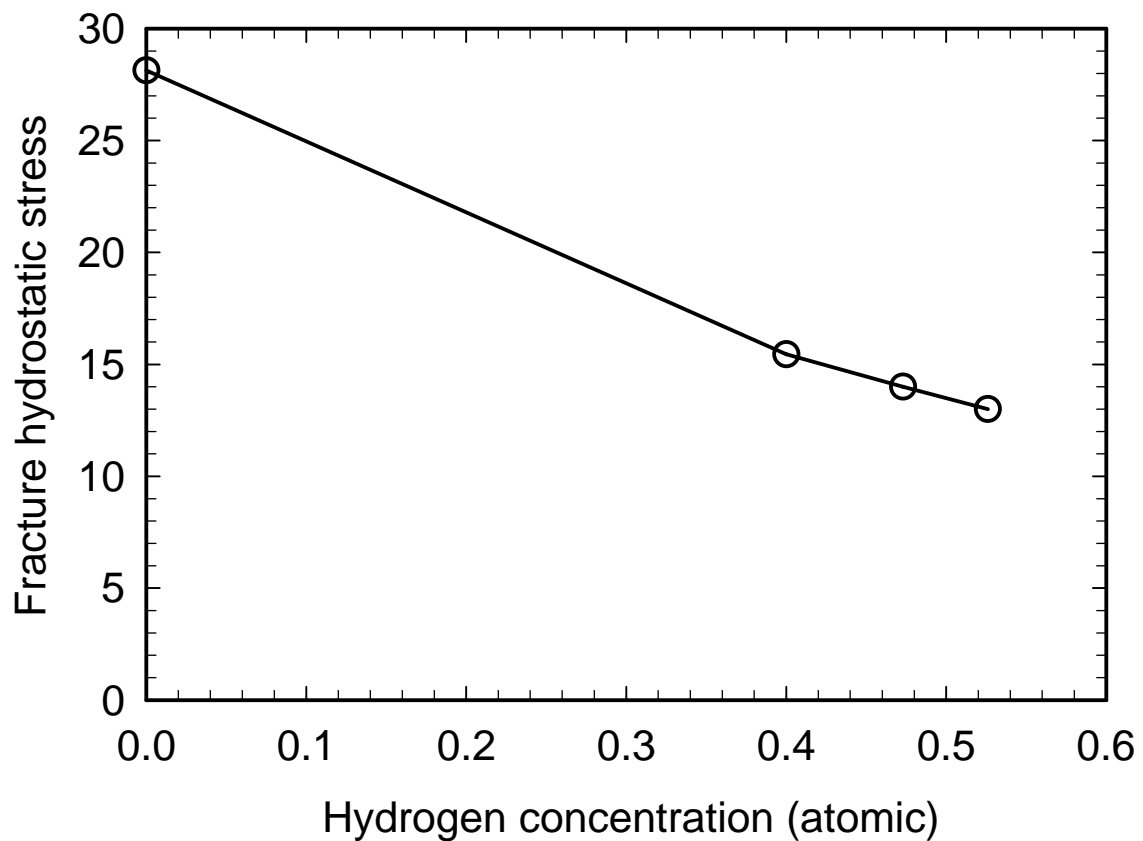
Figure 4.12.   MD simulation results show that fracture hydrostatic stress decreased continuously with increased hydrogen concentration in H-dynamically-charged condition.
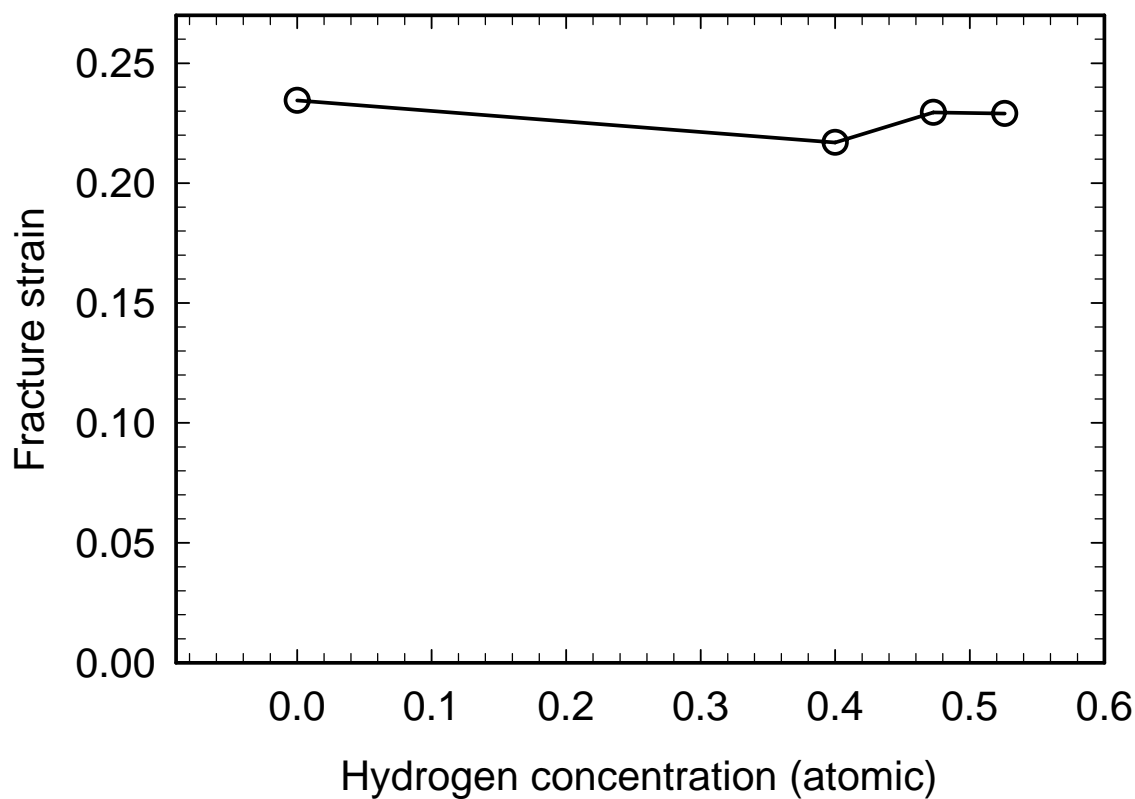
Figure 4.13.   MD simulation results show that fracture strain changed little with increased hydrogen condition in H-dynamically-charged case.

4.3.3   *Dislocation structures*

The MD simulation results show that hydrogen affects the stress-strain responses and nanovoid nucleation. To gain insight and understanding of the underlying mechanisms, Figure 4.14 shows the CNA snapshots of hydrogen-free, hydrogen-precharged, and hydrogen dynamically-charged cases at 0%, 12%, 16%, 20% strains, and the point of nanovoid nucleation. Here, ε denotes the applied strain, and μ denotes the applied chemical potential. The CNA snap shots at 12% strain show that stacking faults

and dislocation networks were observed in all three cases. At 16% and 20% strain, the dislocation structures were similar in the hydrogen-free and hydrogen precharged case, but they were markedly different in the dynamically-charged case. As the deformation increased in hydrogen-free and hydrogen-precharged cases, stacking faults and dislocations continued to form, piling up next to each other to form some HCP-like cells. Eventually, a nanovoid nucleated at an intersection of cell walls. In the dynamically-charged case, more stacking faults and dislocations formed with increasing deformation, but no HCP-like substructure was formed. Eventually a nanovoid developed at an intersection of two stacking faults.

Figure 4.15 shows the percentage of atoms in a local HCP structure versus applied strain illustrating a lower percentage of HCP atoms in the dynamically-charged case than in both hydrogen-free and precharged cases. The FCC structure changed into an HCP structure as partial dislocations nucleated. A lower percentage of HCP atoms indicate a lower dislocation density. Since a lower dislocation density produces a lower strain hardening rate [132] in macroscale experiments, a corollary may be similar in these nanoscale numerical experiments: the dynamically-charged case leads to less dislocations hence leading to a lower work hardening rate.

To further understand the dislocation structures in Figure 4.14. Nickel FCC single crystal and nickel HCP single crystal specimens were modeled. Both specimens were charged with different hydrogen concentrations: 0% (atomic), 5% (atomic), 12.5% (atomic) and 20.5% (atomic). Hydrostatic tension loads were applied on both specimens at different hydrogen concentrations. The energy differences were calculated by

subtracting the energy at each configuration to the initial energy of nickel in its natural state FCC at 300K. The configurations with smaller energy differences are more stable than the configurations with higher energy differences. Figure 4.16 was plotted to show the energy difference versus applied hydrostatic tension of FCC Ni and HCP Ni with different hydrogen concentrations. Figure 4.16a shows that the averaged energy per atom of Ni in the FCC crystal structure was lower than in the HCP crystal structure until the applied hydrostatic tension exceeded 20GPa in the hydrogen-free condition, indicating the specimen is in a FCC structure if the applied hydrostatic tension is under 20 GPa, and is in a mostly HCP structure if the applied hydrostatic tension exceeds 20 GPa. Figure 4.16b shows Ni in HCP crystal structure became more stable than the FCC structure when the hydrostatic tension exceeded 22GPa with 5% hydrogen applied. Figure 4.16c shows that the averaged energy per atom was very similar in both FCC Ni and HCP Ni with 12.5% hydrogen applied. Figure 4.16d shows that the averaged energy per Ni atom was higher in HCP Ni than FCC Ni when hydrostatic tension was below 30GPa when 20.5% of hydrogen applied. Figures 4.16 indicate that Ni in the HCP structure was more stable than Ni in the FCC structure when the applied hydrostatic tension exceeds 20GPa and the hydrogen concentration was less than 5%. When the hydrogen concentration exceeded 12.5%, Ni in the FCC structure was always more stable than Ni in HCP structure as long as the applied hydrostatic tension did not exceed 30GPa. This explains why the dislocation structures arose in Figure 4.14. In the hydrogen-free case, a high percentage of FCC Ni changed into HCP Ni when the applied strain exceeded 16%, which corresponds to a hydrostatic stress of 20 GPa, shown in Figure 4.7. In the

precharged case, the hydrogen concentration in the specimen was only 0.125%, therefore, a high percentage of FCC Ni changed into HCP Ni when the applied strain exceeded 16%, which corresponds to a hydrostatic stress of 20GPa, shown in Figure 4.7. In the dynamically-charged case, the hydrogen concentration was higher than 12% after the applied strain exceeded 8%, and the hydrostatic tension was lower than 20GPa during the course of deformation. Therefore, Ni remained in the FCC structure during the deformation process.

Figures 4.16(a-d) show that it became more difficult for FCC Ni to change into HCP Ni with increasing hydrogen concentration. In FCC crystals, when a thin layer of FCC structure turns into HCP structure, a stacking fault forms. The previous study suggests that hydrogen discouraged the formation of stacking faults, and may have lowered the stacking fault energy of the system, which was observed in different types of metals by other researchers [14-15, 21]
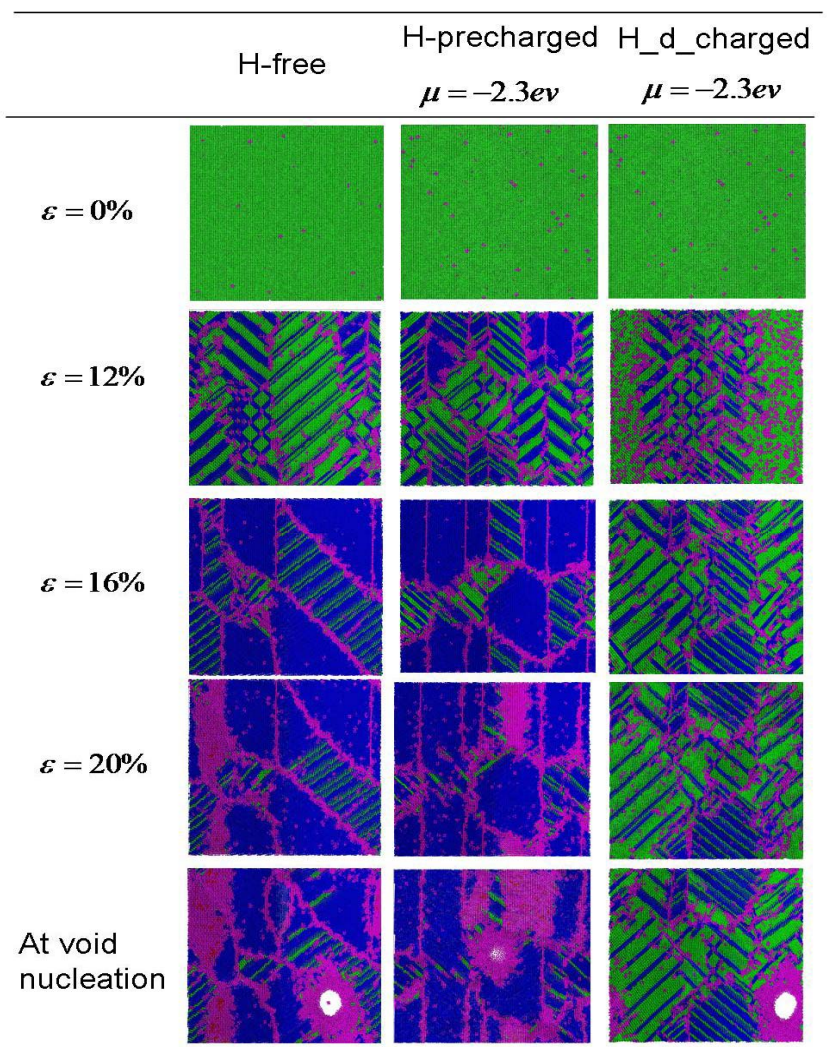
Figure 4.14.   The CNA snap shots of hydrogen-free, hydrogen precharged, and hydrogen dynamically-charged cases at 0%, 12%, 16%, and 20% strains, and at the point of nanovoid nucleation show that the dislocation structures are similar for the hydrogen-free and hydrogen-precharged cases. However, they are different for the hydrogen dynamically-charged condition. Here, ε denotes the applied strain and μ denotes the applied chemical potential. The white-colored regions denote nanovoids. In CNA snap shots, the color green is designated as a local FCC structure, the color blue represents the local HCP structure, and the color pink is an unknown lattice structure. Each snap shot includes the total simulation domain of Nickel crystals.
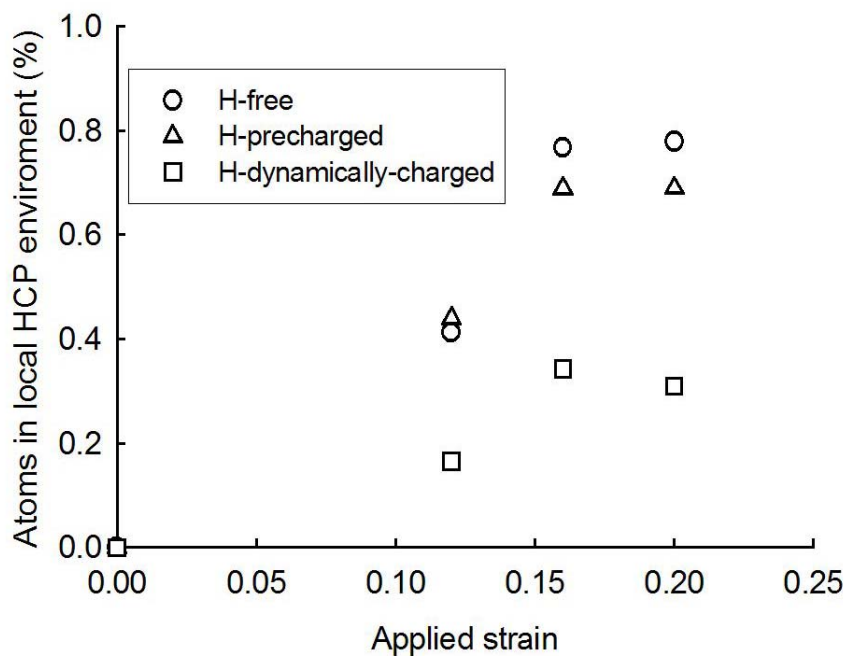
Figure 4.15. MD simulation results show the percentage of atoms in a local HCP environment versus applied strain. FCC atoms change into local HCP by partial dislocation nucleation. A higher number of HCP atoms in the H-free and H-precharged cases indicate a greater dislocation nucleation rate and a greater dislocation density.
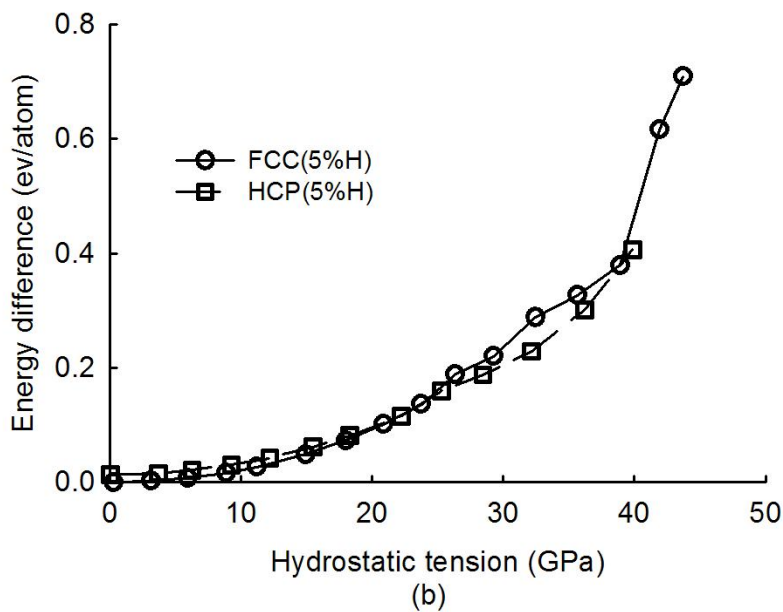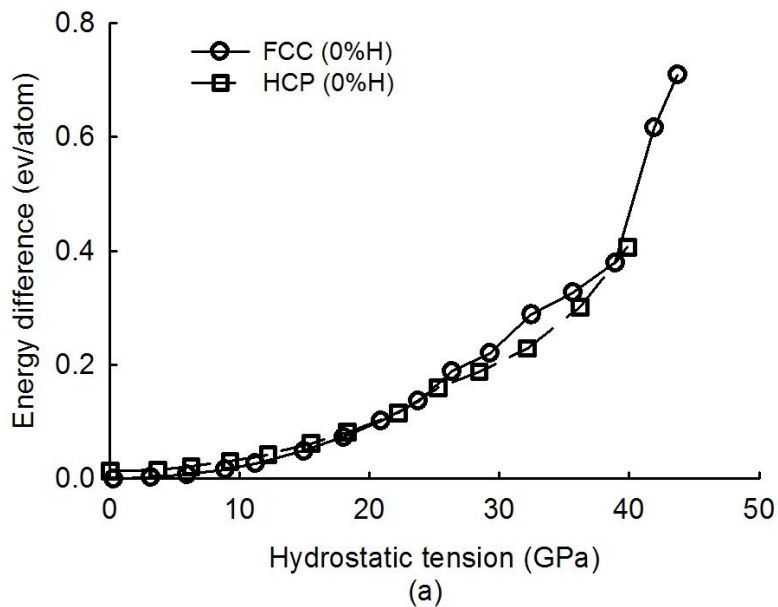
Figure 4.16. Energy difference versus hydrostatic tension in FCC Ni and HCP Ni with hydrogen-free (a), 5% hydrogen-charged case (b), 12.5% hydrogen-charged case (c) and 20.5% hydrogen-charged case (d).

Figure 4.16 (continued)

(c)

(d)
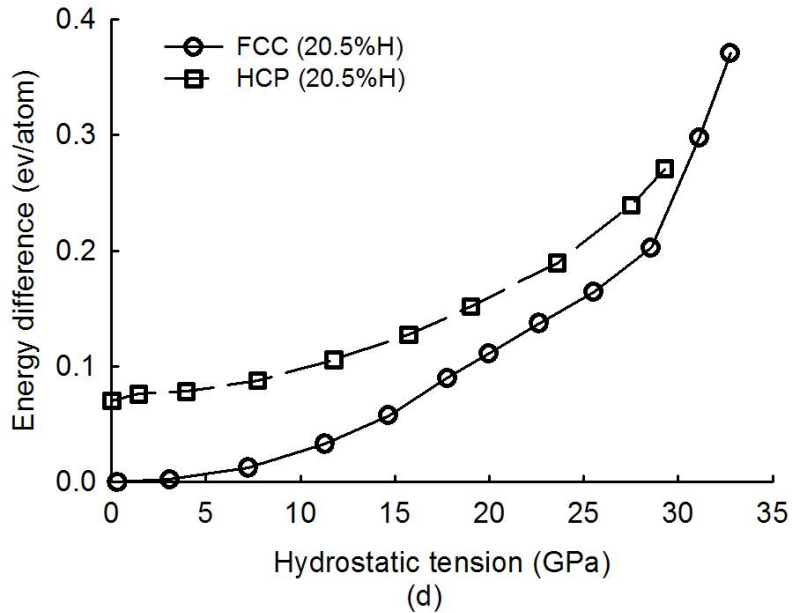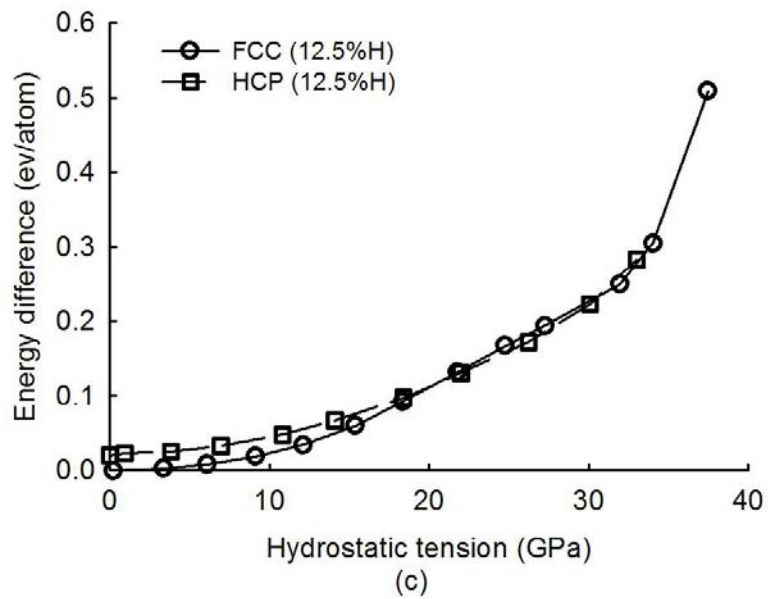
4.3.4 Relation to continuum void nucleation model

MD and MC simulation results indicate hydrogen promotes nanovoid nucleation in single crystal nickel in the dynamically-charged condition. To draw information on nanovoid nucleation and hydrogen concentrations from MD simulation results, in this section, we applied the MD results for the dynamically-charged case in the Horstemeyer and Gokhale model [47]. Stress invariants I_1, J_2 and J_3 at the point of nanovoid nucleation were calculated based on Equations (4.4), (4.5) and (4.6). Table 4.1 shows the stress invariant parameters at different hydrogen concentration. Table 4.1 shows that stress invariant parameters $\frac{4}{27} - \frac{J_3^2}{J_2^{3/2}}$ and $\frac{J_3}{J_2^{3/2}}$ are much smaller than stress triaxiality $\frac{I_1}{\sqrt{J_2}}$. Stress invariant parameters $\frac{4}{27} - \frac{J_3^2}{J_2^{3/2}}$ and $\frac{J_3}{J_2^{3/2}}$ were related to the deviatoric component of stresses, which were considered to be negligible here, because the nanovoid nucleated at high triaxial stress state in H-dynamically charged case, similar to the grain boundary study in Chapter III.

The MD simulation results in the dynamically-charged case were inserted in Equation (3.9) to calculate the void nucleation parameter $\frac{c_H}{c}$ at different hydrogen concentrations. Figure 4.17 shows that void nucleation parameter $\frac{c_H}{c}$ versus hydrogen concentration. Similar to results in the study on nanovoid nucleation at grain boundaries, the stress triaxiality-driven void nucleation parameter $\frac{c_H}{c}$ also increased exponentially with increasing hydrogen concentration. H-dynamically-charged case mainly addressed

nanovoid nucleation caused by hydrogen absorption due to the hydrostatic stress gradient. Based on Figure 4.17, in the case of hydrogen absorption from the hydrostatic stress gradient, the stress triaxiality-driven void nucleation parameter is also a function of local hydrogen concentration as:

$$\frac{c_H}{c} = e^{mH_\sigma}, \tag{4.9}$$

where H_σ is the local hydrogen concentration caused by the hydrostatic stress gradient, and m is related to material. According to Figure 4.17, m is approximately 1.72.

Based on [133], in a transit system, the local hydrogen concentration due to hydrostatic stress gradient can be calculated as follows:

$$\dot{H}_\sigma = D\nabla^2 H_L - \frac{D\overline{V}}{RT}\left[H_L\nabla^2\frac{\sigma^{kk}}{3} + \vec{\nabla}H_L\vec{\nabla}\frac{\sigma^{kk}}{3}\right] \tag{4.10}$$

where H_σ is the local hydrogen concentration, H_L is the bulk hydrogen concentration, D is the hydrogen diffusion coefficient of the alloy, $\overline{V}$ is the partial molar volume of hydrogen.

Table 4.1. Stress state parameters $\frac{4}{27} - \frac{J_3^2}{J_3}$, $\frac{J_3}{J_2^{3/2}}$ and $\frac{I_1}{\sqrt{J_2}}$ were calculated from MD
           simulation results at nanovoid nucleation in H-dynamically charged condition
           at different hydrogen concentrations.

Hydrogen concentration (atomic)	$\frac{4}{27} - \frac{J_3^2}{J_2^{3/2}}$	$\frac{J_3}{J_2^{3/2}}$	$\frac{J_3}{\sqrt{J_2}}$
0	0.039	0.33	121.62
0.4	0.073	0.274	68.54
0.47	0.017	0.362	53

Table 4.1 (continued)

0.53	0.016	0.363	51
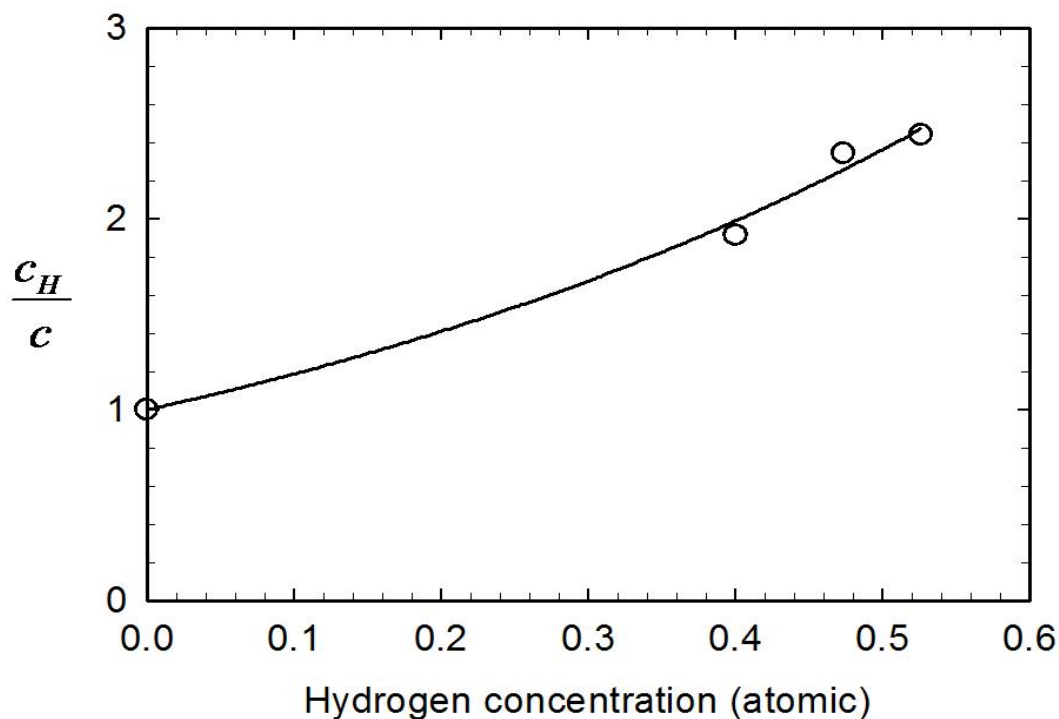
Figure 4.17. MD simulation results in the dynamically-charged case were inserted into Horstemeyer and Gokhale continuum void nucleation model. The material constants related to stress triaxiality-driven void nucleation in the H-dynamically charged case, c_H, increased exponentially with increased hydrogen concentration, which was described in Equation 4.9. Here, the exponential coefficient is approximately 1.72.

4.4   Discussion

The simulation results indicate that different mechanisms may have played roles in the hydrogen-precharged and the dynamically-charged cases.

In the precharged condition, the stress-strain curves followed the same trend as in the hydrogen-free condition until a nanovoid nucleated; the dislocation density changed little; the dislocation substructures were similar to the hydrogen-free case. The small reduction on the fracture hydrostatic stress and fracture strain may be caused by hydrogen-induced reduction on the cohesive strength of the lattice, a hydrogen-enhanced decohesion mechanism [13]. However, the effects were very small and ductility of the specimen changed little, which agrees with the experimental results by Windle and Smith [3]. Hydrogen was precharged in the specimen in their experiments.

In the dynamically-charged condition, hydrostatic stress component was lowered by hydrogen; dislocation density was lower; much fewer FCC atoms change into HCP atoms because high hydrogen concentration possibly caused a reduction on stacking fault energy of the system; the fracture stresses were reduced markedly and fracture strains were only slightly reduced. This suggests that hydrogen enhances nanovoid nucleation by reducing the hydrostatic stress for void nucleation. If a crack is advancing by void nucleation and void growth ahead of the crack, hydrogen can lower the stress for a void to nucleate in front of the crack and the crack will advance at a lower stress. This finding agrees with experimental results by Robertson and Birnbaum [16]. Robertson and Birnbaum found that hydrogen decreased the stress required for crack advance in dynamically-charged experiments.

In the dynamically-charged condition, very high hydrogen concentration was present in the specimen due to the high hydrostatic stress. The MD simulation results

were inserted into the Horstemeyer and Gokhale model and a stress triaxiality-driven void nucleation parameter was plotted against hydrogen concentrations.

4.5   Summary of Chapter 4

Monte Carlo simulations and Molecular Dynamics simulations were carried out to study the nanovoid nucleation of nickel single crystal in hydrogen-precharged and hydrogen-dynamically conditions and the associated precursor plasticity mechanisms that led up to nanovoid nucleation. Although the fracture strains only slightly decreased with the addition of hydrogen, the fracture stress decreased dramatically. More specified main points of this study are summarized as the following.

- The hydrogen concentration increased with increasing chemical potential in the precharged condition and in the dynamically-charged condition. The hydrogen concentration in the dynamically-charged condition was much higher than in the precharged condition due to hydrogen transport by the tensile hydrostatic stress caused chemical potential gradient.

- The precharged condition represented a bulk condition, in which hydrogen did not diffuse. Plastic flow was slightly reduced and the dislocation structure changed little. The critical stress and strain at nanovoid nucleation was slightly reduced possibly by hydrogen-induced reduction on the cohesive strength.

- The dynamically-charged condition represented a type of transient state, in which hydrogen was absorbed into the specimen, because of the presence of tensile hydrostatic stress and dislocations induced by plastic deformation. Hydrogen

caused a reduction in hydrostatic stress and small increase in yield stress. Hydrogen also discouraged stacking faults from forming. As a result, the nanovoid nucleation occurred at a much lower stress and at only a slightly lower strain.

- MD simulation results suggest that hydrogen promotes nanovoid nucleation mainly by lowering the critical hydrostatic stress for nanovoid nucleation when hydrogen is transported by stress gradient and plastic deformation into the specimen in single crystals. The MD simulation results were inserted into Horstemeyer and Gokhale model. The stress triaxiality-driven void nucleation parameter also followed an exponential form with local hydrogen concentration. This information can be used in the development of a continuum void nucleation model in the next chapter.

CHAPTER V

A CONTINUUM HYDROGEN-ASSISTED VOID NUCLEATION MODEL FOR DUCTILE MATERIALS

5.1   Introduction

Ductile material deformation involves irreversible, path-dependent processes such as plastic deformation, fracture and diffusion [134]. To capture these processes in a continuum model, a set of internal state variables can be used to represent the physical processes associated with irreversible, path-dependent material behavior. For example, three internal state variables were used in the BCJ continuum damage model [53-54]: damage, isotropic hardening, and kinematic hardening. Damage addresses microstructure evolution due to void nucleation, void growth, and void coalescence. The isotropic hardening variable addresses the plastic flow from the evolution of the statistically-stored dislocations. Kinematic hardening addresses the plastic flow from the evolution of geometrically necessary dislocations.

Experiments [130-131] and simulations [32] clearly show that hydrogen can affect the bulk plastic deformation and fracture of ductile materials; hydrogen diffusion in the material   affects deformation processes [135]. Hydrogen can cause either material hardening or softening by interacting with dislocations or with impurities [130].

97

Hydrogen can induce shear localization and plastic instability, which leads to premature material failure [136]. Furthermore, hydrogen diffusion along the grain boundaries and interfaces encourages intergranular failures [116]. To include hydrogen effects in the constitutive formulations to study ductile material damage, we propose two internal state variables: a thermodynamic displacement related to statistically-stored dislocations and a damage variable that is a function of hydrogen. Hydrogen can affect plastic flow by lowering the energy barrier for dislocation slip and reducing the dislocation spacing [137]. However, hydrogen enhancing damage is one of most dominate mechanisms in the hydrogen-induced failure process. Hydrogen can cause an elongation-to-failure to decrease, which is caused by the damage progression. In particular, hydrogen-induced void nucleation may be the main driving force for hydrogen-assisted fracture.

The MD and MC simulation results in the previous chapters show that hydrogen causes nanovoid nucleation to occur at lower stresses and strains. In this chapter, the kinematic, thermodynamic, kinetics and flow rules of the constitutive equations of a continuum damage framework are proposed. The emphasis is placed upon the void/crack nucleation mechanism related to bulk hydrogen effects and upon developing a model to capture its phenomenological nature in the context of internal state variable plasticity and damage equations.

5.2   Kinematics of a Continuum Damage Framework with Hydrogen Effects

All equations are written in the current configuration. The tensors are denoted with underlines.

Because the material volume can deform elastically and plastically, so the elastic velocity gradient $\underline{L}^e$ and the plastic velocity gradient $\underline{L}^p$ are included in the total velocity gradient. The damage can induce a material volume change, so we include a velocity gradient induced by damage, $\underline{L}^\Phi$. Because hydrogen causes a dilatational volume change of material, we also include a hydrogen-induced velocity gradient, $\underline{L}^H$. The total velocity gradient is written as:

$$\underline{L} = \underline{L}^e + \underline{L}^p + \underline{L}^\phi + \underline{L}^H \tag{5.1}$$

For small strain, the anti-symmetric component of the velocity gradient is zero, therefore, the strain tensors can be written as:

$$\dot{\underline{\varepsilon}} = \dot{\underline{\varepsilon}}^e + \dot{\underline{\varepsilon}}^p + \dot{\underline{\varepsilon}}^\phi + \dot{\underline{\varepsilon}}^H \tag{5.2}$$

where $\underline{\varepsilon}^e$, $\underline{\varepsilon}^p$, $\underline{\varepsilon}^\Phi$ and $\underline{\varepsilon}^H$ are the elastic strain, plastic strain, damage-induced volumetric strain and hydrogen-induced volumetric strain.

Based on [88, 138], we assume that damage-induced deformation is isotropic, and damage-induced strain may be written as:

$$\dot{\underline{\varepsilon}}^\phi = \frac{1}{3}(1-\phi)^{-1}\dot{\phi}\underline{I} \tag{5.3}$$

Based on Alefeld and Jvölkl [139], assume that hydrogen dilatational deformation is also isotropic, and hydrogen dilatational strain may be written as;

$$\dot{\underline{\varepsilon}}^H = \frac{1}{3}\frac{d}{dt}\left\{\ln\left[1+\frac{H\overline{V}}{\Omega}\right]\right\}\underline{I} = \frac{\overline{V}\dot{H}}{3(\Omega+H\overline{V})}\underline{I} \; , \tag{5.4}$$

where H is atomic hydrogen concentration, $\overline{V}$ is hydrogen partial molar volume, Ω is the mean atomic volume of the host metal atom.

5.3 Thermodynamics of a Continuum Damage Framework with Hydrogen Effects

The first law of thermodynamic in the local form is given by Malven [134]

$$\rho \dot{u} = \underline{\sigma} : \underline{\dot{\varepsilon}} + \varsigma - \underline{\nabla} \cdot \underline{q} \quad , \tag{5.5}$$

where u is the internal energy per unit mass, $\underline{\sigma}$ is the Cauchy stress tensor, ς is the specific heat generation rate, and $\underline{q}$ is the heat flux vector and ρ is the density.

The second law of thermodynamic in the local form is given:

$$\dot{\mu}_T - \frac{1}{\rho}\frac{\varsigma}{T} + \frac{1}{\rho}\underline{\nabla} \cdot \frac{\underline{q}}{T} \geq 0 \tag{5.6}$$

where μ_T is specific entropy related to dissipation and T is absolute temperature,

Eliminate ζ and combine equations (5.5) and (5.6) and we get:

$$\dot{\mu}_T + \frac{1}{\rho}\underline{\nabla} \cdot \frac{\underline{q}}{T} - \frac{1}{\rho T}(\rho \dot{u} - \underline{\sigma} : \underline{\dot{\varepsilon}} + \underline{\nabla} \cdot \underline{q}) \geq 0 \tag{5.7}$$

Noting that:

$$\underline{\nabla} \cdot \frac{\underline{q}}{T} = \frac{\underline{\nabla} \cdot \underline{q}}{T} - \frac{\underline{q} \cdot \underline{\nabla} \cdot T}{T^2} \tag{5.8}$$

Equation (5.7) can be written as:

$$\rho(T\dot{\mu}_T - \dot{u}) + \underline{\sigma} : \underline{\dot{\varepsilon}} - \underline{q} \cdot \frac{\underline{\nabla} \cdot T}{T^2} \geq 0 \tag{5.9}$$

After Coleman and Gurtin [140], assume a Helmholtez free energy per unit mass, ψ, as the following

$$\psi = u - \mu_T T \tag{5.10}$$

$$\dot{u} = \dot{\psi} + \dot{\mu}_T T + \mu_T \dot{T} \tag{5.11}$$

Substitute equation (5.11) into equation (5.9) and obtain the Clausius-Duhem inequality:

$$\underline{\sigma} : \dot{\underline{\varepsilon}} - \rho(\dot{\psi} + \mu_T \dot{T}) - \underline{q} \cdot \frac{\nabla \cdot T}{T} \geq 0 \tag{5.12}$$

The free energy, ψ, may be defined as a function of a local state, which may be characterized by observable variables such as temperature, elastic strain $\underline{\varepsilon}^e$ and internal state variables such as thermodynamic displacement caused by statistically stored dislocations, ε^{ss}, and damage, ϕ. The earlier atomistic simulations show that hydrogen can enhance damage by reducing the required energy for void nucleation. The study done by Liang and Sofronis [136] demonstrate that hydrogen can enhance void coalescence by HELP mechanism. Apparently, hydrogen can affect free energy of the system by enhancing damage. Hence, the free energy of the system is defined as a function of the elastic strain, the internal thermodynamic displacement caused by statistically stored dislocations [141], damage and temperature.

$$\psi = \psi(\underline{\varepsilon}^e, \varepsilon^{ss}, \phi, T) \tag{5.13}$$

Take the derivative of ψ to get the following,

$$\dot{\psi} = \frac{\partial \psi}{\partial \underline{\varepsilon}^e} : \underline{\varepsilon}^e + \frac{\partial \psi}{\partial \varepsilon^{ss}} \dot{\varepsilon}^{ss} + \frac{\partial \psi}{\partial \phi} \dot{\phi} + \frac{\partial \psi}{\partial T} \dot{T} \tag{5.14}$$

Substitute Equation (5.2) and (5.14) into Equation (5.12) and get:

$$(\underline{\sigma} - \rho \frac{\partial \psi}{\partial \underline{\varepsilon}^e}) : \dot{\underline{\varepsilon}}^e - (\mu_T + \rho \frac{\partial \psi}{\partial T})\dot{T} + \underline{\sigma} : \dot{\underline{\varepsilon}}^p + \underline{\sigma} : \dot{\underline{\varepsilon}}^\phi + \underline{\sigma} : \dot{\underline{\varepsilon}}^H - \rho \frac{\partial \psi}{\partial \varepsilon^{ss}} \dot{\varepsilon}^{ss}$$
$$- \rho \frac{\partial \psi}{\partial \phi} \dot{\phi} - \underline{q} \cdot \frac{\nabla \cdot T}{T^2} \geq 0 \tag{5.15}$$

Similar to [142],

$$\underline{\sigma} = \rho \frac{\partial \psi}{\partial \underline{\varepsilon}^e} \tag{5.16}$$

$$\mu_T = -\rho \frac{\partial \psi}{\partial T} \tag{5.17}$$

Thus, Equation (5.14) can be simplified as:

$$\underline{\sigma} : \underline{\dot{\varepsilon}}^p + \underline{\sigma} : \underline{\dot{\varepsilon}}^\phi + \underline{\sigma} : \underline{\dot{\varepsilon}}^H - \rho \frac{\partial \psi}{\partial \varepsilon^{ss}} \dot{\varepsilon}^{ss} - \rho \frac{\partial \psi}{\partial \phi} \dot{\phi} - \underline{q} \cdot \frac{\nabla \cdot T}{T^2} \geq 0 \tag{5.18}$$

The first term is the external work from deviatoric plastic deformation; the second term is the external work from damage-induced volumetric expansion, the third term is the external work from hydrogen-induced volumetric expansion, the fourth term is the dissipation from internal work from the dislocations, the fifth term is the dissipation from damage, the sixth term is a convection term. The fourth and the fifth terms are related to internal state variables. The thermodynamic forces associated with the internal state variables can be defined by:

$$\kappa = \rho \frac{\partial \psi}{\partial \varepsilon^{ss}} \tag{5.19}$$

$$Y = \rho \frac{\partial \psi}{\partial \phi} \tag{5.20}$$

where κ is the thermodynamic force conjugate to statistically stored dislocations-induced thermodynamic displacement, which is also defined as an isotropic hardening variable and can be thought as the stress related to forest dislocations. Y is the thermodynamic force conjugated to damage, which can be thought as an elastic energy release rate induced by increasing damage.

For a small-strain system, the free energy is written as:

$$\rho\psi = \frac{1}{2}\underline{\varepsilon}^{eT} : \underline{C}(1-\phi)\underline{\varepsilon}^e + \frac{1}{2}H^{ss}\varepsilon^{ss^2} \ , \tag{5.21}$$

where $\underline{C}$ is elastic moduli. H^{ss} is related to the isotropic hardening moduli.

Substitute equation (5.21) into equations (5.16) and (5.19) and get:

$$\underline{\sigma} = \underline{C}(1-\phi)\underline{\varepsilon}^e \tag{5.22}$$

$$\kappa = H^{ss}\varepsilon^{ss} \tag{5.23}$$

Take the derivative of equations (5.22) and (5.23) and get rate forms:

$$\underline{\dot{\sigma}} = \underline{C}(1-\phi)\underline{\varepsilon}^e - \dot{\phi}\underline{C}\underline{\dot{\varepsilon}}^e = \underline{C}(1-\phi)\underline{\dot{\varepsilon}}^e - \frac{\dot{\phi}}{1-\phi}\sigma \tag{5.24}$$

$$\dot{\kappa} = H^{ss}\dot{\varepsilon}^{ss} \tag{5.25}$$

Equation (5.24) can be written as:

$$\underline{\dot{\sigma}} = \lambda(1-\phi)tr(\underline{\varepsilon}^e) + 2\mu^s(1-\phi)\underline{\varepsilon}^e - \frac{\dot{\phi}}{1-\phi}\sigma \tag{5.26}$$

where λ is the bulk modulus, μ^s is the shear modulus.

The elastic strain of statistically-stored dislocations is a function of dislocation density [141:

$$\varepsilon^{ss} = \bar{b}\sqrt{\rho_{ss}} \tag{5.27}$$

where ρ_{ss} is the dislocation density and $\bar{b}$ is Burger's vector.

According to Kocks-Mecking model [143], the dislocation density evolves by storage minus recovery event. The dislocation density satisfies:

$$\frac{d\rho_{ss}}{d\|\underline{\varepsilon}^p\|} = c_1\sqrt{\rho_{ss}} - c_2\rho_{ss} \ , \tag{5.28}$$

where c_1 and c_2 are material constants.

Based on Equation (5.25), (5.27) and (5.28), the isotropic hardening variable, κ, is written as:

$$\dot{\kappa} = (\frac{\overline{b}c_1}{2}H^{ss} - c_2\kappa)\left\|\underline{\dot{\varepsilon}}^p\right\|$$ (5.29)

Simplify Equation (5.29) into:

$$\dot{\kappa} = (H^\kappa - R^\kappa\kappa)\left\|\underline{\dot{\varepsilon}}^p\right\|$$ (5.30)

where H^κ is the isotropic hardening modulus, R^κ is the dynamic recovery parameter.

These two terms are normally functions of temperature. However, only ambient

Temperature is considered and they are constants here.

Substitute Equation (5.3) and (5.4) into (5.2) and get:

$$\underline{\dot{\varepsilon}}^e = \underline{\dot{\varepsilon}} - \underline{\dot{\varepsilon}}^p - \underline{\dot{\varepsilon}}^\phi - \underline{\dot{\varepsilon}}^H = \underline{\varepsilon} - \underline{\dot{\varepsilon}}^p - \frac{\dot{\phi}}{3(1-\phi)}\underline{I} - \frac{\overline{V}\dot{H}}{3(\Omega + H\overline{V})}\underline{I}$$ (5.31)

Based on [54], the deviatoric flow rule is assumed as:

$$\underline{\dot{\varepsilon}}^p = f(T)\sinh\left[\frac{\|\sigma\| - \kappa - Y(T)(1-\phi)}{V(T)(1-\phi)}\right]\frac{\underline{\sigma}}{\|\sigma\|}$$ (5.32)

where $V(T)$, $f(T)$ and $Y(T)$ are used to describe temperature dependences of the yield

functions. All those functions have forms according to [53-54]:

$$V(T) = C_1\exp(-\frac{C_2}{T})$$ (5.33)

$$Y(T) = C_3\exp(\frac{C_4}{T})$$ (5.34)

$$f(T) = C_5\exp(-\frac{C_6}{T})$$ (5.35)

5.4   Kinetics of a Continuum Damage Framework with Hydrogen Effects

In this model, damage is related to void nucleation, void growth and void coalescence in a linear rate form:

$$\phi = \eta v C \tag{5.36}$$

$$\dot{\phi} = \dot{\eta} v C + \eta \dot{v} C + \eta v \dot{C} \tag{5.37}$$

where η is the void nucleation, v is the void growth, and C is the void coalescence.

5.4.1 *Void growth model and void coalescence model*

Experiments [28-31] and simulations [33, 136] suggest hydrogen enhances void growth and coalescence. However, in this study, hydrogen effects on the void growth and the void coalescence were not considered, only the void nucleation was considered.

Mclintock's model [144] for the growth of spherical voids in a rate-independent plastic material was used:

$$v = \frac{4}{3}\left(R_0 \exp\left[\varepsilon(t) \frac{\sqrt{3}}{2(1-n)} \times \sinh\left(\sqrt{3(1-n)}\right) \frac{\sqrt{2}I_1}{3\sqrt{J_2}} \right] \right)^3 \tag{5.38}$$

where R_o is the initial radius of average void size, and n is the strain hardening exponent of the material.

Based on [88], the void coalescence model is:

$$\dot{C} = C_{coal}[\eta\dot{v} + \dot{\eta}v]\exp(C_{CT}T) , \tag{5.39}$$

where C_{coal} is a material constant. C_{CT} is related to the temperature dependence on void coalescence.

5.4.2 *Void nucleation model*

This work is to develop a hydrogen-enhanced continuum void nucleation model by adding hydrogen effects into the Horstemeyer and Gokhale model [47], based on MD

simulations results presented in the previous chapters. The Horstemeyer and Gokhale void nucleation rate equation [47] was described in section 3.4, Chapter III.

To use the information from MD simulation results appropriately, the length scale, in which each term resides in the continuum nucleation equation [47], needs to be understood. Figure 5.1 is used to illustrate the concept. Void number density, η, is a continuum quantity. The diameter of the second phase particle, d, is from a lower length scale, which is usually at the microscale and can be at the nanoscale if the particle size is at the nanoscale. The volume fraction of second phase particles is also from a lower length scale, which corresponds to the number of sites possible for void nucleation, because void nucleation can occur either by fracture of second phase particles or by interfacial debonding. Strains and stresses all are continuum quantities. Void nucleation coefficients, a, b and c are at the microscale or at the nanoscale and are related to local stresses at interfaces, inclusions and second phase particles. MD simulations results provided information on how hydrogen affects void nucleation coefficients a, b and c.
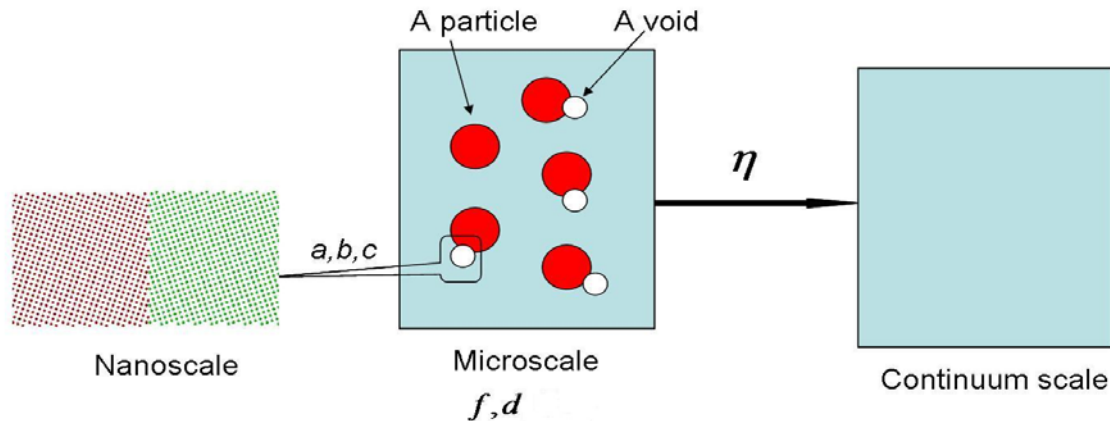
Figure 5.1. Void number density η, a continuum quantity, is a function of microscale quantities: particle number density f, particle size d and void nucleation coefficients, a, b and c. Nanoscale simulations can provide information on void nucleation coefficients a, b and c.

MD simulation results in the grain boundaries study (see Chapter III) show that hydrogen lowers the critical hydrostatic stress and critical strain for void nucleation if hydrogen is trapped at and near grain boundary planes. MD simulation results in single crystals study show that hydrogen reduces the critical hydrostatic stress for void nucleation if hydrogen is transported by stress gradient and deformation-induced dislocations. Dighe and coworkers [55] also found that interfacial debonding at a particle-matrix interface was mainly caused by a hydrostatic tensile stress. Therefore, hydrogen-induced void nucleation by interfacial debonding is addressed by adding a hydrogen-related factor $G(H)$ in the term that associated with the stress triaxiality.

$$\dot{\eta}_H = \frac{\left\| \varepsilon^p \right\| \eta d^{1/2}}{K_{IC} f^{1/3}} \left\{ a \left[\frac{4}{27} - \frac{J_3^2}{J_2^3} \right] + b \frac{J_3}{J_2^{3/2}} + G(H) c \left| \frac{I_1}{\sqrt{J_2}} \right| \right\} \tag{5.40}$$

MD simulation results in Chapter III show that *G(H)* is an exponential function of grain boundary hydrogen concentration induced by trapping at defects at grain boundaries. MD simulation results in Chapter IV shows that *G(H)* is also an exponential function of the local hydrogen concentration caused by a hydrostatic stress gradient and deformation-induced dislocations. Therefore, the form for *G(H)* is chosen as:

$$G(H) = e^{mH_\sigma} \tag{5.41}$$

Hence, the new hydrogen-enhanced void nucleation rate equation is:

$$\dot{\eta}_H = \frac{\left\|\underline{\varepsilon}^p\right\|\eta_H d^{1/2}}{K_{IC}f^{1/3}}\left\{a\left[\frac{4}{27}-\frac{J_3^2}{J_2^3}\right]+b\frac{J_3}{J_2^{3/2}}+ce^{mH_\sigma}\left|\frac{I_1}{\sqrt{J_2}}\right|\right\}, \tag{5.42}$$

take integration and get the void nucleation equation:

$$\eta_H = C_\eta \exp\left(\frac{\left\|\underline{\varepsilon}^p\right\|\eta_H d^{1/2}}{K_{IC}f^{1/3}}\left\{a\left[\frac{4}{27}-\frac{J_3^2}{J_2^3}\right]+b\frac{J_3}{J_2^{3/2}}+ce^{mH_\sigma}\left|\frac{I_1}{\sqrt{J_2}}\right|\right\}\right) \tag{5.43}$$

where H_σ is local hydrogen concentration, which can include hydrogen absorption by defects- trapping and stress gradient, *m* is a material constant related to material and local interfaces, C_η is the initial void volume/area density. Note that as the local hydrogen concentration approaches zero, the Horstemeyer-Gokhale nucleation model is fully recovered.

5.4.3 *Local hydrogen concentrations*

Local hydrogen concentrations can be affected by hydrogen trapping at microstructural defects such as interfaces, grain boundaries, voids and cracks [107], can

be also affected by local stress state [135] and by dislocations induced by plastic deformation. The grain boundary study addressed the local hydrogen concentration by hydrogen trapping at the grain boundaries, and the single crystal study addressed the local hydrogen concentration caused by stress gradient and deformation-induced dislocations. The grain boundary study addressed a hydrogen equilibrium state, while the single crystal study addressed a hydrogen transit state.

For a hydrogen equilibrium state, local hydrogen concentration can be evaluated based on the following methods.

The hydrogen concentration at interstitial sites, H_L, is related to applied hydrogen pressure according to Sievert's law [113].

$$H_L = 2226\sqrt{P_{H_2}}\exp(\frac{-6850}{RT}),\tag{5.44}$$

where P_{H_2} is hydrogen gas pressure in MPa.

Based on McLean [57] and Oriani's theory [145] and, at equilibrium state, the hydrogen concentration trapped at the interfaces, H_B, is related to the hydrogen concentration at interstitial sites, H_L as:

$$\frac{H_B}{1-H_B} = \frac{H_L}{1-H_L}\exp(\frac{-W_B}{RT}),\tag{5.45}$$

where W_B is trap binding energy at the interface, R is gas constant and T is absolute temperature.

At the equilibrium state, local hydrostatic concentration in a region with positive hydrostatic stress is higher than the unstressed region. The local hydrogen concentration in a stressed region, H_σ, is related to the concentration in a unstressed region H_B as:

$$H_\sigma = H_B \exp(\frac{\sigma_{kk}\overline{V}}{3RT}),$$
(5.46)

For a hydrogen transit state, Taha and Sofronis [146] proposed a model of the rate of local hydrogen concentration:

$$\dot{H}_\sigma = \frac{D}{\left(1+\frac{H_B}{H_L}\right)}\nabla^2 H_L - \frac{D\overline{V}}{\left(1+\frac{H_B}{H_L}\right)RT}\left[H_L\nabla^2\frac{\sigma^{kk}}{3} + \vec{\nabla}H_L\vec{\nabla}\frac{\sigma^{kk}}{3}\right]$$
$$- N_\alpha\theta_T\frac{\partial N_T}{\partial\varepsilon^p}\frac{\partial\varepsilon^p}{\partial t}$$
(5.47)

where H_L is the hydrogen concentration at interstitial sites corresponding to the bulk hydrogen concentration described earlier, H_B is the hydrogen concentration trapped at microstructural defects corresponding to the grain boundary hydrogen concentration described earlier, D is the hydrogen diffusion coefficient of the alloy, N_α is the number of sites per trap, N_T is the trap density measured in number of traps per unit volume, θ_T denotes the occupancy of the trapping sites, the ε^p is the local plastic strain. The last term in Equation (5.47) is related to hydrogen trapped by dislocations induced by plastic deformation.

5.5   Model Implementation and Correlation

The continuum damage framework with the new hydrogen-enhanced void nucleation model was implemented into user material code UMAT, which can be used with commercial FEA code ABAQUS to predict void nucleation and damage. The existing experimental data on 1518 spheroidized steel [38] was used to validate the model

5.5.1   *Parameter correlation for plasticity in 1518 spheroidized steel*

To implement equations in the previous sections, a number of constants related to plasticity of 1518 spherodized steel needed to be determined. BCJ Fit is a code which uses least square curve fitting method to find constants that correlate with the experimental stress-strain curves. Figure 5.2 shows a simple stress-strain curve provided for 1518 spheroidized steel by Kwon and Asaro [38], and a number of plastic constants were correlated from it, which is shown in Table 5.1. Because rate-dependence and temperature-dependence on yielding and strain hardening was neglected in this study, the constants addressing temperature and rate dependence are zero.
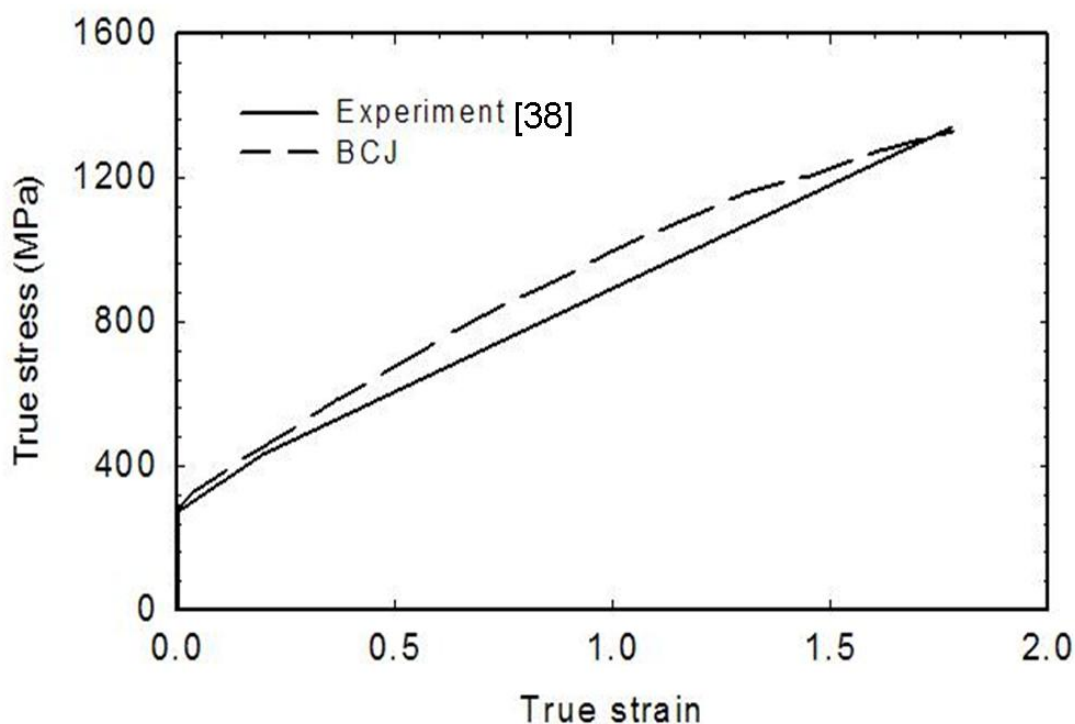
Figure 5.2.   The stress-strain curve from the experimental data on 1518 spheroidized steel is correlated with BCJ fit. A number of plastic constants are correlated from the experimental data [38].

Table 5.1. Plasticity parameters were correlated from experimental data. Constants C_1,
C_2, C_3, C_4, C_5 and C_6 are material constants that relate to yielding with
temperature dependence.

Bulk Modulus λ (MPa)	79620
Shear Modulus μ^s (MPa)	172500
Isotropic hardening modulus H^κ (MPa)	160
Dynamic recovery parameter R^κ	0
C_1	0
C_2	0
C_3 (MPa)	293
C_4	0
C_5	0
C_6	0

5.5.2 *Void nucleation parameters correlation for uncharged specimens in 1518 spheroidized steel*

According to Kwon and Asaro, in 1518 spheroidized steels, voids were nucleated by interface separation at large inclusions and carbide particles. The experimental data on the smooth specimens and notched specimens without hydrogen were used to correlate the initial void volume density and void nucleation coefficient a, b and c in Equation (5.43). Normally, the void volume densities of smooth specimens need to be evaluated under uniaxial tension, uniaxial compression and pure torsion in order to determine material constants a, b and c and initial void volume density C_η [47]. For example, coefficient a, is usually determined from torsion results. Coefficients b and c are

determined from tension and compression. Experiments by Asaro and Kwon only included void area density versus plastic strain of smooth specimens under uniaxial tension and notch tensile specimens. No torsion data was available to determine coefficient *a*. However, since the purpose here is to validate hydrogen effects on void nucleation. Hydrogen is only added to the material constant associated with stress triaxiality. Therefore, $a = 0$ was assumed, *b*, *c* and initial void volume density $C\eta$ were determined by correlating the void volume density curve of the smooth specimens under uniaxial tension and notch specimens under uniaxial tension. Figure 5.3 shows the void volume density versus plastic strain of the smooth and notch data without hydrogen by model prediction and experiments. Based on Figure 5.3, void nucleation coefficients *b*, *c* and initial void volume density, C_η were found to be the following: $b = 50000$MPa, $c = 5000$MPa and $C_\eta = 7.5e7$ cm^{-3}.
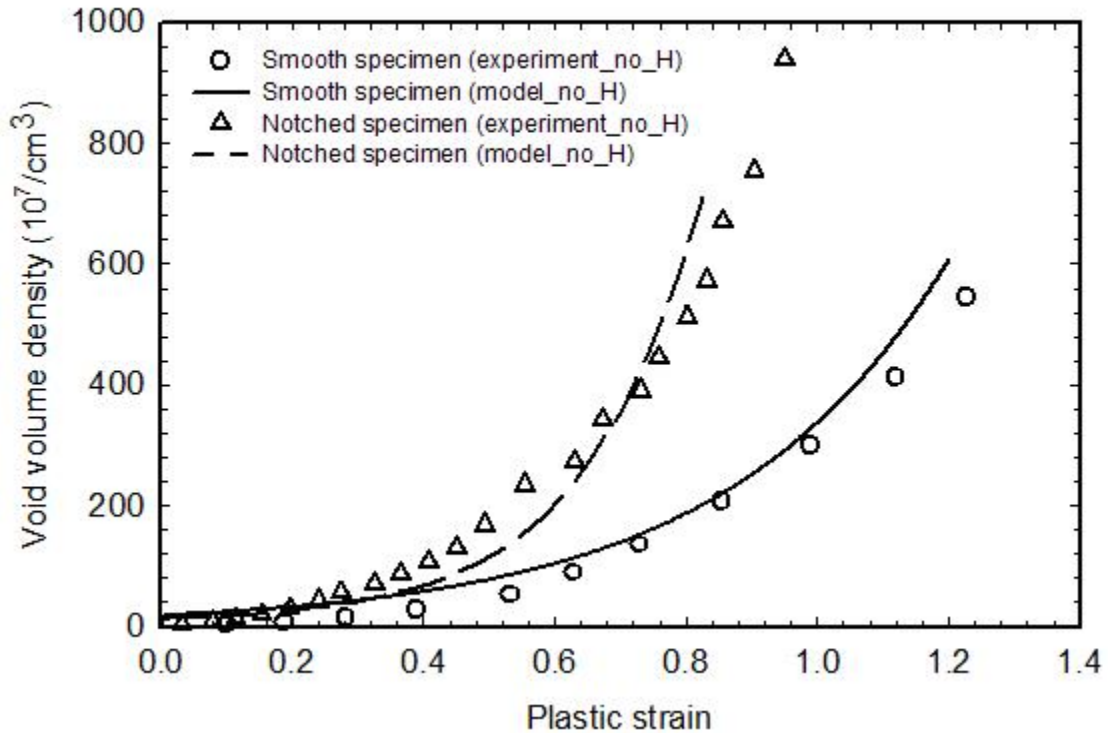
Figure 5.3.   The experimental data of void nucleation density versus plastic strain for smooth and notched specimens is correlated with Horstemeyer and Gokhale void nucleation model [47].

5.5.3   *Void growth and void coalescence parameters*

Based on Kwon and Asaro [38], the parameters for void growth are:

R_o = 0.25e-6 (m) n=0.092

In this study, void coalescence was not considered:

C=1

5.5.4   *Model correlation and validation with 1518 spheroidized steel*

5.5.4.1 *Local Hydrogen concentration*

In Kwon and Asaro's experiments, hydrogen was electrochemically charged into the specimens before the mechanical tests were performed under an extremely slow strain rate of 6.6e-4/s. Hence hydrogen is considered to have reached an equilibrium state. Thus the local hydrogen concentration was calculated based on the equations described in the previous section for the equilibrium state. Hydrogen-related parameters are needed to calculate the local hydrogen concentrations. Table 5.2 shows the hydrogen-related parameters.

Table 5.2. The following parameters are used to calculate the local hydrogen concentrations.

Trap binding energy W_B [147]	-56KJ/mol
Gas Constant R	8.31J mol^{-1}K^{-1}
Temperature T	300K
Partial molar volume of hydrogen $\overline{V}$ [148]	1.72 cm^3/mol

The local hydrogen concentrations trapped at the interfaces at the unstressed condition was calculated for different bulk hydrogen concentrations based on Equation (5.46) and the parameters provided from Table 5.2. Figure 5.5 shows that the local hydrogen concentration at the interfaces increased with bulk hydrogen concentration and then saturated after hydrogen occupied all the trap sites, and the interface hydrogen concentration was much higher than bulk hydrogen concentration due to high trap

binding energy at the interface. This indicates that even if the solubility of hydrogen is usually very small in many alloys, the local hydrogen concentration can be very high.
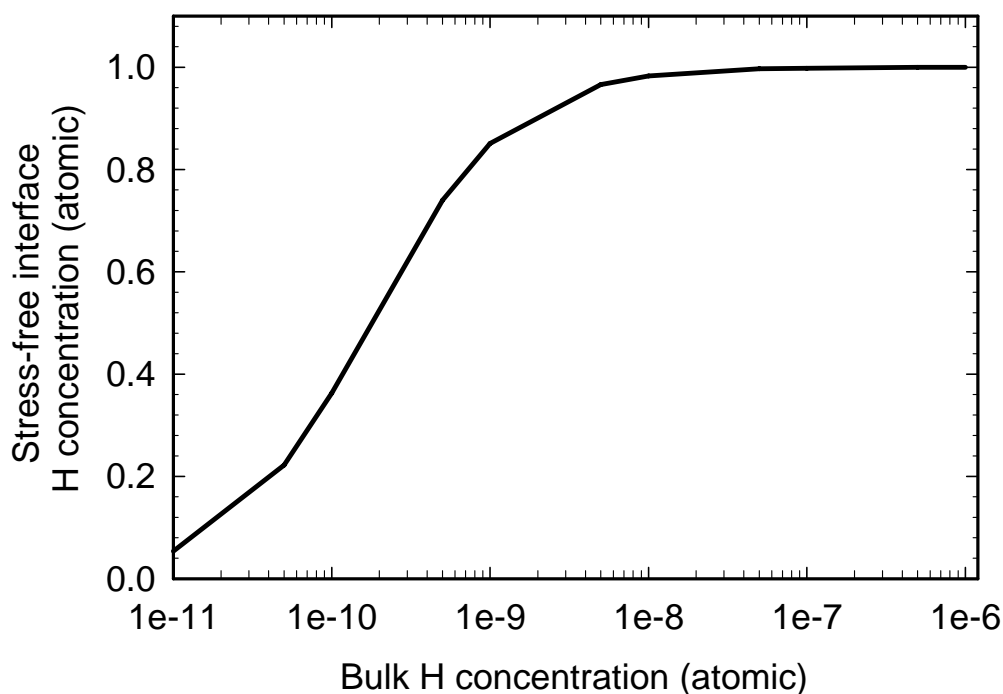
Figure 5.4.   The interface hydrogen concentration in the unstressed condition increases with increased bulk hydrogen concentration and saturates when hydrogen occupies all available trapping sites. The interface hydrogen concentration is much higher than the bulk hydrogen concentration.

5.5.4.2 Void nucleation model correlation and validation with hydrogen

Based on Equation (5.45), the bulk hydrogen concentration can be calculated based on applied hydrogen gas pressure. However, no hydrogen pressure data was available in the experiments by Kwon and Asaro[38], because hydrogen was charged electrochemically instead of by gas pressure. Normally, if the hydrogen bulk

concentration is known, the experimental data of void nucleation with hydrogen on smooth specimens can be used to find the material constant m. However, hydrogen bulk concentration can not be determined due to the reason described earlier [38]. Therefore, $m = 3.3$ was assumed based on the MD simulation results in chapter III, and was applied in the new void nucleation model to calculate the void volume density at different bulk hydrogen concentrations, as shown in Figure 5.5. Note; material constant m is most likely not the assumed value. However, the purpose of this study is to find out whether the new void nucleation model can match the trend of experimental data. Figure 5.5 also show a comparison of the model versus experimental data. Figure 5.5 shows that the calculated void volume density increased rapidly with increased plastic strain and bulk hydrogen concentration. When the bulk hydrogen concentration is 10^{-4}appm, the curve is very close to the experimental data until plastic strain reaches 0.62. The experimental data is higher than the model results at a plastic strain higher than 0.62. The reason may be due to neglecting the necking of the specimen in the later stage of the deformation. The necking of the specimen can induce high triaxiality, which can cause higher void nucleation rate.

In the experiments by Kwon and Asaro [38], an electrical current density of $2mA/cm^2$ same as the smooth specimens was also applied on the notch specimens, which indicate the bulk hydrogen concentration, is likely to be approximately the same in both type specimens. Based on Figure 5.5, the bulk hydrogen concentration was chosen as 10^{-4}appm for simulating the notch tensile tests. All the material constants in the notch specimen simulations were the same as the smooth specimen simulations. The notch tensile tests induced higher stress triaxialities and hydrostatic stresses, which can affect

the local hydrogen concentration and void nucleation, compared to the smooth specimens. Figure 5.6 shows void volume density versus plastic strain from experimental data and model results for the notch specimen, showing a fairly close comparison.

Figure 5.7 shows the plastic strain at the notch area in the hydrogen-free condition at the point of failure. The peak plastic strain is located at the outer surface of the notch. Figure 5.8 shows the stress triaxialities at the notch area in the hydrogen-free condition at the point of failure. The peak stress triaxiality is located in the center of the notch area. Figure 5.9 shows the void nucleation at the notch area in hydrogen-free condition at the point of failure. The peak void nucleation is located between the outer surface and the center of notch region. The study by Horstemeyer and coworkers [88] also show similar results, as shown in Figures 5.7, 5.8 and 5.9. Figure 5.10 shows the void volume density at the notched area in the hydrogen-charged condition at the point of failure. The peak void volume density is located in the center of the notch region. Figure 5.9 and 5.10 show that hydrogen caused the peak void volume density to move from the region close to the outer surface to the center of the notch region. This is because the high hydrostatic stress in the center causes an increase in local hydrogen concentration and hydrogen enhances the stress triaxiality-driven void nucleation.
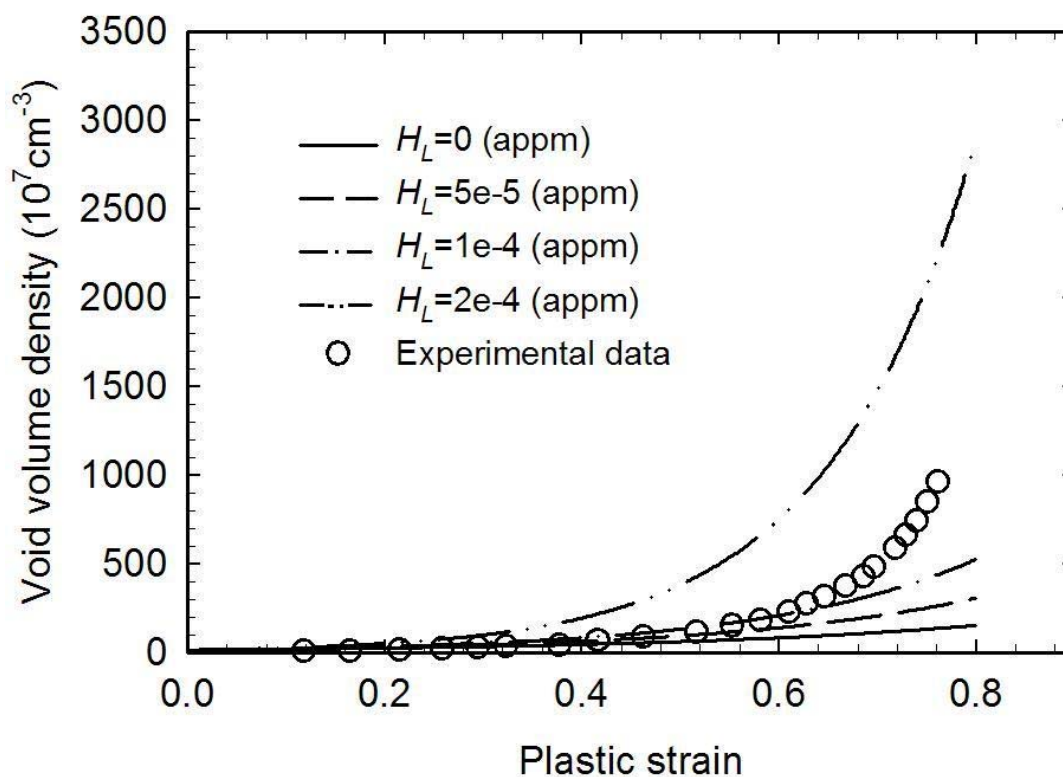
Figure 5.5.   The void volume density versus plastic strain of the smooth specimen at different bulk hydrogen concentrations from model results and from experimental data [38]. At the bulk hydrogen concentration H_L = 1e-4 (appm), the model results match well with the experimental results until at the high plastic strain.
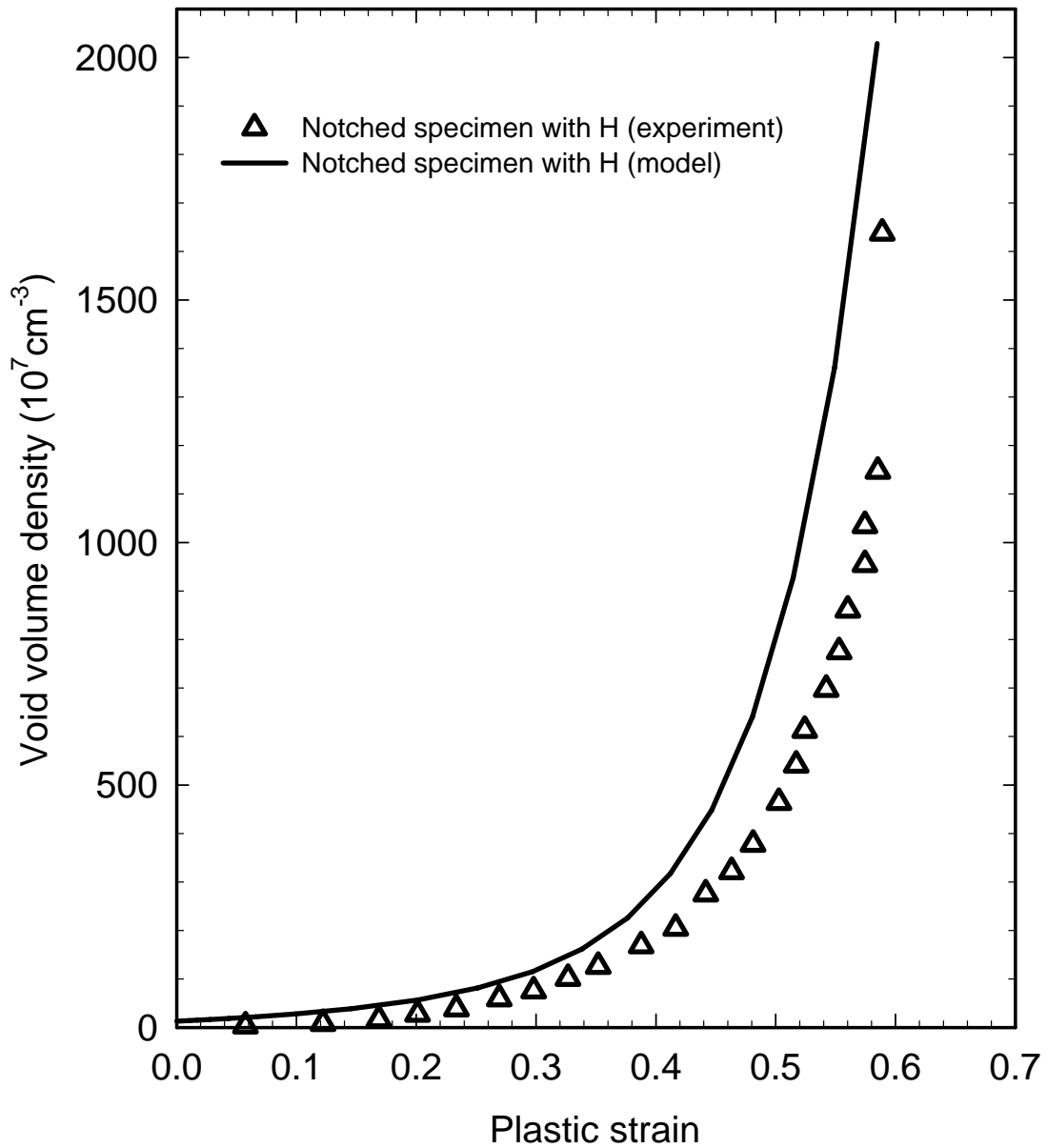
Figure 5.6.   The void number density versus plastic strain in the H-charged notch specimen from experimental data and from model results. The model results compared well with the experimental data [38].
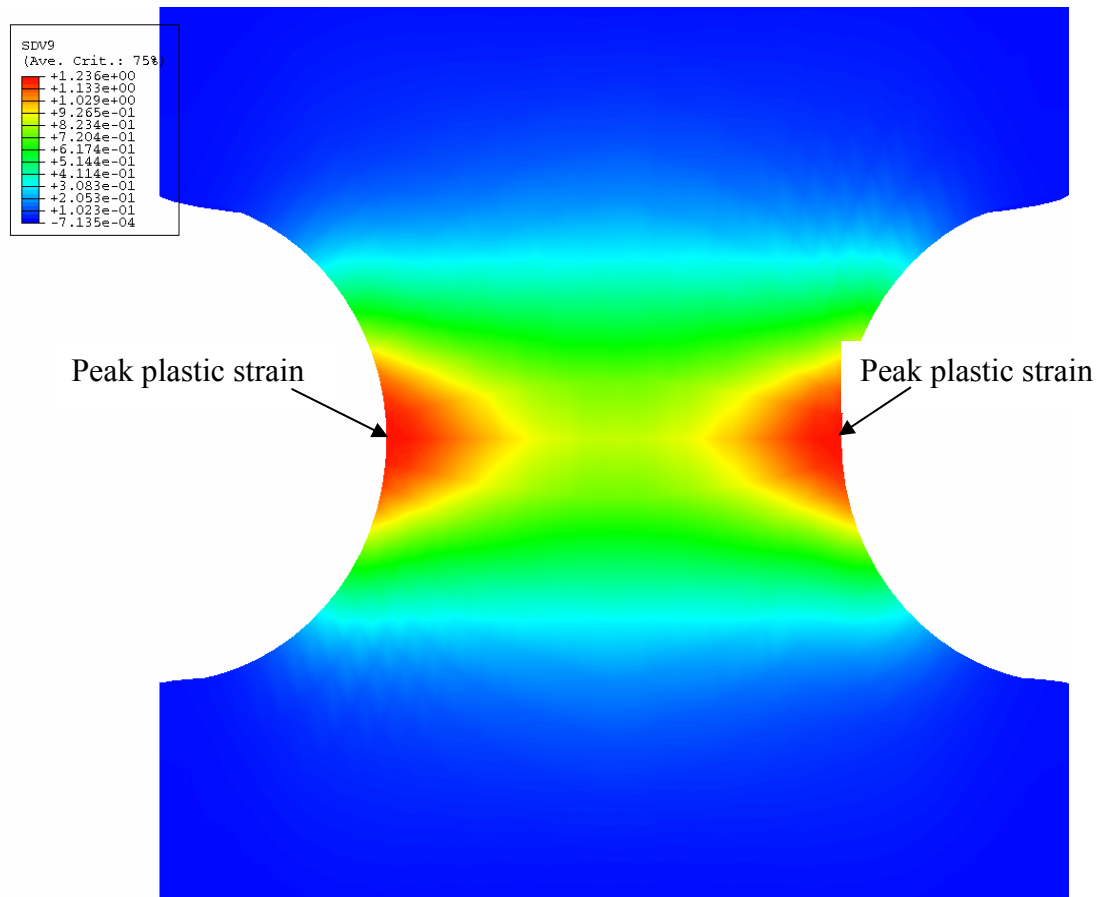
Figure 5.7.   The model simulation results show the plastic strain distribution in the hydrogen-free notch specimen at the point of failure. The peak plastic strain is located at the outer surface of the notch.
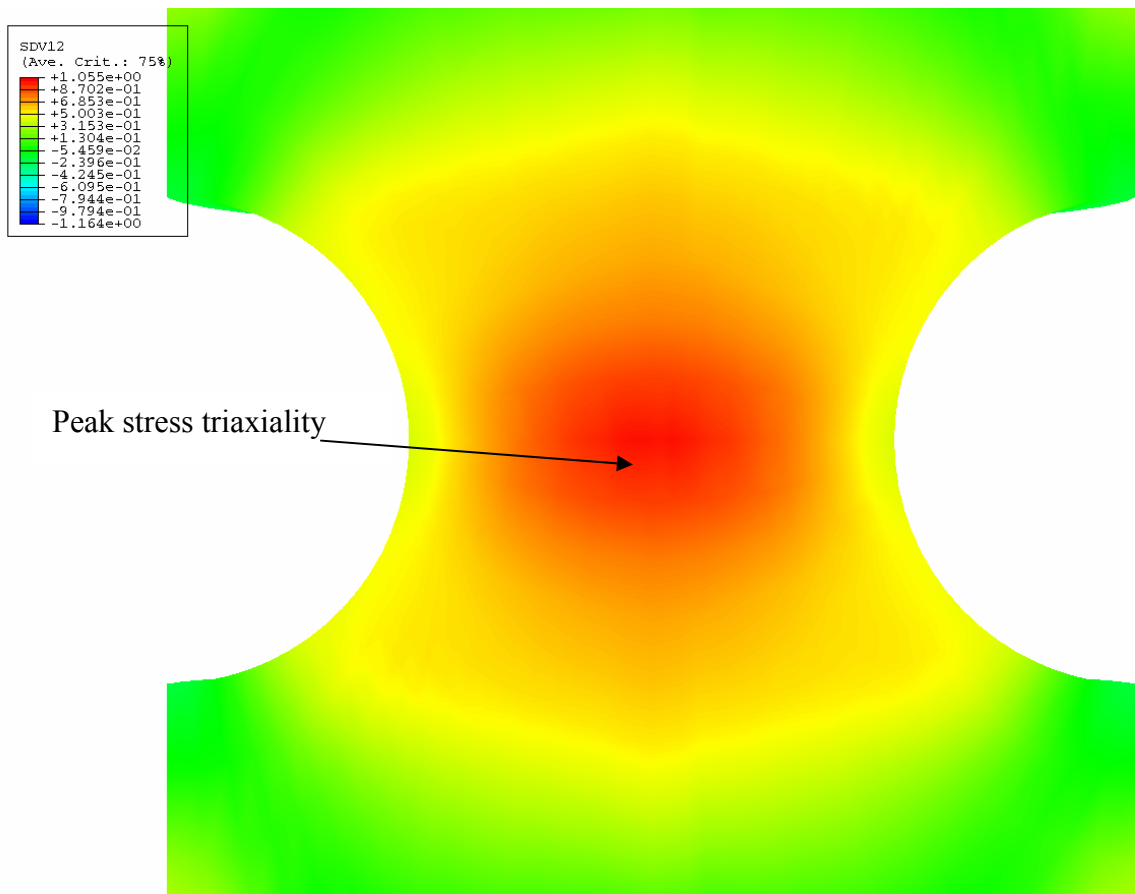
Figure 5.8.   The model simulation results show the stress triaxiality distribution in the hydrogen-free notch specimen at the point of failure. The peak stress triaxiality is located at the center of the notch.
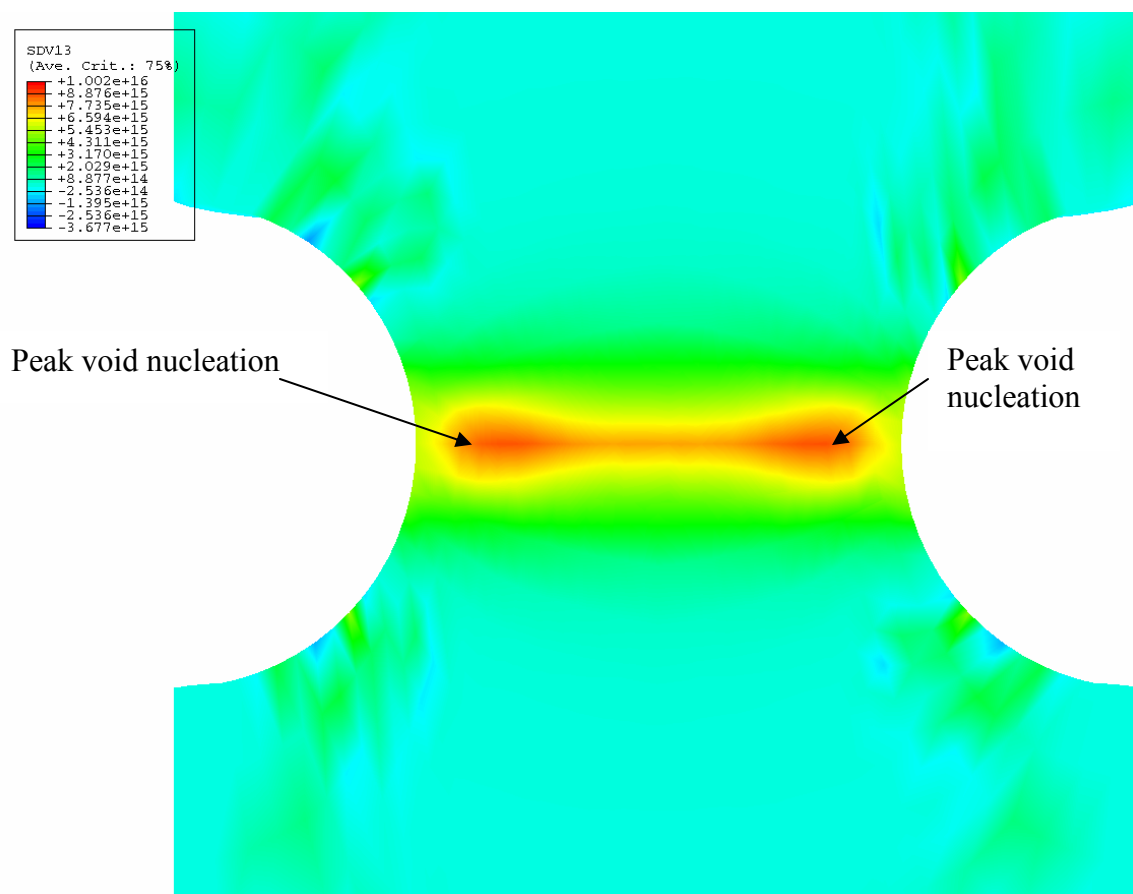
Figure 5.9. The model simulation results show the void nucleation distribution in the hydrogen-free notch specimen at the point of failure. The peak void nucleation is located at the area between the outer surface and the center in the hydrogen-free specimen.
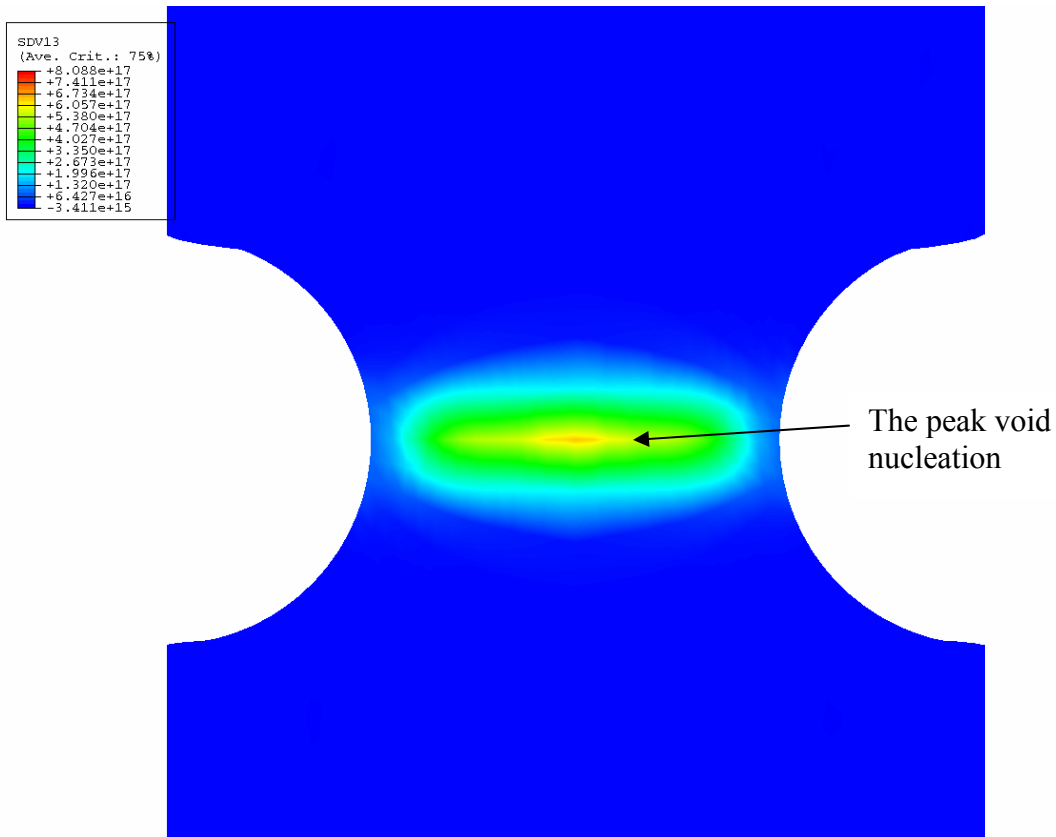
Figure 5.10.   The model simulation results show the void nucleation in the hydrogen-charged notch specimen at the point of failure. The peak void nucleation is located at the center of the specimen.

5.6   Summary of Chapter 5

The main points of this study can be summarized as follows:

▪ Hydrogen effects were added into the internal state variable damage framework.   The kinematic, thermodynamic and kinetics of a continuum damage model with hydrogen effects were described.

▪ A new void nucleation model with hydrogen effects was developed based on nanoscale results from previous chapters and experimental observations.

- The damage model with the new void nucleation equation was implemented into the user material code, which can be used with commercial finite element code ABAQUS.

- Finite element calculations were performed on smooth and notch tensile specimens. The results were compared favorably to the existing experimental data by Kwon and Asaro [38].

- The model results in the smooth specimen matched well with the experimental data until the plastic strain was higher than 0.6, then the experimental results were higher than the model results. A possible reason might be due to neglecting the necking of the specimen in the later stage of the deformation.

- The model results in the notch specimen followed the same trend as the experimental data. At the point of failure, in the hydrogen-free specimen, the location of the peak void nucleation was between the center and the outer face in the notched region; in the hydrogen-charged specimen, the location of the peak void nucleation was at the center of the notch region, because high hydrostatic stress in the center increased hydrogen absorption; also the effects of hydrogen on void nucleation were driven by the stress triaxiality.

- The calculated local hydrogen concentrations at the interfaces were much higher than the bulk hydrogen concentrations, because of the high trap binding energy at the interfaces. This indicates that even if hydrogen solubility is very small in many alloys, hydrogen can still induces failure because it is the local hydrogen concentration that drives hydrogen-related failures.

CHAPTER VI

SUMMARY AND FUTURE WORK

6.1   Summary

A continuum void nucleation model with hydrogen effects was developed by using information gathered from nanoscale studies and experimental observations. The new model was based on the Horstemeyer and Gokhale continuum void nucleation model. MD and MC simulations were performed to study hydrogen effects on plasticity, nanovoid nucleation, and interfacial debonding of different local grain boundaries. This study shows that hydrogen accumulates at the grain boundaries and causes the critical hydrostatic stress and strain for nanovoid nucleation to decrease with increased grain boundary hydrogen concentration at the grain boundaries. This study also shows that hydrogen-enhanced void nucleation depends on local grain geometries, possibly due to the local hydrogen distribution at the grain boundary. By inserting the MD simulation results into the Horstemeyer and Gokhale model, the relationship between nanovoid nucleation, grain boundary hydrogen concentration and local grain boundary geometries was determined quantitatively. MD and MC simulations were also performed to study hydrogen effects on plasticity and nanovoid nucleation in single crystal in hydrogen-precharged and dynamically-charged conditions. Hydrogen transport by stress gradient and dislocations were addressed in a dynamically-charged case. This study shows that

126

hydrogen causes a reduction on critical hydrostatic stresses for void nucleation in the dynamically-charged case due to hydrogen-induced volumetric expansion and hydrogen-induced stacking fault energy. The MD simulation results in single crystals were also inserted into the Horstemeyer-Gokhale model to extract the relationship between nanovoid nucleation and hydrogen concentrations. The nanoscale study suggests hydrogen affects the hydrostatic component of stress for nanovoid nucleation, particularly for the void nucleation induced by interfacial debonding. Based on nanoscale studies and experimental observation, the Horstemeyer and Gokhale model was modified to account for hydrogen effects. The modified model was then cast into a continuum damage framework with hydrogen effects and implemented into a user material code. ABAQUS [56] finite element calculations were performed to validate the model with experimental data. The model results matched well with the experimental results in the plastic strain lower than 0.6 in the smooth specimens. The model results followed the same trend with the experimental results in the notched specimens.

6.2   Future work

6.2.1   *Hydrogen effects on void nucleation by particle fracture*

In this research, hydrogen effects on void nucleation by interfacial debonding were studied. However, voids can nucleate by particle fracture under torsion and compression loads [47, 55]. To gain an understanding of the underlying mechanisms of the void nucleation by particle fracture with hydrogen effects, MD and MC simulations can be performed to study the particle fracture by embedding a hard-phase particle into a

ductile matrix under compression and torsion loading in the hydrogen-free and hydrogen-charged conditions. A quantitative relationship between local hydrogen concentration and nanovoid nucleation due to particle fracture may be extracted, and this relationship may be used to improve the continuum void nucleation model with hydrogen effects.

6.2.2 *Hydrogen effects on void nucleation at grain triple point polycrystals*

Void nucleation at grain triple points has been observed experimentally [149]. Querin and coworkers [150] observed the void nucleation at a triple point of 6022 aluminum. MD and MC simulations might be performed to study the hydrogen effects on void nucleation at grain triple points. MC simulations can first be performed to introduce hydrogen into the triple point, and MD simulation can then be performed to study the void nucleation at triple points under different loading conditions, and different length scales.

6.2.3 *Uncertainty on hydrogen-enhanced void nucleation*

The MD and MC simulation results in this research show statistical scatters due to the uncertainty related to the hydrogen concentration, hydrogen trapping sites, and void nucleation sites. Uncertainty analysis might be performed on those parameters to add statistics associated distribution in the new void nucleation model.

6.2.4 *Hydrogen interactions with interfaces and defects*

The grain boundaries studied were free of defects. That is why these simulation results show much higher interfacial strength than experimental data. To better represent the more realistic grain boundaries and interfaces, it is important to study the interaction

between hydrogen and defects at the grain boundaries and interfaces. One possible study might be to add different amounts of vacancies at the grain boundary and interfaces. Another possible study can be to add impurity such as carbon atoms in a nickel grain boundary. Because intergranular failure is often a fast fracture, the MD-MC process used in Chapter IV can be used in this study to simulate hydrogen diffusion along the grain boundary.

6.2.5   *Hydrogen effects on void growth and void coalescence*

This research was focused on hydrogen-enhanced void nucleation. Hydrogen effects on void growth and coalescence, isotropic hardening and kinematic hardening variables also need to be studied. Those effects can then be included into the continuum damage framework to predict damage and failure. The model should be fully coupled and include hydrogen in a steady state and a diffusive state.

6.2.6   *A continuum damage model with environmental effects*

When a structure is subjected to mechanical loading in a corrosive environment involving production of hydrogen, two processes are present simultaneously. First, anodic reaction causes pits and intergranual cracks on the surface of the material. Second, cathodic reaction produces hydrogen, which can diffuse into the metal and degrade material properties. A continuum damage model with environmental effects should include not only the damage with hydrogen effects, but also include the damage caused by pitting and intergranular corrosion on the surface. Both experimentation and simulations should be used to study the pitting and intergranular corrosion in order to capture the important mechanisms.

REFERENCES

[1]   William H. Johnson, "On Some Remarkable Changes Produced in Iron and Steel by the Action of Hydrogen and Acids," *Proceedings of the Royal Society of London*, Vol. 23, 1874 - 1875, pp. 168-179.

[2]   T. Toh and W. M. Baldwin, Jr. In Stress Corrosion Cracking and Embrittlement, W. D. Robertson (Editor), J. Wiley & Sons, New York, 1956.

[3]   A. H. Windle and G. C. Smith, "The Effect of Hydrogen on the Plastic Deformation of Nickel Single Crystals," *Metal Science Journal*, 1968, Vol. 2. pp.187-191.

[4]   A. H. Windle and G. C. Smith, "The effect of hydrogen on the deformation and fracture of polycrystalline nickel," *Metal Science Journal*, 1970, Vol. 4. pp.136-144.

[5]   M. R. Louthan. Jr, G. R. Caskey. Jr, J. A. Donovan and D. E. Rawl. Jr., "Hydrogen Embrittlement of Metals," *Material Science and Engineering*, American Society for Metals, Vol . 10, No. 6, 1972, pp. 357-368.

[6]   R. J. Gest and A. R. Troiano, "Stress Corrosion and Hydrogen Embrittlement in an Aluminum Alloy," Corrosion, Vol. 30, Aug, 1974, pp. 274-279.

[7]   N. E.Paton and J. C. Williams, "Effect of Hydrogen on Titanium and Its alloys," Hydrogen in Metals, proceedings of an International Conference on the Effects of Hydrogen on Materials properties and selection and Structural Design, 23-27, September, 1973, pp.409-431.

[8]   M. R. Louthan. Jr, "Effect of H on Metals," *Process Industries Corrosion*, *National Assoc. of Corrosion Engineers*, Houston, TX, 1975, pp. 126-134.

[9]   D. G. Westlake, "Generalized Model for Hydrogen Embrittlement," *Trans. ASM* (62), 1969, pp.1000-1006.

[10]   C.D. Beachem, "New Model for Hydrogen-Assisted Cracking-Hydrogen Embrittlement," *Metall Trans*. Vol.3. No. 2. 1972, pp. 437-451.

[11]   S. P. Lynch, "Mechanism of Hydrogen-Assisted Cracking," *Metals Forum*, Vol. 2, No. 3. 1979, pp. 189-200.

130

[12]   H. K. Birnbaum and P. Sofronis, "Hydrogen-enhanced Localized Plasticity—a Mechanism for Hydrogen Related Fracture," *Materials Science and Engineering*, A176 (1994) 191-202.

[13]   A. R. Troiano, "The Role of Hydrogen and Other Interstitials in The Mechanical Behavior of Metals," *Trans. ASM* 52, 1960, pp.54-80.

[14]   S. Jani, M. Marek, R. F. Hochman, E. I. Meletis, "A Mechanistic Study of Transgranular Stress Corrosion Cracking of Type 304 stainless Steel," *Metallurgical Transactions A*. Vol. 22A, no 6, June 1991, pp. 1453-1461.

[15]   Daniel P. Abraham, Carl J. Altstetter, "Hydrogen-enhanced Localization of Plasticity in Austenitic Stainless Steel," *Metallurgical and Materials Transactions A*: *Physical Metallurgical and Materials*, Vol. 26A, no. 11, 1995, pp. 2859-2871.

[16]   I. M. Robertson and H. K. Birnbaum, "An HVEM Study of Hydrogen Effects on The Deformation and Fracture of Nickel," *Acta Metallurgica*, Volume 34, Issue 3, March 1986, pp.353-366.

[17]   P. Sofronis, "Transmission Electron Microscopy Observations and Micromechanical/Continuum Models for The Effect of Hydrogen on the Mechanical Behaviour of Metals," *Philosophical Magazine*, Vol. 82, No. 17/18, 2002, pp. 3405-3413.

[18]   Jian-Sheng Wang, "The Thermodynamics Aspects of Hydrogen Induced Embrittlement," *Engineering Fracture Mechanics* 68 (2001), pp. 647-669.

[19]   N. R. Moody, M. I. Baskes, S. L. Robinson, and M. W. Perra, "Temperature Effects on Hydrogen-induced Crack Growth Susceptibility of Iron-based Super alloys," *Engineering Fracture Mechanics* 68 (2001), pp. 731-750.

[20]   H. K. Birnbaum, "Hydrogen Effects on Deformation and Fracture: Science and Sociology*," MRS Bulletin*, July 2003, pp. 479-485.

[21]   P. J. Ferreira, I.M. Robertson, and H.K. Birnbaum, "Hydrogen Effects on the Character of Dislocations in High-purity Aluminum," *Acta mater*. Vol. 47, No. 10, 1999, pp. 2991-2998.

[22]   P. J. Ferreira, I. M. Robertson and H. K. Birnbaum, "Influence of hydrogen on the Stacking Fault Energy of An Austenitic Stainless Steel," *Materials Science Forum* (Switzerland). Vol. 207-209, no.1, pp. 93-96, 1996.

[23]   W. M. Garrison Jr. and N.R. Moody, Ductile Fracture, *Journal of Physics and Chemistry of Solids*, Vol. 48, No. 11, 1987, pp.1035-1074.

[24] H. Matsui, H. Kimura, "The Effect of Hydrogen on the Mechanical Properties of High Purity Iron I. Softening and Hardening of High Purity Iron by Hydrogen Charging during Tensile Deformation," *Material Science and Engineering*, 40, 1979, pp. 207-216.

[25] Yu. Jagodzinki, H. Hanninen, O. Tarasenko and S. Smuk, "Interaction of Hydrogen with Dislocation Pile-ups and Hydrogen Induced Softening of Pure Iron," *Scripta Mater*, 43(2000), pp. 245-251.

[26] K. Oguri and H. Kimura, "The effect of Hydrogen on the Flow Stress of Iron with Various Purities," *Scripta Metallurgica*, Vol. 14, 1980, pp. 1017-1022.

[27] E. Lunarska and J. Flis, "Effect of Hydrogen charging-discharging on the Stress-Strain Relationship for Nickel," *Scripta Metallurgica*, 1984, Vol. 18, pp. 889-892.

[28] R. Garber, I. M. Bernstein and A. W. Thompson, "Effect of Hydrogen on Ductile Fracture of Spheroidized Steel," *Script Metallurgica*, Vol. 10. 1976, pp. 341-345.

[29] H. Cialone and R. J. Asaro, "Hydrogen-Assisted Fracture of Spheroidized Plain Carbon Steels," *Metall. Trans. A*. Vol. 12A, no. 8. 1981, pp. 1373-1387.

[30] I. G. Park and A. W. Thompson, "Hydrogen-Assisted Ductile Fracture in Spheroidized 1520 Steel. I. Axisymmetric Tension," *Metall. Trans. A*. Vol. 21A, no. 2, Feb. 1990, pp. 465-477.

[31] H. J. Maier, W. Popp and H. Kaesche, " Effects of Hydrogen on Ductile Fracture of a Spheroidized Low Alloy Steel," *Material Science and Engineering A* 191 (1995), pp. 17-26.

[32] Y. Liang, "Micromechanics of the Hydrogen Effect on Plasticity and Interfacial Decohesion," *PhD dissertation*, University of Illinois, 2003.

[33] Y. Liang, P. Sofronis and R. H. Dodds, Jr., "Interaction of hydrogen with crack-tip plasticity: effects of constraint on void growth," *Material Science and Engineering A*, Vol 366, Issue 2, 2004, pp.397-411.

[34] R.A. Oriani and P.H. Josephic, "Hydrogen-Enhanced Load Relaxation in a Deformed Medium-Carbon Steel," *Acta Metallurgica*, Vol. 27, Issue 6, 1979, pp. 997-1005.

[35] A. W. Thompson, "Hydrogen-Assisted Fracture in Single-Phase Nickel Alloys," *Scr. Metall*. Vol. 16, no. 10, Oct. 1982, pp. 1189-1192.

[36]   T. D. Lee, T. Goldenberg, J. P. Hirth, "Effect of hydrogen on fracture of U-notched bend specimens of spheroidized AISI 1095 steel," *Metallurgical Transactions A-Physical Metallurgy and Materials Science.* Vol. 10A, Feb. 1979, pp. 199-208.

[37]   In-Gyu Park, Anthony W. Thompson, "Hydrogen-Assisted Ductile Fracture in Spheroidized 1520 Steel: Part I, Axisymmetric Tension," *Metallurgical Transaction A*, v21A, n2, Feb, 1990, pp. 465-477.

[38]   Dong-IL Kwon and R. J. Asaro, "Hydrogen-Assisted Ductile fracture in Spheroidized 1518 Steel," *Acta Metallurgical Materialia,* Vol, 38, n. 8. pp.1595-1606, 1990.

[39]   C.P. You, A.W. Thompson, and I.M. Bernstein, "Ductile Fracture Processes in 7075 Aluminum," *Metallurgical Transactions A*, Vol. 26A, February 1995, pp. 407-415.

[40]   Xing-Gang Jiang, Wu-Yang Chu and Ji-Mei Xiao, "Hydrogen induced Void nucleation of 310 Stainless Steel," *Acta Metall, Mater*, Vol 43, No. 10, 1995, pp. 3727-3732.

[41]   M. Ashby, "Working Hardening of Dispersion-hardened Crystals," *Phil. Mag*, 14, 1966, pp. 1157-1178.

[42]   A. R. Rosenfield, "Criteria for Ductile Fracture of Two-Phase Alloys," *Metall. Rev*, 13, 1968, pp. 29-40.

[43]   T. W. Barbee, L. Seaman, R. Crewdson, D. Curran, "Dynamic Fracture Criteria for Ductile and Brittle Metals," *J. Materials*. JMLSA 7 (3), 1972, pp. 393-401.

[44]   A. L. Gurson, "Continuum Theory of Ductile Rupture by Void nucleation and Growth-1. Yield Criteria and Flow Rules for Porous Ductile Media," *J. Engineering. Materials Techn*, 99, 1977a, pp. 2-15.

[45]   A. Needleman and J. R. Rice, "Limits to Ductility Set by Plastic flow Localization," In: Koistinen, D. P., Wang, N. M. (Eds). *Mechanics of Sheet Metal Forming*, Plenum Publishing Co, 1978, 237-265.

[46]   J. P. Hirth and W. D. Nix, "Analysis of Cavity Nucleation in Solids Subjected to External and Internal Stresses," *Acta Metall. Mater*, 33, 1985, pp. 359.

[47]   M. F. Horstemeyer, A.M. Gokhale, "A Void-crack Nucleation Model for Ductile Metals," *International Journal of Solids and Structures* 36 (1999) 5029-5055.

[48]   Y. Liang, P. Sofronis, "Toward a Phenomenological Description of Hydrogen-induced Decohesion at Particle/Matrix Interfaces," *Journal of the Mechanics and Physics of Solids* 51 (2003) 1509-1531.

[49]   S. M. Myers, M. I. Baskes, H. K. Birnbaum, J. W. Corbett, G. G. Deleo, S. K. Estreicher, E. E. Haller, P. Jena, N. M. Johnson, R. Kirchheim, S. J. Pearton, M. J. Stavola, "Hydrogen Interaction with Defects in Crystalline Solids," *Reviews of Modern Physics*, Vol. 64, No.2, April, 1992.pp.560-609.

[50]   H. K. Birnbaum and P. Sofronis, "Hydrogen-Dislocation Interactions," *Hydrogen Effects in Materials, Proceedings of Fifth International Conference on the Effects of Hydrogen on Material Behavior*, 1994, pp.15-34.

[51]   M. Daw and M. I. Baskes, "Embedded-atom method: Derivation and application to impurities, surfaces, and other defects in metals," *Physical Review* B, 29(12): 6443-6453, 1984.

[52]   S. M. Foils, "Calculation of the Surface Segregation of Ni-Cu Alloys with the Use of the Embedded-Atom Method," *Physical Review B*, Volume 32, Number 12, 1985, 7685-7693.

[53]   D. J. Bammann, M. L. Chiesa and G. C. Johnson, " A State Variable Damage Model for Temperature and Strain Rate Dependent Metals" *Constitutive laws*: *Theory*, *experiments*, *and numerical implementation*, eds. A. M. Rajendran and R. C. Batra, CIMNE, Barcelona, pp. 84-97, 1995.

[54]   D. J. Bammann, M. L. Chiesa and G. C. Johnson, " Modeling Large Deformation and Failure in Manufacturing Processes," *Theoretical and Applied mechanics*, eds. T. Tatsumi, E. Wannabe, and T. Kambe, pp. 359-376, 1996.

[55]   M. D. Dighe, A. M. Gokhale and M. F. Horstemeyer, "Effect of Loading condition and Stress State on Damage evolution of Silicon Particles in an Al-Si-Mg-Base Cast Alloy," *Metallurgical and Materials Transactions* A, Vol 33, No 3, Mar 2002, pp.555-565.

[56]   ABAQUS, version 6.3, 2002

[57]   D. McLean, Grain Boundaries in Metal, Oxford press, 1957.

[58]   Gang Lu and Efthimios Kaxiras, "an Overview of Multiscale Simulations of Materials," *Condensed matter*, 2004.

[59]   G. Lu, V. V. Bulatov, N. Kioussis, "Dislocation Constriction and Cross-Slip: An *ab initio* Study," Phys. Rev. B, 66, 144103, 2002.

[60]   Nasr M. Ghoniem, Esteban P. Busso, Nicholas Kioussis and Hanchen Huang, "Multiscale Modeling of Nan mechanics and Micromechanics: An Overview," *Philosophical Magazine*, Vol., 83, Nos. 31-34, 3475-3528.

[61]   R. O. Jones, "The Density Functional Formalism, Its Applications and Prospects, reviews of Modern Physics," Vol. 61, No. 3, 1989.

[62]   M. S. Daw, S. M. Foils and M. I. Baskes, "The Embedded-Atom Method (EAM): a Review of Theory and Applications," *Material Science Report* (The Netherlands), Vol. 9, no. 7-8, pp. 251-310. March, 1993.

[63]   Farid F. Abraham, Robert Walkup, Huajian Gao, Mark Duchaineau, Tomas Diaz de La Rubia, and Mark Seager, "Simulating Materials Failure by Using Up to One Billion Atoms and The World's Fastest Computer: Working-Hardening," *Applied Physical Science*, Vol.99, no. 9, April , 2002, pp. 5783-5787.

[64]   R. J. Amodeo and N. M. Ghoniem, "Dislocation Dynamics. I. A Proposed Methodology for Deformation Micromechanics," *Phys. Rev.* B 41, 6958 - 6967 (1990).

[65]   Michael Zaiser**, "** Statistical Modeling of Dislocation Systems," *Material Science and Engineering* A, Vol 309-301, 2001, pp. 304-315.

[66]   W. K. Liu, E. G. Karpov, S. Zhang and H. S. Park, "An Introduction to Computational Nanomechanics and Material," *Computer methods in Applied Mechanics and Engineering*, 193, 2004, pp. 1529-1578.

[67]   P. M. Gullett, G. Wagner and A. Slepoy, "Numerical Tools for Atomistic Simulations," SANDIA REPORT, SAND2003-8782, 2004.

[68]   A. Rahman, "Correlations in the Motion of Atoms in Liquid Argon," Phys. Rev. Vol 136, no 2A, pp. 405-411, 1964.

[69]   J. E. Lennard-Jones, "Cohesion," *Proceedings of the Physical Society*, 1931, 43, 461-482.

[70]   M. I. Baskes, "The modified Embedded Atom Method," Vol. 42/PVP. Vol.294. *Computational Material Modeling*, ASME, 1994. pp.23-35.

[71]   J. R. Beeler Jr, the Techniques of High-Speed Computer Experiments, Physics of Many-Particle Systems: Methods and Problems, New York, 1966.

[72] B. J. Berne, "Molecular Dynamics of the Rough Sphere Fluid. II. Kinetic Models of Partially Sticky Spheres, Structured Spheres, and Rough Screwballs," *J. Chem. Phys*. 66, 1977, 2821.

[73] D. C. Rapaport, *The Art of Molecular Dynamics Simulations*, Cambridge University Press, 2004.

[74] Hans C. Anderson, "Molecular Dynamic Simulations at Constant Pressure and /or Temperature," *J. Chem. Phys*. 72(4), 1980, pp 2384-2393.

[75] James E Angelo, N. R. Moody and M. I. Baskes, "Trapping of Hydrogen to Lattice Defects in Nickel," *Modeling Simul Mater. Sci. Eng*. 3(1995) 289-307.

[76] M. I. Baskes, Xianwei Sha ,J. E. Angelo and N. R. Moody, "Trapping of Hydrogen to Lattice Defects in Nickel," *Modeling Simul Mater. Sci. Eng*. 5(1997) 651-652.

[77] G. Simmons and H. Wang, "Single Crystal Elastic Constants and Calculated Aggregate Properties: a Handbook," MIT Press, 1971.

[78] W. Wyciskw and M. Feller-Kniepmeier, "Quenching Experiments in High Purity Ni," *Journal of Nuclear Material*, 69/70, 1978, pp. 616-619.

[79] George E. Dieter, "Mechanical Metallurgy," *Material Science & Metallurgy,* McGraw-Hill, New York, 1988.

[80] D. C. Stouffer and L. T. Dame, Inelastic Deformation of Metals: models, mechanical properties, and Metallurgy, Wiley-IEEE, 1996.

[81] N. Metropolis, A. W. Metropolis, M. N. Rosenbluth, A. H. teller and E. Teller, "Equation of State Calculations by Fast Computing Machines," *J. Chem. Phys*. 21, 1087 (1953).

[82] Faken Daniel, Jonsson Hannes, "Systematic Analysis of Local Atomic Structure Combined with 3D Computer Graphics," *Computational Material Science* 2 (1994) 279-286.

[83] Andrew S. Clarke and Hannes Jonsson, "Structural Changes Accompanying Densification of Random Hard-Sphere Packings," *Physical Review* E, Vol 47, No. 6. 1993, pp. 3975-3984.

[84] L.M. Kachanov, "Time of the Rupture Process under Creep Condition," Izv. Akad. Nauk. SSR, Otd. Tekh. Nauk, 1958.

[85]   Y. N. Rabotnov, "Creep Problem in Structural Members," North-Holland, Amsterdam, 1969.

[86]   Dierk Raabe, Franz Roters, Frédéric and Long-Qiang Chen, Continuum Scale Simulation of Engineering materials, Fundamentals-Microstructures-Process Application, Wiley-Vch, Berlin, 2004.

[87]   Jean lemaitre, A Continuous damage Mechanics Model for Ductile Fracture, Journal of engineering Materials ad Technology, Vol. 107, January, 1985, pp. 83-90.

[88]   M.F. Horstemeyer, J. Latrop, A.M. Gokhale, M. Dighe, "Modeling Stress State Dependent Damage Evolution in a Cast Al-Si-Mg Aluminum Alloy," Theoretical and Applied Fracture Mechanics 33 (2000) 31-47.

[89]   M. F. Horstemeyer and M. I. Baskes, "Atomistic Finite Deformation Simulations: A Discussion on length Scale Effects in Relation to Mechanical Stresses," *J. Eng.Matls. Techno.* Trans. ASME, Vol. 121, pp. 114-119, 1999.

[90]   M. F. Horstemeyer, M. I. Baskes and S. J. Plimpton, "Computational Nanoscale Plasticity Simulations Using Embedded Atom Potentials," *Theoretical and Applied Fracture Mechanics*, Vol. 37, No. 1-3, pp. 49-98, 2001.

[91]   M. F. Horstemeyer, S. J. Plimpton and M. I. Baskes, "Length Scale and Time Scale Effects on the Plastic Flow of FCC Metals," *Acta Mater.*, Vol. 49, pp. 4363-4374, 2001.

[92]   W. W. Gerberich, N. I. Tymak, J. C. Grunlan, M. F. Horstemeyer and M. I. Baskes , " Interpretations of Indentation Size Effects," *J. Applied Mechanics,* Vol. 69, No. 4, pp. 443-452, 2002.

[93]   M. F. Horstemeyer, T. J. Lim, W. Y. Lu, D. A. Mosher, M. I. Baskes, V. C. Prantil and S. J. Plimpton, "Torsion/Simple Shear of Single Crystal Copper," *Journal of Engineering Materials and Technology,* Vol. 124, pp. 322-328, 2002.

[94]   M. F. Horstemeyer, M. I. Baskes, V. C. Prantil, J. Philliber and S.Vonderheide, "A Multiscale Analysis of Fixed-End Simple Shear Using Molecular Dynamics, Crystal Plasticity, and A Macroscopic Internal State Variable Theory," Modeling Simul. Mater. Sci. Eng. Vol. 11, pp. 265-286, 2003.

[95]   K. Solanki , M. F. Horstemeyer, M. I. Baskes, H. Fang, "Multiscale Study of Dynamic Void Collapse in Single Crystal," *Mechanics of Materials*, Vol. 37, pp. 317-330, 2005.

[96]   G. P. Potirniche and M. F. Horstemeyer, "On the Growth of Nanoscale Fatigue Cracks," *Phil. Mag. Letters*, Vol. 86, No. 3, pp. 185-193, 2006.

[97]   G. P. Potirniche, M. F. Horstemeyer, B. Jelinek, G. J. Wagner, "Fatigue Damage in Nickel and Copper Single Crystals at Nanoscale," *International Journal of Fatigue*, Vol.27, No. 10-12, pp. 1179-1185, 2005.

[98]   G. P. Potirniche, M. F. Horstemeyer, G. J. Wagner, P. M. Gullett, "A Molecular Dynamics Study of Void Growth and Coalescence in Single Crystal Nickel," *International Journal of Plasticity*, Vol. 22, No.2, pp. 257-278, Feb, 2006.

[99]   Richard P Gangloff, "Hydrogen Assisted Cracking of High Strength Alloys," *Compressiove Structural Integrity*, Vol 6, I. Milne, R. O. Ritchie and B. Karihaloo, Editors-in-Chief, Elsevier Science, New York, NY, 2003, pp.1-194

[100]   N. R. Moody, J. E. Angelo, S. M. Foiles, and M. I. Baskes, "Atomistic Simulation of The Hydrogen-Induced Fracture Process in an Iron-based Superalloy," *Symposium on New Techniques for Characterizing Corrosion and Stress Corrosion*, Cleveland, OH, 29 Oct 1995.

[101]   D. Tanguy, B. Bayle and T. Magnin, "Hydrogen Effects on GB Fracture during SCC in Al-Mg; Critical Experiments and Computer Simulations," *Hydrogen Effects on Material Behavior and Corrosion Interactions*, 2003, pp. 873-882.

[102]   A. Sato, K. Kon, S. Tsujikawa, Y. Hisamatsu, "Effect of Grain Boundary Orientation on the Hydrogen Embrittlement of Alloy 600 With Coarse Columnar Crystals," *Corrosion Engineering* (Japan), Vol. 41, no.1, pp. 51-64, 1992.

[103]   Y. Pan, B. L. Adam, T. Olson and N. Panayotou, "Grain-Boundary Structure Effects on Intergranular Stress Corrosion Cracking of Alloys X-750," *Acta Mater*, 44, 4685-4695, 1996.

[104]   Corrosion: Fundamentals, Testing, and Protection, Volume 13A, ASM Handbook, 2003.

[105]   D. Hull and D. J. Bacon, Introduction to Dislocations, Fourth edition, 2001.

[106]   James R. Welty, Charles E, Wicks, Robert E. Wilson, "Fundamentals of Momentum, Heat, and Mass Transfer," Third edition, John Wiley & Sons, 1984.

[107]   C. A. Wert and R. C. Frank, "Trapping of Interstitials in Metals," *Annual Review of Material Science,* Vol 13, 1983, 139-172.

[108] T. Boniszewski and G. C. Smith, "The Influence of Hydrogen on The Plastic Deformation, Ductility and Fracture of Nickel in Tension," *Acta Metallurgica*, Vol, 11, March, 1963, pp. 165-178.

[109] D. H. Lassila and H. K. Birnbaum, "Effect of Diffusive Hydrogen Segregation on Fracture of Polycrystalline Nickel," *Acta Metallurgical*. Vol. 34, pp. 1237-1243, July, 1986.

[110] D. H, Lassila and H. k. Birnbaum, "The effect of diffusive segregation on the fracture of hydrogen charged nickel," *Acta Metallurgical*, Vol. 36, pp. 2821-2825. Oct.1988.

[111] G. J. Baxter, T. Furu, Q. Zhu, J. A. Whiteman and C. M. Sellars, "The Influence of Transient Strain-Rate deformation Condition on The Deformed Microstructure of Aluminum Alloy Al-1%Mg," *Acta Mater*, Vol. 47. No.8. pp. 2367-2376, 1999.

[112] Ken Gall, M. F. Horstemeyer, Mark Van Schilfgarde and M. I. Baskes, Atomistic Simulations on the Tensile Debonding of an Aluminum-Silicon Interface, *Journal of the Mechanics and Physics of Solids*, 48(2000), 2183-2212.

[113] D. M. Symons, "a Comparison of Internal Hydrogen Embrittlement and Hydrogen Environment Embrittlement," Bettis Atomic Power Laboratory, 1999.

[114] B. A. Wilcox and G. C. Smith, "Intercrystalline Fracture in Hydrogen-charged Nickel," *Acta Metallurgica*, Vol. 13, March, 1965, pp. 331-343.

[115] R. H. Jones, S. M. Bruemmer, M. T. Thomas and D. R. Baer, "Grain Boundary Chemistry, Fracture Mode and Ductility Comparisons for Iron and Nickel Tested at Cathodic Potentials," *Hydrogen Effects in Metals*, 1980, pp. 369-377.

[116] A. Kimura and H. K. Birnbaum, Hydrogen Induced Grain boundary Fracture in High Purity Nickel and Its Alloys-Enhanced Hydrogen Diffusion Along Grain Boundary, *Acta Metall*, Vol. 36, No. 3. pp. 757-766, 1988.

[117] I. G. Palmer and G. C. Smith, "Proc. AIME Conf. Oxide Dispersion Strengthening," Bolton Landing, NY, Gordon and Breach, NY, 1967 .

[118] J. Gurland, "Observations on the Fracture of Cementite Particles in a Spheroidized 1.05 Percent C Steel, Deformed at Room Temperature ," *Acta Metall*., Vol. 20, No. 5, pp. 735-741, 1972.

[119] T. G. Nih and W. D. Nix, "A comparison of the dimple spacing on intergranular creep fracture surfaces with the slip band spacing for copper," *Scripta Metall*., Vol. 14, pp. 365-368, (1980).

[120] G. M. Bond, I. M. Robertson IM and H. K. Birnbaum, "The influence of Hydrogen on Deformation and Fracture Processes in High-Strength Aluminum Alloys," *Acta Metallurgica*, Volume 35, Issue 9, September 1987, pp.2289-2296.

[121] G. M. Bond, I. M. Robertson and H. K. Birnbaum, "Effects of Hydrogen on Deformation and Fracture Processes in High-Purity Aluminum," *Acta Metallurgica*, Volume 36, Issue 8, August 1988, P2193-2197.

[122] Q. Z. Chen, G. H. Zhou, Y. Z. Huang, W. Y. Chu, "Hydrogen-inducing nanovoids in thin crystals of 310 stainless steel," *Journal of Material Science*, Volume 33, Issue 9, October, 1998, pp4813-4819.

[123] Xuejun Xu, Mao Wen, Zhong Hu, Seiji Fukuyama, Kiyoshi Yokogawa, "Atomistic Process on Hydrogen Embrittlement of Single Crystal of Nickel by the Embedded Atom Method," *Computational Materials Science*, 23, 2002, pp.131-138.

[124] Wen Mao, Xu Xue-Jun, Omura Y, Fukuyama S, Yokogama K, "Modeling Hydrogen Embrittlement in Single Crystal Ni," *Computational Material Science* 30(2004) 202-211.

[125] J. P. Hirth and B. Carnahan, "Hydrogen Adsorption at Dislocations and Cracks in Fe," *Acta Metallurgica*, 26, 1795-1803, 1978.

[126] M. Parrinello and A. Rahman, "Polymorphic Transitions in Single Crystals: A New Molecular Dynamic Method," *J. Appl. Phys*. 52, 7182-7190 (1981).

[127] N. R. Moody, S. R. Robinson and M. W. Perra , "Internal hydrogen effects on thresholds for crack growth in the iron-based superalloy IN903," *Engineering Fracture Mechanics*, Vol. 39, No. 6, pp. 941. 1991.

[128] S. Sun, Kazuaki Shiozawa, J. Gu, N. Chen, "Investigation of deformation field and hydrogen partition around crack tip in fcc single crystal," *Metallurgical Transactions*, A, Vol: 26, Issue: 3, Mar 1995.

[129] C. Hsiao and W. Chu, "Some New Aspects of Hydrogen Damage," Hydrogen Effects in Metals; Moran; Wyo; 26-31 Aug. 1980.pp. 255-267.1981.

[130] H. Kimura and H. Matsui, "Softening and Hardening in High-Purity Iron and Its Alloys Charged With Hydrogen," *Hydrogen effects in metals*: proceedings of the third international conference on effect of hydrogen on behavior of materials sponsored by the physical metallurgy and mechanical metallurgy committees of the metallurgical society of AIME, 1980, pp191-208.

[131] K. S. Shin, C. G. Park, and M. Meshii, "Effects of Strain Rate, Purity and Thermal History on Mechanical Behavior of Cathodically Charged Iron," Hydrogen effects in metals: proceedings of the third international conference on effect of hydrogen on behavior of materials sponsored by the physical metallurgy and mechanical metallurgy committees of the metallurgical society of AIME, 1980, pp209-218.

[132] Marc André Meyers, Krishan Kumar Chawla, Mechanical Metallurgy, Principals and Applications, Prentice-Hall, Inc., Englewood Cliffs, New Jersey, 1984.

[133] D. Delafosse and T. Magnin, "Hydrogen Induced Plasticity in Stress Corrosion Cracking of Engineering Systems," *Engineering Fracture Mechanics* 68 (2001) 693-729.

[134] Lawrence E. Malvern, Introduction to the Mechanics of a Continuous Medium, Prentice-Hall Englewood Cliffs, NJ, 1969.

[135] P. Sofronis and R. M. McMeeking, "Numerical Analysis of Hydrogen Transport Near a Blunting Crack Tip," *J. Mech. Phys. Solids*. Vol. 37, no. 3, 1989, pp317-350.

[136] P. Sofronis, Y. Liang and N. Aravas, "Hydrogen Induced Shear Localization of the Plastic Flow in metals and Alloys," *Eur. J. Mech. A/Solids*, 20(2001), pp857-872.

[137] D. J. Bammann, P. Sofronis and P. Novak, "a Coupled Dislocation-Hydrogen Based Model of Rate Dependence Inelastic Deformation, Proceedings of International Conference on Fracture," pp.577, Turin, Italy, March 20-25, 2005.

[138] L. Davison, A. L. Stevens and M. E. Kipp, "Theory of Spall Damage Accumulation in Ductile Metals", *Journal of The Mechanics and Physics of Solids*, Volume 25, Issue 1, 1977, pp11-28.

[139] G. Alefeld and J. Völkl, Hydrogen in Metals, Springer-Verlad Berlin, 1978.

[140] B. D. Coleman and M. E. Gurtin, "Thermodynamics with Internal State Variables," *The Journal of Chemical Physics*, Volume 47, Number 2, 1967, pp598-613.

[141] D. J. Bammann, "A Model of Crystal Plasticity Containing a Natural Length Scale," *Material Science & Engineering A*, 2001, pp 406-410.

[142] J. Lemaitre and J. L. Chaboche, "Mechanics of Solid Materials," Cambridge University, 2000.

[143] H. Mecking and U. F. Kocks, "Kinetics of Flow and Strain-Hardening**,**" Acta Metall. Vol. 29, no. 11, pp1865-1875. Nov. 1981.

[144] F. A. McClintock, "A Criterion for Ductile Fracture by the Growth of Holes," ASME *J. Appl. Mech*. 35, 1985, pp363-371

[145] R. A. Oriani, Diffusion and Trapping of Hydrogen in Steel, *Acta Metallurgica*, Vol. 18, no. 1, pp147-157, 1970.

[146] A. Taha and P. Sofronis, Micromechanics Approach to the Study of Hydrogen Transport and Embrittlement, *Engineering Fracture Mechanics*, 68 (2001) 803-837.

[147] S. L. Pyun, J. T. Kim, Hydrogen Trapping at Spheroidized and Elongated Sulphidic Inclusions/ Matrix Interfaces in Mild Steel, *Steel Res*. Vol. 62, no. 11, pp512-517, Nov, 1991.

[148] B. Baranowski, T. B. Majchrzak and T. Flanagan, "The Volume Increase of FCC Metals and Alloys Due to Interstitials Hydrogen Over a Wide range of Hydrogen Contents," *J. Phys*, F: Met. Phys, 1971, pp258-261.

[149] A. J. Perry, "Cavitations in Creep," *Journal of Material Science*, Vol. 9, No. 6, 1973, 1016-1039.

[150] J. Querin, J, J. Schneider and M. F. Horstemeyer, "Use of EBSD to Quantify the Microstructural Damage in Aluminum Alloys under Monotonic Loading," *JOM*, Vol. 56, No. 1, pp168, 2005.